Thermodynamic Analysis and Modeling of Pd-Ni-S Novel Ternary Bulk Metallic Glass Forming System

Dissertation

zur Erlangung des Grades

des **Doktors der Ingenieurswissenschaften**

der

Naturwissenschaftlich-Technischen Fakultät

der

Universität des Saarlandes

vorgelegt von

Maryam Rahimi Chegeni

Saarbrücken

2025

Tag des Kolloquiums: 18.12.2025

Dekan: Prof. Dr.-Ing. Dirk Bähre

Berichterstatter: Prof. Dr. Ralf Busch

Prof. Dr. mont. Christian Motz

Vorsitz: Prof. Dr.-Ing. Frank Mücklich

Akad. Mitglied: Dr. Noora Aho

Abstract

This study explores both experimental and computational aspects of the thermo-physical properties of the novel ternary Pd-Ni-S Bulk Metallic Glass (BMG)-forming system. Unlike other complex ternary and quinary BMG-formers, the simplicity of this ternary system in terms of equilibrium thermodynamics allows for the application of the CALPHAD approach to model the underlying thermodynamics governing glass formation.

Experimental investigations include quantifying specific heat capacity and studying crystallization across various compositions in the glass forming range, critical for generating essential input data for CALPHAD calculations. Using a two-state model approach, initial modeling of the undercooled liquid and glass is conducted for individual elements and extended to the corresponding binary and ternary systems. Model predictions are validated against experimental findings and iteratively optimized.

Assessment of the Pd-Ni-S system's glass-forming ability involves calculating the crystallization driving force for all the forming phases by applying the parallel tangent method to the Gibbs free energy of crystalline and liquid phases at different compositions. This method provides a more accurate estimation of the nucleation driving force of the first forming phase compared to the conventional thermodynamic approach. These calculated driving forces are then used to model the isothermal Time-Temperature-Transformation (TTT) diagrams, and finally for the estimation of the interfacial energy between liquid and crystal during primary crystallization, which plays an important role in the glass-forming ability of this system.

Zusammenfassung

Diese Studie untersucht sowohl experimentelle als auch rechnerische Aspekte der thermophysikalischen Eigenschaften des neuartigen ternären Pd-Ni-S Bulk Metallglas (BMG)-Bildungssystems. Im Gegensatz zu anderen komplexen ternären und quinären BMG-Bildnern ermöglicht die Einfachheit dieses ternären Systems in Bezug auf das Gleichgewicht der Thermodynamik die Anwendung des CALPHAD-Ansatzes zur Modellierung der zugrunde liegenden Thermodynamik, die die Glasbildung steuert.

Experimentelle Untersuchungen umfassen die Quantifizierung der spezifischen Wärmekapazität und die Untersuchung der Kristallisation über verschiedene Zusammensetzungen im Glasbildungsbereich, was entscheidend ist, um wichtige Eingabedaten für CALPHAD-Berechnungen zu generieren. Unter Verwendung eines Zweizustandsmodells wird eine erste Modellierung der unterkühlten Flüssigkeit und des Glases für einzelne Elemente durchgeführt und auf die entsprechenden binären und ternären Systeme erweitert. Die Modellvorhersagen werden mit experimentellen Ergebnissen validiert und iterativ optimiert.

Die Bewertung der Glasbildungsfähigkeit des Pd-Ni-S-Systems umfasst die Berechnung der Kristallisationsantriebskraft für alle sich bildenden Phasen durch Anwendung der Methode des parallelen Tangenten an die Gibbs'sche freie Energie von kristallinen und flüssigen Phasen bei verschiedenen Zusammensetzungen. Diese Methode liefert eine genauere Schätzung der Keimbildungsantriebskraft der ersten sich bildenden Phase im Vergleich zum herkömmlichen thermodynamischen Ansatz. Diese berechneten Antriebskräfte werden dann verwendet, um die isothermen Zeit-Temperatur-Umwandlungsdiagramme (TTT) zu modellieren und schließlich zur Schätzung der Grenzflächenenergie zwischen Flüssigkeit und Kristall während der Primärkristallisation, die eine wichtige Rolle in der Glasbildungsfähigkeit dieses Systems spielt.

Acknowledgments

First and foremost, I would like to express my deepest gratitude to my supervisor, Prof. Dr. Ralf Busch, for his guidance and support throughout the past three years as I worked on my doctoral project at the Chair of Metallic Materials. He provided me with invaluable insights and constructive discussions that significantly advanced my research.

I would also like to extend my heartfelt thanks to Prof. Dr. Isabella Gallino, whose encouragement from the very beginning was a source of strength for me.

My sincere appreciation goes to my colleagues and fellow doctoral students: Lucas Ruschel, Bastian Adams, Sascha Riegler, Tom Jamison, Maximilian Frey, and Nico Neuber. Their collaboration, camaraderie, and support were instrumental in ensuring that our work at the Chair ran smoothly.

I am also grateful to the other members of the department, particularly Hermann Altmeyer and Jörg Eiden, for their invaluable technical support. My heartfelt thanks go to Dr. Frank Aubertin, whose constant availability and insightful advice helped me overcome numerous technical challenges. I would also like to express my appreciation to Martina Stemmler for her meticulous handling of our samples, and to Ms. Alfiya Kurt for her kind support and consistently helpful assistance — it has been truly appreciated.

Of course, I must also extend my deepest thanks to my friends and family for their unwavering support throughout my studies. My parents have always stood by me, and their encouragement means the world to me. My friends in Iran and Germany provided the necessary distractions that allowed me to return to my work with renewed energy and focus.

Last but not least, I wish to express my profound gratitude to my husband, friend, and colleague, Amirhossein Ghavimi. Over the past few years, he has been my anchor, especially while living 4,764 kilometers (Tehran to Saarbrücken) away from my parents. His presence, love, and unwavering support warmed my heart and made Germany feel like home. I eagerly anticipate all the adventures that life has in store for us together.

Maryam Rahimi Chegeni Saarbrücken 2025

Publications and Contributions

This research was funded by the Deutsche Forschungsgemeinschaft (DFG). The findings in this research resulted from the collaborative work between two research groups: one at Karlsruhe Institute of Technology, specializing in CALPHAD calculations, and the other at Saarland University, focusing on the experimental work.

The following papers from this research have been published:

- Maryam Rahimi Chegeni, Wenhao Ma, Sascha Sebastian Riegler, Amirhossein Ghavimi, Magnus Rohde, Fan Yang, Hans Jürgen Seifert, Isabella Gallino, Ralf Busch, ***“Thermodynamic analysis and modeling of Pd-Ni-S bulk metallic glass-forming system”***, Acta Materialia, Volume 294, 2025, 121074, ISSN 1359-6454, https://doi.org/10.1016/j.actamat.2025.121074.
- Wenhao Ma, Julian Gebauer, Andreas Klaus Czerny, Maryam Rahimi Chegeni, Isabella Gallino, Ralf Busch, Hans Jürgen Seifert, ***“Thermodynamic assessment of the sulfur and the nickel-sulfur systems”***, Calphad, Volume 89, 2025, 102821, ISSN 0364-5916, https://doi.org/10.1016/j.calphad.2025.102821.

A paper on the modeling of the ternary Pd-Ni-S system is currently being prepared.

The results from both the modeling and experimental work have been presented at several national and international conferences. Notable among these contributions are:

- **M. Rahimi-Chegeni**, W. Ma, S. Riegler, I. Gallino, M. Rohde, R. Busch, H. J. Seifert, "Thermodynamic analysis and modeling of novel ternary Ni-S-Pd based bulk metallic glass-forming systems", DPG 2024, Berlin, Germany.
- W. Ma, **M. Rahimi-Chegeni**, S. Riegler, I. Gallino, M. Rohde, R. Busch, H. J. Seifert, "Thermodynamic analysis and modeling of novel ternary Ni-S-based bulk metallic glass-forming systems", FEMS Euromat 2023, Frankfurt, Germany.
- **M. Rahimi-Chegeni**, W. Ma, S. Riegler, I. Gallino, M. Rohde, R. Busch, H. J. Seifert, " Thermodynamic Assessment and CALPHAD Calculations of the Ni-Pd-S Glass Forming Ternary System ", RQ 17 and ISMANAM 27 2023, Warsaw, Poland.
- W. Ma, **M. Rahimi-Chegeni**, S. Riegler, I. Gallino, M. Rohde, R. Busch, H. J. Seifert, "Thermodynamic analysis and modeling of novel ternary Ni-S-based bulk metallic glass-forming systems", Materials Science and Engineering (MSE) Congress, Darmstadt, Germany, 2022.

Within the scope of this PhD thesis, the authors secured funding for a proposal at the Deutsche Electron Synchrotron (DESY) high-energy synchrotron facility, titled ***"Structure and Crystallization Behavior of Different Ni-Pd-S Metallic Liquids by In-Situ X-ray Diffraction Under Aerodynamic Levitation".***

Moreover, building on the results of this work, the authors submitted a proposal to the Deutsche Forschung Gemeinschaft (DFG) to extend the CALPHAD model to the Pd-Ni-P glass forming system. Due to the success of the research on the Pd-Ni-S system, the new proposal just recently received two years of funding.

List of Abbreviations

BMG	Bulk Metallic Glass
CALPHAD	CALculation of PHAse Diagrams
SRO/ MRO	Short Range Order / Medium Range Order
SGTE	Scientific Group Thermodata Europe
DSC	Differential Scanning Calorimetry
DTA	Differential Thermal Analysis
Flash DSC	Fast Differential Scanning Calorimetry
TTT	Time-Temperature-Transformation
HEXRD	High-Energy X-Ray Diffraction
VFT	Vogel-Fulcher-Tammann
AG	Adam-Gibbs
JMAK	Johnson-Mehl-Avrami-Kumogorov
CCR	Critical Cooling Rate
MG	Metallic Glass
ECP	Efficient Cluster Packing
RSE	Representative Structural Elements
ES	Edge Sharing
VS	Vertex Sharing
FS	Face Sharing
ICME	(Integrated Computational Materials Engineering
MGI	Materials Genome Initiative
TLS	Two-Level Systems
CPT	Configuron Percolation Theory
FCC	Face-Centered Cubic
GFR	Glass Forming Region
WAXS	Wide-Angle X-ray Scattering
DESY	Deutsches Elektronen Synchrotron
ADL	Aerodynamic Levitation

PyFAI	Python Fast Azimuthal Integration
CRRs	Cooperatively Rearranging Regions

Table of Contents

1 Introduction 1

2 Bulk Metallic Glasses 4

2.1 Empirical Developments 4

2.2 Glass Transition Mechanism 6

2.3 Thermodynamics of Glass Forming Liquids 10

2.4 Kinetics of Glass Forming Liquids 13

2.5 Crystallization of Glass Forming Liquids 19

2.6 Structure of Glass Forming Liquids 26

3 CALPHAD Modeling 31

3.1 Introduction to CALPHAD 31

3.2 Thermodynamic Models 32

3.2.1 (Undercooled)Liquid and Amorphous State 32

3.2.2 Solid State 35

4 Pd-Ni-S Novel Ternary Glass Forming System 37

5 Experimental Methods 41

5.1 Sample Synthesis 41

5.2 Calorimetry Measurements 43

5.2.1 Differential Scanning Calorimetry (DSC) and Differential Thermal Analysis (DTA) 43

5.2.2 Fast Differential Scanning Calorimetry (FDSC) 46

5.3 High-energy Synchrotron X-ray Diffraction 55

5.4 CALPHAD Modeling 58

5.4.1 Modelling of pure Sulfur, Palladium, Nickel, Ni-S, Pd-S, and Ni-Pd binary systems 58

5.4.2 Modelling of the Pd-Ni-S ternary system 58

6 Results 60

6.1 Thermodynamic Studies 60

6.1.1 Experimental thermal and thermodynamic data 60

6.1.2 Isobaric specific heat capacity data 64

6.1.3 Excess Enthalpy, Entropy and Gibbs free energy 67

6.1.4 CALPHAD modeling 70

6.2 Kinetic Studies 73

6.2.1 Critical Cooling Rate Determination 73

6.3 Crystallization of the undercooled liquid 75

6.3.1 Aerodynamic Levitation Study 75

6.3.2 Time-Temperature-Transformation (TTT) Diagrams 79

7 Discussion 81

7.1 Gibbs free energy and driving force for crystallization 81

7.1.1 Experimental approach 81

7.1.2 CALPHAD approach 83

7.2 Fragility estimations 85

7.3 Interfacial energy calculation 88

8 Summary and Conclusion 92

9 References 94

Table of Figures

Figure 2-1. Advancements in the critical casting thickness of glass forming systems discovered between 1960 and 2000. Taken from [20]. 4

Figure 2-2. The schematic plot shows different solidification pathways as volume over temperature. Below the liquidus temperature (T), the liquid either crystallizes after some undercooling (ΔT, path 1) or transitions into a vitreous state (path 2). Another pathway (path 3) involves isothermal annealing, where the glassy state transforms into another glassy state through relaxation or physical aging. The fictive temperatures, marked as T_f^1 and T_f^2, correspond to the respective cooling rates and glassy states. Plotted based on [27]. 7

Figure 2-3. Changes in the Gibbs energy *G* and its derivatives with temperature for the first- and second-order phase transitions based on the Ehrenfest scheme. It's important to note that during a first-order transition, the Gibbs free energy (G) changes slope at the transition temperature, indicating a discontinuity in the first derivative. However, during a second-order (continuous) transition, the slope of G does not change at the transition temperature , meaning the first derivative remains continuous, though the second derivative exhibits a discontinuity. Taken from [29]. 8

Figure 2-4. Schematic description of the changes in viscosity η and relaxation time τ of the liquid in different stages as a function of temperature. As temperature decreases, both η and τ rapidly increase due to a decrease in atomic mobility. At the glass transition, with a viscosity around 10^{12} Pa.s and a relaxation time of about 10^2 s, vitrification occurs, causing the system to fall out of metastable equilibrium due to the crossover of the inherent and applied timescales. Plotted based on [27]. 9

Figure 2-5. Schematic description of the changes in a) Gibbs free energy of the liquid $G_l(T)$ and crystal $G_x(T)$ in different stages as a function of temperature. As temperature decreases, at a certain undercooling, the Gibbs free energy difference between liquid and crystal, ΔG^{l-x}, can be approximated by the difference between slopes of $G_l(T)$ and $G_x(T)$ at T_l, namely $\Delta S^m = S^l(T_l) - S^x(T_l)$, b) Molar heat capacity of the crystalline mixture, the glassy state, the SCL, and the equilibrium liquid as a function of temperature. The changes of c_p in the solid state can be described by Debye and Doulong-Petit's rule based on the temperature range. Plotted based on [40]. 12

Figure 2-6. Gibbs free-energy difference between the supercooled liquid and the crystalline state for eutectic and near eutectic alloys with different critical cooling rates. Taken from [38]. ..13

Figure 2-7. The so-called Angell plot, showing the changes in viscosity data for different alloys scaled by T_g^*. The inset shows the jump in c_p at T_g, which is in general large for fragile liquids and small for strong liquids. Taken from [46]. 15

Figure 2-8. Results of [1], (a) Fragility parameter (D^*) vs free activation energy per particle to cooperative rearrangements (C) derived from the fit of Adam–Gibbs equation to the viscosity data for the investigated BMG forming liquids, (b) changes in normalized configuration entropy plot of the investigated BMG forming liquids as a function of normalized temperature. 18

Figure 2-9. Gibbs free energy changes in a liquid imposed by the formation of a spherical crystalline nucleus with the radius r. The ΔG-curve contains a volume and a surface contribution. The critical radius r* represents the threshold below which nuclei are unstable. Clusters larger than r* are supercritical and will normally grow. Taken from [27]. 20

Figure 2-10. Changes of $I(T)$ and $u(T)$ as a function of temperature. At the liquidus temperature $\Delta G^{l-x} = 0$.Taken from [27]........22

Figure 2-11. The effect of the interfacial energy (γ^{l-x}), the Gibbs free energy difference between the liquid and the crystal (ΔG^{l-x}, indicated by the entropy of fusion, ΔS^m), and the kinetic fragility of the liquid on the changes in crystallization nose in a TTT diagram. GFA gradually improves from system 1 to system 3 by varying these factors. Taken from [27]. 24

Figure 2-12. Schematic illustration of the effect of wetting angel on the reduction of the energy barrier for stable nucleus formation, considering heterogeneous nucleation. A higher wetting angel results in a higher energy barrier. Taken from [69]. 25

Figure 2-13. Schematic TTT diagram of a glass forming liquid, illustrating the effects of homogenous and heterogenous nucleation on the CCR and crystallization nose. Taken from [27]. 25

Figure 2-14. ABED patterns of a distorted icosahedron with an FCC-like orientation, a-a′) Experimental ABED pattern and the corresponding characteristic diffraction angles in the experimental ABED pattern obtained from $Zr_{80}Pt_{20}$, b-b′) Simulated ABED pattern and the corresponding characteristic diffraction angles in the simulated ABED pattern. c) Illustration of the distorted icosahedron producing the ABED pattern shown in (b). d) Calculated [110] diffraction pattern of a FCC cluster. Taken from [77]. 27

Figure 2-15. Kasper polyhedra corresponding to different coordination numbers (Z), which are the dominant coordination polyhedra in relaxed metallic glasses.Taken from [80]. 28

Figure 2-16. 3D model of an assembly of clusters in a) $Ni_{80}P_{20}$, b) $Ni_{81}B_{19}$, and c) $Zr_{84}Pt_{16}$ metallic glass. The solute (P, B, Pt) centered clusters, shown by the dashed circles, exhibit icosahedral type ordering as their MRO. The Voronoi index for each cluster is given in triangular brackets to indicate its identity. The combination of edge sharing (ES), vertex-sharing (VS), and face sharing (FS) between the clusters defines the MRO. Taken from [80]. 29

Figure 2-17. a) Simulated pair distribution function g(r) of amorphous Ta in liquid (orange) and glassy (Blue) states. The inset shows a 2D illustration of the atomic arrangement, highlighting the shells surrounding a central atom. The second peak in g(r) represents the distance to the second nearest neighbor, where both the liquid, and the glassy structure show a split, which is correlated to the formation of different connections between the atomic clusters. b) Schematic illustration of different cluster connection schemes between neighboring clusters, consisting of 1-atom, 2-atom, 3-atom, and 4-atom connections. Taken from [83]. 30

Figure 4-1. Isothermal Ternary Phase Diagram of Pd-Ni-S system at a) 1173 K (900°C), b) 998 K (725°C), c) 823 K (550°C), and d) 673 K (400 °C). The 'hatched area' indicates the liquid state of the particular composition range at the respective temperatures. Taken from [16]...37

Figure 4-2. Binary Phase diagrams of a) Pd-S, b) Ni-S, and c) Pd-Ni. Taken from [112–114].....39

Figure 4-3. Glass forming region (GFR) in the ternary Pd-Ni-S system. Open circles indicate partially or fully crystalline samples, while filled circles denote fully amorphous samples with a thickness of at least 300 mm. The dashed blue lines represent the equilibrium phase fields at 673 K (400°C), as reported by Karup-Moller [16]. Taken from [40]. 40

Figure 5-1. Position of the investigated Pd-Ni-S compositions in the ternary phase diagram, located within the shaded glass-forming region (GFR), according to [15]..41

Figure 5-2. Synthesis procedure of nickel-sulfur (Ni-S) pre-alloy. On the left: Pure nickel and sulfur with their purities indicated. In the middle: Nickel and sulfur in a quartz tube undergoing induction melting. On the right: Ni-S binary alloy before and after grinding. Taken from [115]. 42

Figure 5-3. Schematic arrangement of the pre-alloys together with other elements (left) in the electric arc furnace, along with the final ingot (right) after melting, and the titanium getter for oxygen absorption (center). Taken from [115]. 42

Figure 5-4. Schematic a) step-wise temperature profile and b) heat flow curves from a DSC specific heat capacity measurement using the step method. The shaded grey areas depict the heating interval while the white sections indicate the isothermal holding time (Δt). Red heat flow signals are from the sample, black from the sapphire and gray from the empty pan measurement. Taken from [118]. 46

Figure 5-5. Flash DSC sensors, the left picture features a ceramic substrate with electrical connections and a membrane divided into two active zones (for sample and reference). The pictures in the middle and right show the membrane with a closer look at the active zones of the UFS 1 with a sample (middle) and the UFH 1 (right). Taken from [129]. 47

Figure 5-6. Flash DSC2+ produced by Mettler-Toledo. Taken from [129]..................................49

Figure 5-7. Critical cooling rate measurements temperature program. a) and b) Overheating the sample to the equilibrium liquid state and holding it, ensuring the homogenization of the liquid. c) Quenching the liquid with varying cooling rates. d) Short equilibration at temperatures far below the glass transition. e) Further heating scan to determine the crystalline percentage in the sample..51

Figure 5-8. Time-Temperature-Transformation (TTT) diagram measurements program upon cooling. a) and b) Overheating the sample to the equilibrium liquid state and holding it, ensuring the homogenization of the liquid. c) Rapid cooling of the sample with a constant cooling rate faster than the critical cooling rate. d) Isothermal holding at the target temperature for a sufficient time for full crystallization of the sample. e) Quenching of the sample and reheating to the equilibrium liquid temperature...52

Figure 5-9. Exothermal crystallization event in an isothermal measurement at 220°C, the times at which 1%, 50%, and 99% of the heat release occurred, are determined based on the enthalpy of crystallization and are used for the construction of the TTT diagram...............................53

Figure 5-10. a) Recorded heat flow signal of $Pd_{37}Ni_{37}S_{26}$ measured using step response method in cooling. The sample is cooled fast to bypass the crystallization and further temperature down jumps of 2 K followed by isothermal holding of 0.1024 s are applied. The glass transition happens almost from 190 °C to 160 °C. In the case of better glass forming systems like $Pt_{57.3}Cu_{14.6}Ni_{5.3}P_{22.8}$ more data before glass transition could be collected and a wider frequency range could be investigated [151], b) Reversing specific heat as a function of temperature and frequency obtained from step response analysis at 10 Hz by FDSC for $Pd_{37}Ni_{37}S_{26}$.............54

Figure 5-11. Aerodynamic levitation facility with its different components. 56

Figure 5-12. Close-up view of the levitation chamber. Water-cooled levitation stage at the bottom with a converging-diverging nozzle mounted on top of it. The nozzle is fixed by a screw-bracket. A test sample is mounted into the levitation nozzle..57

Figure 5-13. Schematic illustration of the in-situ synchrotron X-ray experiments set up. Taken from [167]. 57

Figure 6-1. Thermodynamic measurements, a-b) DSC (blue curve) and DTA (red curve) scans of Pd-Ni-S variations acquired during heating with 20 K/min, the glass transition temperature (T_g), crystallization temperatures (T_x), eutectic temperatures (T_{eu}) and liquidus temperatures (T_l) are indicated with black arrows...61

Figure 6-2. In-situ high energy synchrotron X-ray diffraction pattern of a) $Pd_{40}Ni_{40}S_{20}$, b) $Pd_{45.06}Ni_{33.88}S_{21.06}$ upon heating from the crystalline state at 20 K/min. In addition, the simulated diffraction patterns of the possible crystalline phases are shown. In both cases, the (Pd, Ni) solid solution is stable up to higher temperatures and melts away at about 1173 K and 923 K respectively. 63

Figure 6-3. Isobaric specific heat capacity data of glassy cp (orange circles), liquid (red circles), and crystalline state (blue circles) for Pd-Ni-S variations. The fits of crystalline states (blue full line) and liquid states (red full line) are based on the Inaba and Kubaschewski equations, Eq. (6-1), (6-2), and (6-3). 66

Figure 6-4. Changes in the enthalpy ΔH^{l-x}, scaled entropy $\Delta S^{l-x}$and Gibbs free energy ΔG^{l-x} with temperature for Pd-Ni-S alloy variations calculated using Eq. (2-2), (2-3) and (2-4). Circles shown in (c) for $Pd_{37}Ni_{37}S_{26}$ are ΔH_x values obtained during isothermal FDSC measurements.. 70

Figure 6-5. Calculated isothermal sections of the Pd-Ni-S ternary phase diagram at (a) 673 K, (b) 823 K, and (c) 998 K. Dashed blue lines indicate the experimental results obtained by Karup-Moller and Makovicky. 71

Figure 6-6. Comparison between the calculated heat capacity and the experimental results for some of Pd-Ni-S glass forming compositions. The empty triangles indicate the experimentally measured c_p data and the solid lines are the modeling result. 72

Figure 6-7. Changes in Crystallization enthalpy of a) $Pd_{31}Ni_{42}S_{27}$, b) $Pd_{33.5}Ni_{40.5}S_{26}$, and c) $Pd_{37}Ni_{37}S_{26}$ over a logarithmic cooling rate. Each enthalpy measurement was conducted under a constant heating rate of 100 K s^{-1} following an initial cooling from a temperature significantly above the liquidus temperature of the respective alloy. The point at which the plateau value in crystallization enthalpy is reached signifies the range where fully amorphous samples were achieved, indicating that the critical cooling rate was exceeded. 74

Figure 6-8. Scheil solidification simulation for Pd-Ni-S alloy variations in comparison with the in-situ WAXS measurement at 200 K/s cooling rate which is accompanied by a heat release due to recalescence, shown exemplarily for $Pd_{33.5}Ni_{40.5}S_{26}$. The simulated diffraction patterns of the crystalline equilibrium phases including (Pd, Ni) solid solution, Ni_3S_2, and Pd_4S are shown and used to detect the forming phases. 79

Figure 6-9. Isothermal time–temperature-transformation (TTT) diagram of a) $Pd_{31}Ni_{42}S_{27}$, b) $Pd_{33.5}Ni_{40.5}S_{26}$, and c) $Pd_{37}Ni_{37}S_{26}$ determined in fast differential scanning calorimetry (FDSC) (circles) and conventional DSC (squares) for $Pd_{31}Ni_{42}S_{27}$ from [40]. The dark blue and crimson curves show the Johnson–Mehl–Avrami fitting of the experimental data using experimentally determined crystalline mixture driving force and Calphad driving force, respectively. 80

Figure 7-1. Calculated Gibbs free energy function with respect to the crystalline state from Eq. (2-2), a) for the Pd-Ni-S alloy variations, b) in comparison to other glass-forming systems, taken from [2]. The slope of the driving force is proportional to $-\Delta S_m$. 82

Figure 7-2. Schematic Gibbs free energy curves for the competing phases for a nominal composition of X_q at $T < T_{eut}$ in a binary A-B system. ΔG^{l-x} is the Gibbs free energy difference between the liquid and the crystalline mixture $(\alpha + \beta)$. $\Delta \mu_A^{L-\alpha}$ is the actual driving force for the nucleation of an α-nucleus of the composition $\mathrm{X_n(T)}$ within the liquid with the composition $\mathrm{X_q}$ [3]. 82

Figure 7-3. Calculated driving forces for crystallization of all the crystalline phases that compete with the undercooled liquid for a) $Pd_{23.9}Ni_{46.9}S_{29.2}$, b) $Pd_{31}Ni_{42}S_{27}$, c) $Pd_{33.5}Ni_{40.5}S_{26}$, d) $Pd_{37}Ni_{37}S_{26}$, e) $Pd_{40}Ni_{40}S_{20}$, and f) $Pd_{45.06}Ni_{33.88}S_{21.06}$ in comparison with the calculated $\Delta \boldsymbol{Gl} - \boldsymbol{x}$ between the undercooled liquid and the crystalline mixture. 84

Figure 7-4. Relaxation data acquired by step response analysis, a) $\log_{10}(\tau_d)$ of the $Pd_{31}Ni_{42}S_{27}$, $Pd_{33.5}Ni_{40.5}S_{26}$, and $Pd_{37}Ni_{37}S_{26}$ liquid over 1/T measured at a base frequency of 10 Hz using the step response analysis method. b) Linear Arrhenius fits of τ_d (T) in an Angell-type diagram for all three compositions. The linear fits are done with regard to the maximum $\log_{10}(\tau_d)$ data point which is the same for all the three compositions to define $T*$ and the m-fragility ($m\tau$). 86

Figure 7-5. Changes in $1/\Delta \mathrm{C_p^{l-x}(T_g)}$ as a function of composition (Pd content) together with the approximated kinetic fragility parameter D^* plotted for all Pd-Ni-S alloy variations.7-6 88

Figure 7-6. Schematic changes of $H - T_m S$ and G across the solid/liquid interface at the equilibrium melting temperature, which shows the origin of the solid/liquid interfacial energy γ_{sl}. Taken from [60]. 91

Figure 7-7. Schematic illustration depicting the effect of interfacial energy on the solubility of small particles. Taken from [60]. 91

List of Tables

Table 6-1. Measured thermodynamic characteristic temperatures and enthalpies for Pd-Ni-S variations: glass transition temperature (T_g), crystallization onset temperature (T_x), eutectic temperature (T_{eu}) and liquidus temperature (T_l), enthalpy of crystallization ($\Delta \mathrm{H_x}$), enthalpy of fusion ($\Delta \mathrm{H_m}$), and entropy of fusion ($\Delta S_m = \Delta \mathrm{H_m}/T_l$). Measurements are conducted with a heating rate of 0.333K/s (20K/min)............62

Table 6-2. Fitting parameters derived from applying Eq. (1) and (2) and (3) to the specific heat capacity data............67

Table 7-1. JMAK parameters acquired by the fitting procedure............89

1 Introduction

Metallic glasses are disordered and thermodynamically unstable materials that are formed by the rapid cooling of highly viscous melts, which slows down the crystallization and preserves the amorphous structure. Since the discovery of the first Au-Si amorphous metal by Duwez et al. [4], researchers have made significant progress in developing bulk metallic glasses (BMGs) with high glass-forming ability (GFA). This has been achieved by increasing the number of alloying elements and optimizing the compositions.

As a result, various BMG-forming systems have been developed based on elements such as copper (Cu) [5], iron (Fe) [6], nickel (Ni) [7], palladium (Pd) [8], titanium (Ti) [9], and zirconium (Zr) [10]. However, experimentally identifying the optimal glass-forming compositions is time-consuming and challenging due to the vast number of possible combinations. Therefore, there is a growing need for computational methods that can accurately describe the thermodynamics of metallic glasses and identify the optimal alloy compositions with the highest glass-forming ability. The computational approaches would accelerate the discovery of new metallic glass systems and provide valuable insights into the underlying mechanisms governing the glass-forming ability of different alloy systems.

The CALPHAD (CALculation of PHAse Diagrams) method is a powerful computational technique that is widely used to predict the thermodynamic properties of different materials systems. This approach integrates experimental data and theoretical models to generate phase diagrams, which are crucial for understanding the phase transitions within the materials across different compositions and temperatures. Originating in the late 1960s and the early 1970s, the CALPHAD method has evolved into an essential tool in materials science, aiding in designing and developing of new materials with tailored properties [11].

The CALPHAD methodology is particularly useful in the field of BMGs, thanks to the continuous advancements in thermodynamic modeling and calculation techniques to describe the Gibbs free energy of both crystalline and non-crystalline phases [12]. However, attaining precise modeling for amorphous alloys using the CALPHAD method has proven somewhat challenging due to several factors, despite varying levels of success in different attempts [13–15]. This modeling is intrinsically difficult due to the disordered structure of metallic glasses and the need to describe the glass transition and the complex short-range order (SRO)/medium-range order (MRO) present in these materials.

The second-generation CALPHAD database, proposed by SGTE (Scientific Group Thermodata Europe), has been limited in its ability to accurately model the (undercooled) liquid down to the glass transition temperature. Its polynomial description restricts the extrapolation of the Gibbs free energy expression to the metastable region, where less thermodynamic data is available. In contrast, the third-generation CALPHAD database [16] and the two-state liquid model, which describes the liquid as a mixture of two distinct states and provides a more physically sound and realistic representation of the thermodynamic properties [17], offer a more reliable approach for property extrapolation. Nevertheless, a comprehensive and concrete model and methodology are still missing for the modeling of the bulk metallic glass-forming systems, which are characterized by complex interatomic behaviors such as pronounced SRO and MRO.

In this study, the third-generation CALPHAD approach is implemented and expanded for a more physically accurate and reliable modeling of the undercooled liquid with a focus on the newly developed ternary BMG forming alloy system, Pd-Ni-S [18]. This system was first extensively studied by Karup-Moller et al. [19] in 1993 in terms of its equilibrium thermodynamics. They produced numerous samples of different compositions in the ternary system. They annealed them at specific temperatures including 1173 K, 998 K, 823 K, and 673 K, for extended periods, and subsequently quenched them to analyze the available phases. The comprehensive first-hand data on the equilibrium thermodynamics of this system obtained from their work serves as crucial input data for CALPHAD modeling.

More recently, Kuball et al. studied the glass-forming ability of the Pd-Ni-S system [18]. Based on his findings, the BMG forming region is confined to palladium contents ranging from 30 to 36.5 at. %, while the area where a BMG with a diameter of 1.6 mm can be produced is restricted to 24 – 27 at. % S. In his work, Kuball introduced $Pd_{31}Ni_{42}S_{27}$ composition as an effective glass former, featuring a critical casting thickness of 1.5 mm. He also highlighted the $Pd_{37}Ni_{37}S_{26}$ composition, which despite having less thermal stability, is likely closest to the eutectic point because of its short melting interval. His findings show that the glass-forming region is bordered by equilibrium phases of Ni_3S_2, (Pd, Ni) solid solution, and Pd_4S in its stable crystalline state, proving the simplicity of the system's equilibrium thermodynamics. This uncomplicated behavior makes this system an ideal candidate for thermodynamic modeling using the CALPHAD approach.

The experimental investigations contain both binary and ternary compositions within this ternary system. The ternary compositions are selected from the glass-forming region identified by Kubal et. al to enhance the input data for CALPHAD calculations.

In this work, the existing models are extended to describe the thermodynamics of stable binary and ternary phase diagrams and the metastable equilibrium state of the undercooled liquid. The available experimental data on the equilibrium phase diagram from the literature are evaluated and used as input data for CALPHAD modeling.

In the experimental work, different glass-forming alloy compositions from the glass forming region on the ternary diagram are selected, produced, and further characterized using a range of techniques, including calorimetry, where we employ methods such as Differential Scanning Calorimetry (DSC), Differential Thermal Analysis (DTA), and Flash-DSC (chip-calorimetry). Key thermal properties such as glass transition, crystallization, and liquidus temperatures; the enthalpies of crystallization and fusion, as well as the isobaric specific heat capacity of glassy, crystalline, and liquid states are determined and are used for the calculation of the thermodynamic functions of excess enthalpy, entropy and Gibbs free energy between the liquid and the crystalline mixture.

Subsequently, the CALPHAD approach is employed to calculate the driving force for crystallization at various compositions by applying the parallel tangent method to the Gibbs free energy of the crystalline and liquid phases. This method provides a more accurate estimation of the driving force for nucleation for the initial forming phase compared to the excess Gibbs free energy estimations based on experimental thermodynamic measurements. The calculated driving forces are then used for the modeling of the isothermal Time-Temperature-Transformation (TTT) diagrams, which yield the interfacial energy between the liquid and crystal during primary crystallization, an essential factor in understanding the glass-forming ability of the glass forming systems. Additionally, the study incorporates microstructural analyses using high-energy synchrotron diffraction experiments (HEXRD), which are compared with CALPHAD calculations to improve the accuracy of the modeling based on the observed phase formation results.

The findings of this work are presented in the results section and discussed in the discussion section in relation to existing literature. The outcomes are summarized in the conclusion section.

2 Bulk Metallic Glasses

In this section, a literature review on the topic of BMGs will be presented, which provides a theoretical basis and background information necessary to support the experiments conducted in the framework of this thesis.

2.1 Empirical Developments

In the early 1960s, while investigating the supersaturation of Au-Si solid solution, Duwez and his colleagues discovered a new class of metals [4]. These accidentally discovered amorphous metals, or metallic glasses, are essentially frozen liquids with disordered atomic structures, formed due to rapid cooling that should be fast enough to bypass the crystallization. These high cooling rates were achieved through rapid solidification techniques like melt spinning or splat quenching, resulting in cooling rates up to $10^6\ K/s$. However, this also limited the production of metallic glasses to a thickness below 1 mm due to the inverse relation between the critical thickness and critical cooling rate.

The breakthrough in the research of BMGs emerged with the discovery of multicomponent glass formers by Inoue and his team at Tohoku University [20–22], casting metallic glasses with higher critical thicknesses. The advancements in the critical casting thickness of glass-forming systems discovered between 1960 and 2000 are shown in Figure 2-1 with the PdCuNiP [22] system still owning the highest glass-forming ability.

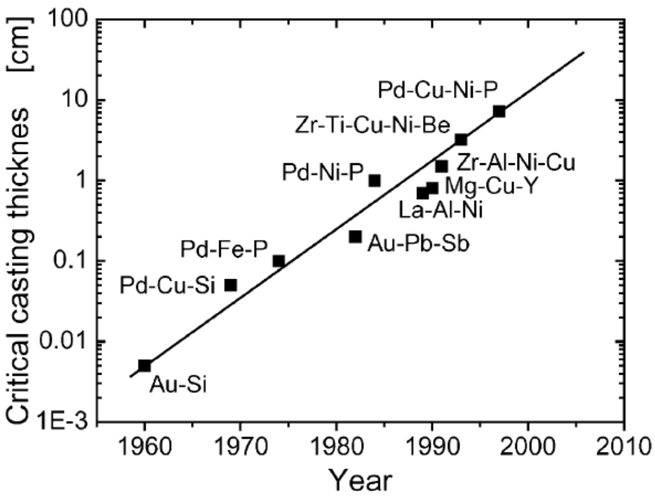

Figure 2-1. Advancements in the critical casting thickness of glass forming systems discovered between 1960 and 2000. Taken from [23].

The introduction of multicomponent bulk glass formers spurred extensive discussions on the mechanisms underlying BMG formation. Inoue proposed a comprehensive set of empirical rules for BMG formation based on a statistical analysis of hundreds of alloys with excellent glass-forming abilities [21] as follows:

- **Multicomponent Systems**: Alloys should consist of more than three elements. This complexity, referred to as the 'confusion principle', impedes the formation of a competing crystalline phase [24].
- **Atomic Size Difference**: There should be a substantial difference in atomic size ratios (greater than 12%) among the three main constituent elements. This increases the packing density in the liquid state and decreases average atomic mobility.
- **Negative Heats of Mixing**: The three main constituent elements should have negative heats of mixing, promoting the formation of a homogeneous glassy state.

In addition to these rules, good glass formers usually have compositions close to the eutectic points that correspond to a reaction from one liquid phase to two solid phases concurrently in the equilibrium binary phase diagram [25]. In practice, focusing on phase regions near deep eutectic points can expedite the discovery of good glass formers in binary and ternary alloy systems. This proximity to a eutectic reaction was highlighted by Turnbull and introduced as the reduced glass transition temperature parameter, $T_{rg} = \frac{T_g}{T_l}$, with T_g as the glass transition temperature and T_l as the liquidus temperature, in which a $T_{rg} = \frac{2}{3}$ indicates a good glass forming composition [26], since the melt becomes kinetically very sluggish and crystallization only occurs in a small range of temperatures, i.e. crystallization becomes more difficult. Therefore, a higher value of T_{rg} translates into a lower possibility of crystallization because of the shorter temperature range between T_g and T_l.

While these empirical rules are followed by most of the best glass formers, suggesting that certain physical principles are crucial in the formation of BMGs in multicomponent systems, they represent only the foundational aspects of glass formation. These rules are not comprehensive enough for the design of new alloys. Consequently, the precise physical mechanisms behind BMG formation remain unclear, and the quantitative laws for designing bulk metallic glasses are still unknown. In the following sections, we will go deeper into the glass formation process, exploring the thermodynamic and kinetic properties of undercooled liquids that govern glass formation.

2.2 Glass Transition Mechanism

The formation of metallic glasses is primarily a kinetic phenomenon rather than a thermodynamic one [27]. Typically, when cooling rates are slow, the equilibrium liquid cools below the liquidus temperature, resulting in a small degree of undercooling. At this stage, nuclei start to form and grow, leading to complete crystallization of the system and the release of the latent heat associated with crystallization. This typical cooling process for crystalline materials is shown in Figure 2-2, path 1, where extensive properties like volume, entropy, and enthalpy change abruptly, characterizing crystallization as a first-order phase transformation as indicated in the proposed thermodynamic classification scheme by Ehrenfest [28,29]. In Ehrenfest's scheme, the order of a phase transformation is determined by observing the behavior of the derivatives of the Gibbs free energy. Under continuous temperature change at constant pressure, which is slow enough for the system to reach internal equilibrium, the Gibbs free energy remains a continuous function of temperature. If the first derivative $(\frac{\partial G}{\partial T})_p$ changes abruptly at the transformation temperature, it is classified as a first-order transformation. In general, if all derivatives up to the n−1 order are continuous and the nth-order derivative is discontinuous at the transformation temperature, the transformation is classified as an nth-order transformation.

As known from basic thermodynamics, $(\frac{\partial G}{\partial T})_p = -S$ and $(\frac{\partial^2 G}{\partial T^2})_p = -\frac{(\frac{\partial H}{\partial T})_p}{T} = -c_p/T$, with S, H and c_p being the entropy, enthalpy and specific heat capacity. Therefore, in a first-order transformation like crystallization, a sudden change in entropy and enthalpy occurs. In contrast, a second-order transformation, like the magnetic Curie transition, features a continuous change in entropy but an abrupt change in specific heat at the transformation temperature. Figure 2-3 provides a graphical representation of the Ehrenfest classification scheme for the first and second-order transformations.

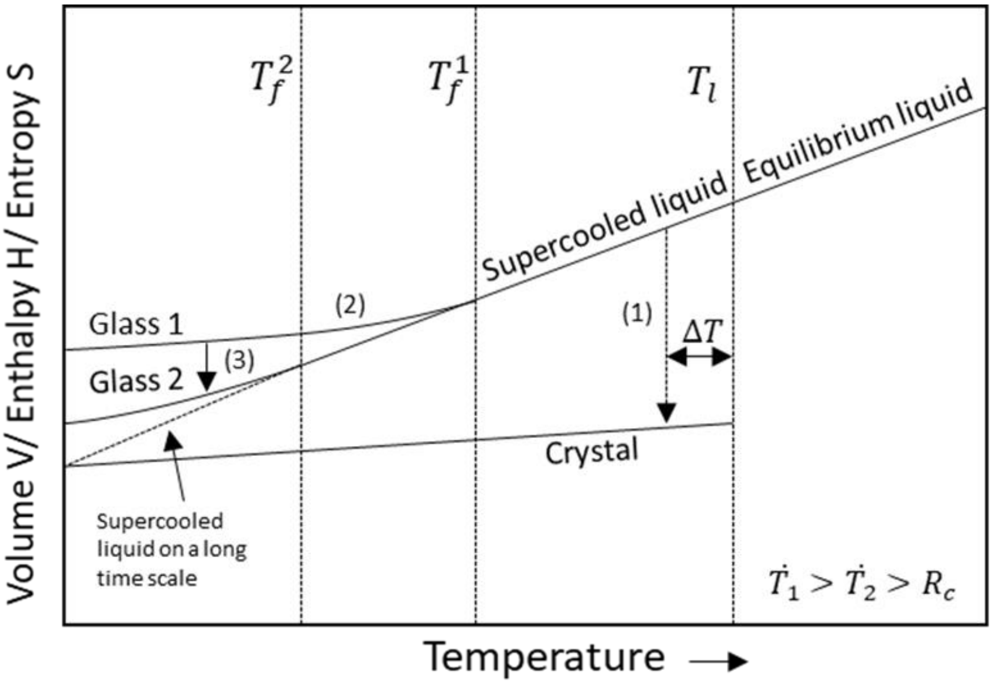

Figure 2-2. The schematic plot shows different solidification pathways as volume over temperature. Below the liquidus temperature (T), the liquid either crystallizes after some undercooling (ΔT, path 1) or transitions into a vitreous state (path 2). Another pathway (path 3) involves isothermal annealing, where the glassy state transforms into another glassy state through relaxation or physical aging. The fictive temperatures, marked as T_f^1 and T_f^2, correspond to the respective cooling rates and glassy states. Plotted based on [3].

In another scenario as in Figure 2-2, when the cooling rate is fast enough, crystallization is bypassed due to insufficient time for nucleation and growth. This keeps the liquid supercooled until it eventually forms a glass, during which extensive properties decrease continuously. Moreover, at the glass transition temperature (T_g) a noticeable change in the specific heat and thermal expansion coefficient is usually observed which will be discussed later. Based on this, from the previous discussion, the glass transition should be classified as a second-order transformation. However, the glass transition has unique characteristics. Unlike established second-order phase transformations, the temperature at which a supercooled liquid becomes glass, known as the fictive temperature, depends on the cooling rate [30]. As illustrated in Figure 2-2, higher cooling rates result in a higher glass transition temperature. For instance, Glass 1 has a higher fictive temperature than Glass 2 and a larger volume is preserved. Additionally, the c_p jump is not constant. It depends on the relaxation state of the glass, including the rates of cooling and heating through the transition range and any annealing the glass has undergone. Consequently, it has been argued [17-19] that the glass transition is not a second-order transformation but rather a kinetic phenomenon.

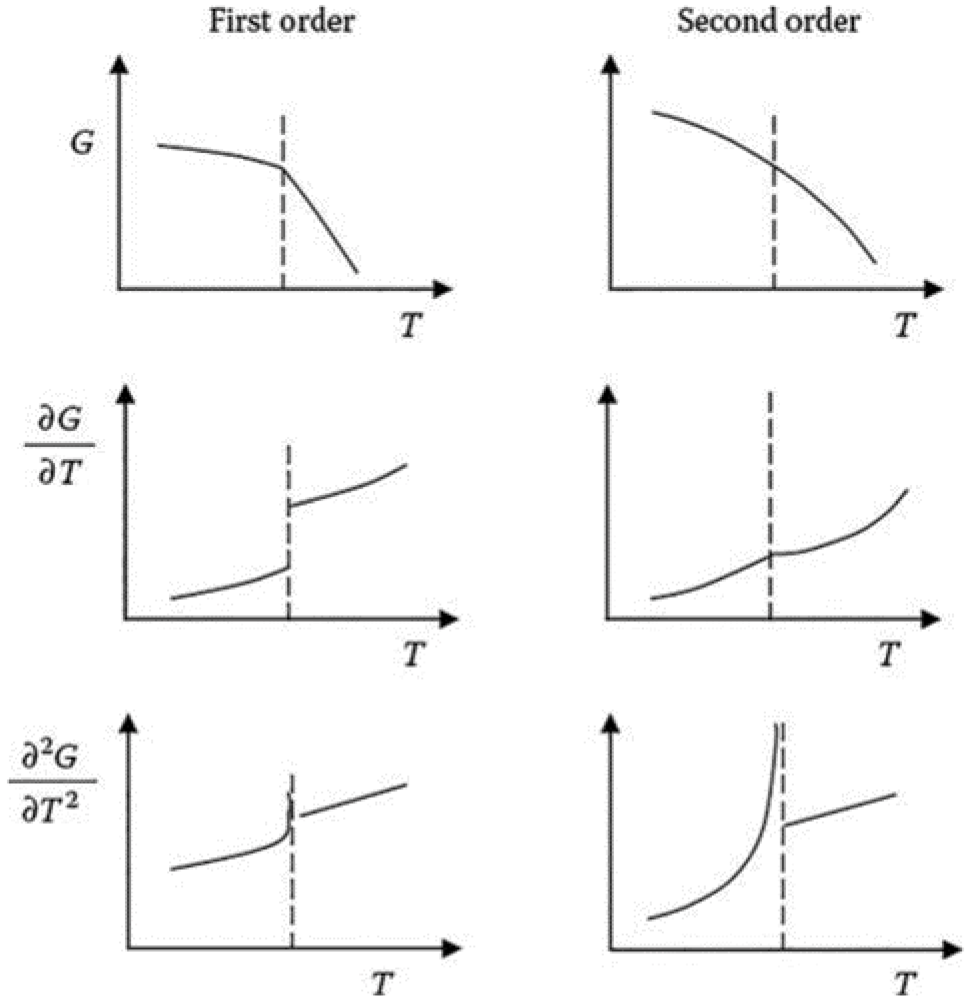

Figure 2-3. Changes in the Gibbs energy *G* and its derivatives with temperature for the first- and second-order phase transitions based on the Ehrenfest scheme. It's important to note that during a first-order transition, the Gibbs free energy (G) changes slope at the transition temperature, indicating a discontinuity in the first derivative. However, during a second-order (continuous) transition, the slope of G does not change at the transition temperature , meaning the first derivative remains continuous, though the second derivative exhibits a discontinuity. Taken from [31].

As depicted in Figure 2-2, glass 2 can also be obtained by annealing glass 1, as shown in path 3, where holding the glass at a certain temperature for a period allows the atoms to relax into a more densely packed structure, resulting in a lower volume. This process is known as physical aging or relaxation.

The glass formation and the associated volume change can be attributed to the changes in atomic mobility as a function of temperature. As shown in Figure 2-4, as the temperature decreases and the atomic dynamics slow down, the viscosity and inherent relaxation time of the supercooled liquid increase dramatically. At a certain point, the system can no longer follow the changes imposed on the system by the fast cooling rate and falls out of equilibrium, resulting in the formation of a glassy solid. This transition typically occures at a viscosity of around 10^{12} Pa s and a relaxation time of approximately 10^2 s [32,33].

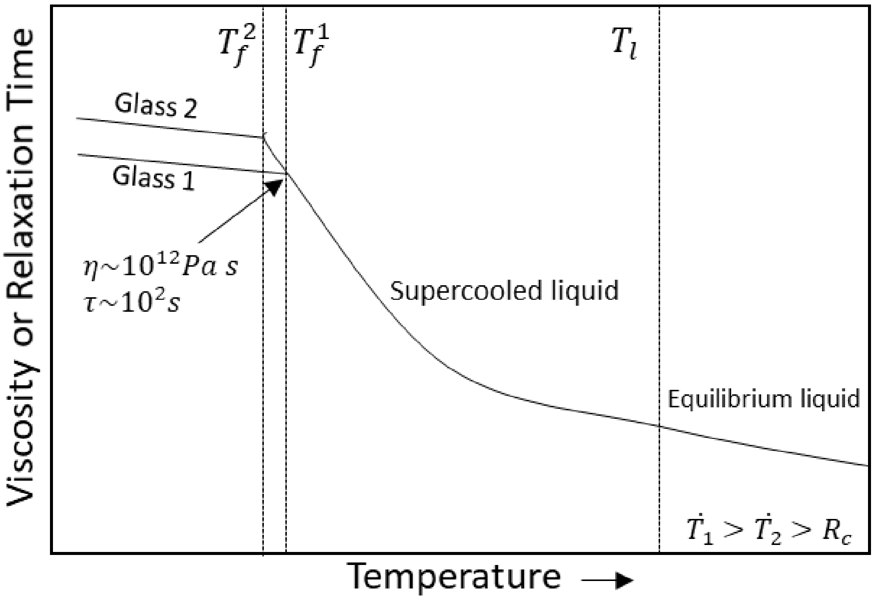

Figure 2-4. Schematic description of the changes in viscosity η and relaxation time τ of the liquid in different stages as a function of temperature. As temperature decreases, both η and τ rapidly increase due to a decrease in atomic mobility. At the glass transition, with a viscosity around 10^{12} Pa.s and a relaxation time of about 10^2 s, vitrification occurs, causing the system to fall out of metastable equilibrium due to the crossover of the inherent and applied timescales. Plotted based on [3].

2.3 Thermodynamics of Glass Forming Liquids

From a thermodynamic perspective, bulk glass formers inherently show a low driving force for crystallization in the supercooled liquid state. This driving force, as shown in Figure 2-5 (a), arises from the difference in Gibbs free energy between the liquid, $G_l(T)$, and the crystalline state, $G_x(T)$, below the liquidus temperature, T_l. As the undercooling increases, the difference between $G_l(T)$ and $G_x(T)$ grows, which in turn raises the likelihood of the liquid crystallizing within a finite time frame. These Gibbs free energies can be described as

$$G_{l/x}(T) = H_{l/x}(T) - S_{l/x}(T) \qquad \textbf{(2-1)},$$

in which $H_{l/x}(T)$ and $S_{l/x}(T)$ are the enthalpy and entropy of the liquid and crystalline state as a function of temperature. Subsequently, the Gibbs free energy difference between liquid and crystalline state is calculated as

$$\Delta G^{l-x} = G_l(T) - G_x(T) = H_l(T) - TS_l(T) - H_x(T) + TS_x(T) = \big(H_l(T) - H_x(T)\big) - \big(TS_l(T) - TS_x(T)\big) = \Delta H^{l-x}(T) - T\Delta S^{l-x}(T) \qquad \textbf{(2-2)}.$$

The enthalpy and entropy difference between the (undercooled) liquid and the crystalline state, $\Delta H^{l-x}(T), \Delta S^{l-x}(T)$, are calculated as [7]

$$\Delta H^{l-x}(T) = \Delta H_m + \int_{T_l}^{T} \Delta c_p^{l-x}(T')dT' \qquad \textbf{(2-3)},$$

and $\Delta S^{l-x}(T) = \Delta S_m + \int_{T_l}^{T} \frac{\Delta c_p^{l-x}(T')}{T'} dT'$, **(2-4)**,

where ΔH_m and ΔS_m represent the enthalpy and entropy of fusion at liquidus temperature T_l, the temperature at which the crystal and the liquid are considered to be in thermodynamic equilibrium and $\Delta S_m = \frac{\Delta H_m}{T_l}$. The parameter Δc_p^{l-x}(T) denotes the specific heat capacity difference between the (undercooled) liquid and crystalline state, which can be measured using thermal analysis methods, as discussed in the following chapters. However, a schematic description of the changes in c_p with temperature is shown in Figure 2-5 (b). By rapidly cooling the material, the undercooled liquid can bypass the crystallization process and undergo a glass transition, solidifying into a glassy state. In bulk metallic glasses, the specific heat capacity of the undercooled liquid has been found to increase as the temperature decreases, which is contrary to Debye's model [34]. This anomaly can be attributed to the formation of SRO and a decrease in both free volume and configurational entropy [34,35]. The temperature dependence of heat capacity at low temperatures (well below 273K) for the solid state (both glass and crystal), can be described by the Debye model, which reaches a value close to 3R = 24.94 J g-atom^{-1} K^{-1} at ambient temperature, in agreement with Dulong-Petit's law [36].

For small undercoolings up to 100 K [35], Turnbull approximation [37] can be used. In this approximation, the difference in specific heat capacity between the liquid and crystalline states is assumed to be negligible ($\Delta c_p^{l-x} \approx 0$). Under this assumption, the Gibbs free energy difference between liquid and crystalline state, ΔG^{l-x}, can be approximated as

$$\Delta G^{l-x}(T) = \Delta H^{l-x}(T) - T \times \Delta S^{l-x}(T) = \Delta H_m - T\frac{\Delta H_m}{T_l} = -\Delta S_m \Delta T \qquad \textbf{(2-5)}.$$

As $-\Delta S_m$ corresponds to the slope of $\Delta G^{l-x}(T)$ curve at T_l in Figure 2-5 (a), this equation allows for an initial estimation of the driving force for crystallization in an alloy with only knowing ΔS_m from experimental methods and without the need to determine the specific heat capacity difference Δc_p^{l-x} (Figure 2-5 (a)).

In general, high GFA is associated with small values of ΔG^{l-x} [38,39]. In Figure 2-6, the Gibbs free-energy difference for eutectic and near eutectic alloys with different critical cooling rates is shown [40]. The alloys exhibit different critical cooling rates, ranging from 1 K/s for Vit1 to approximately 10^4 K/s for the binary $Zr_{62}Ni_{38}$. Alloys with lower critical cooling rates show smaller Gibbs free-energy differences relative to the crystalline state compared to those with higher critical cooling rates. Increasing the bulk metallic glass-forming ability is aligned with a reduced driving force for crystallization. This primarily stems from the lower entropy of fusion ΔS_m, which indicates the negative slope of the free energy curve at the melting point. The low entropy of fusion of these deep eutectic bulk metallic glass-forming systems in the melt suggests that they already contain a small free volume and are prone to develop chemical short-range order at their melting point. These findings align with the assumption that in multicomponent systems, the crystalline phases depict relatively large configurational entropies of mixing. Additionally, they are consistent with the fact that bulk metallic glass formers are very viscous and relatively dense liquids at their melting point and during undercooling [40,41].

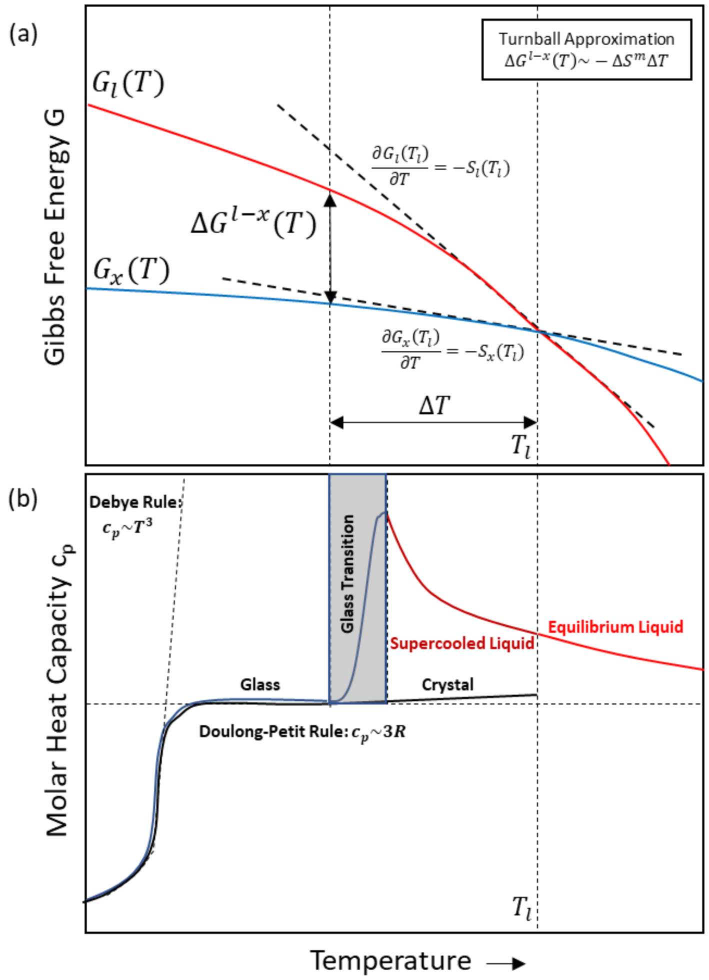

Figure 2-5. Schematic description of the changes in a) Gibbs free energy of the liquid $G_l(T)$ and crystal $G_x(T)$ in different stages as a function of temperature. As temperature decreases, at a certain undercooling, the Gibbs free energy difference between liquid and crystal, ΔG^{l-x}, can be approximated by the difference between slopes of $G_l(T)$ and $G_x(T)$ at T_l, namely $\Delta S^m = S^l(T_l) - S^x(T_l)$, b) Molar heat capacity of the crystalline mixture, the glassy state, the SCL, and the equilibrium liquid as a function of temperature. The changes of c_p in the solid state can be described by Debye and Doulong-Petit's rule based on the temperature range. Plotted based on [42].

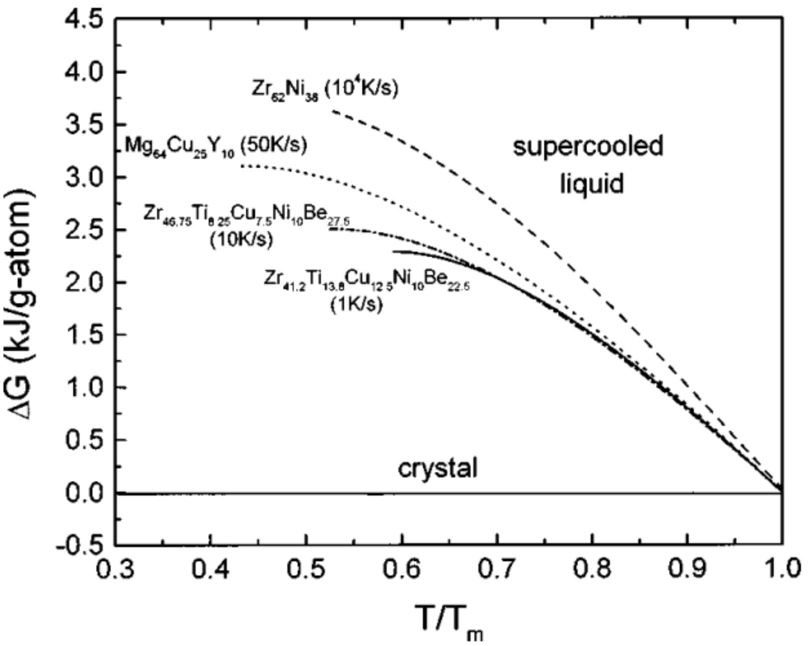

Figure 2-6. Gibbs free-energy difference between the supercooled liquid and the crystalline state for eutectic and near eutectic alloys with different critical cooling rates. Taken from [40].

2.4 Kinetics of Glass Forming Liquids

As previously noted, the transition from the melt to the glassy state cannot be classified as a second-order thermodynamic phase transition, despite the discontinuity in specific heat at the glass transition. The glass transition temperature varies depending on the experimental cooling or heating rate. To more accurately assess the GFA of BMG systems, it is essential to study the kinetics, particularly the temperature-dependent atomic mobility in these alloys. From the perspective of kinetics, the temperature-dependent mobility of the atoms in a metallic liquid can be described by the parameters such as the dynamic viscosity $\eta\ (T)$, the diffusion coefficient D(T), and the structural alpha-relaxation time $\tau_\alpha\ (T)$.

Viscosity $\eta\ (T)$ and diffusion coefficient D(T) are linked through the Stokes-Einstein relation described as [43]

$$D = \frac{\kappa T}{6\pi\eta r} \qquad \textbf{(2-6)},$$

with κ as Boltzmann's constant and r as the atomic radius of the respective element in the metallic liquid. For high undercoolings due to decoupling of the diffusivities of the different constituents, some liquids show a breakdown of this relation [44–46].

Through Maxwell relation, $\eta\ (T)$ and $\tau_\alpha\ (T)$ can be connected as [47]

$$\eta = G_\infty \tau_\alpha \qquad \textbf{(2-7)},$$

with G_∞ being the high frequency shear modulus.

The temperature dependency of η and τ_α, can be described by the empirical Vogel-Fulcher-Tammann equation (VFT equation) [48] as

$$\mathrm{x(T) = x_0 exp\ (\frac{D^*T_0}{T-T_0})} \qquad \textbf{(2-8)},$$

with $\mathrm{x_0}$ (τ_0 and η_0) being the relaxation time and viscosity limit at infinite temperature, respectively.

η_0 can be calculated as follow

$$\eta_0 = \frac{N_a h}{V_m} \qquad \textbf{(2-9)},$$

with N_a being the Avogardo's constant, h the Planck's constant and V_m the molar volume [49]. D^* is the fragility parameter, showing the derivation of the VFT equation from a pure Arrhenius behavior with a temperature-independent activation energy, and $\mathrm{T_0}$ is the VFT temperature at which η or τ diverges.

By measuring the temperature dependency of equilibrium viscosity or structural relaxation and fitting the data with VFT equation, we acquire the D^* value for different liquids and can classify them in terms of their **kinetic fragility**. In this concept introduced by Angell, liquids showing a rapid increase in viscosity and the associated relaxation time during cooling, are termed as **fragile** liquids with a low value of D^* . Liquids featuring a slower increase in viscosity or relaxation time during cooling until approaching glass transition temperature T_g with showing a higher value of D^*, are termed as **strong** liquids, which indicates their less temperature-sensitive structure.

This classification of liquids based on their fragility parameter is visualized in the so-called Angell plot for different glass-forming systems, as shown in Figure 2-7. The plot shows the logarithmic viscosity as a function of inverse temperature which is normalized to the glass transition temperature T_g^*, the temperature at which the supercooled liquid reaches a viscosity value of 10^{12} Pa s. As illustrated in Figure 2-7, SiO_2 serves as an excellent example of a strong liquid with a $D^* \sim 100$ [40]. It possesses a network structure with strong directional bonds that are resistant to temperature variations, resulting in a behavior that closely follows the Arrhenius behavior. On the other hand, fragile liquids, like o-terphenyl, deviate strongly from a pure Arrhenius behavior, and are highly sensitive to temperature changes around T_g, and have small fragility values of $D^* \sim 5$ [50].

Compared to oxide glasses, metallic liquids have weaker orientational constraints between their atoms and hence show a lower range of kinetic fragilities from intermediate values of $20 \leq D^* \leq 36$ [40,51] to very low values below a D^* of 20 [52–54]. The melt viscosity of BMGs is also in the order of 2–5 Pa s, about three orders of magnitude more viscous than pure metals, which usually have viscosities of the order of 10^3 Pa s [55].

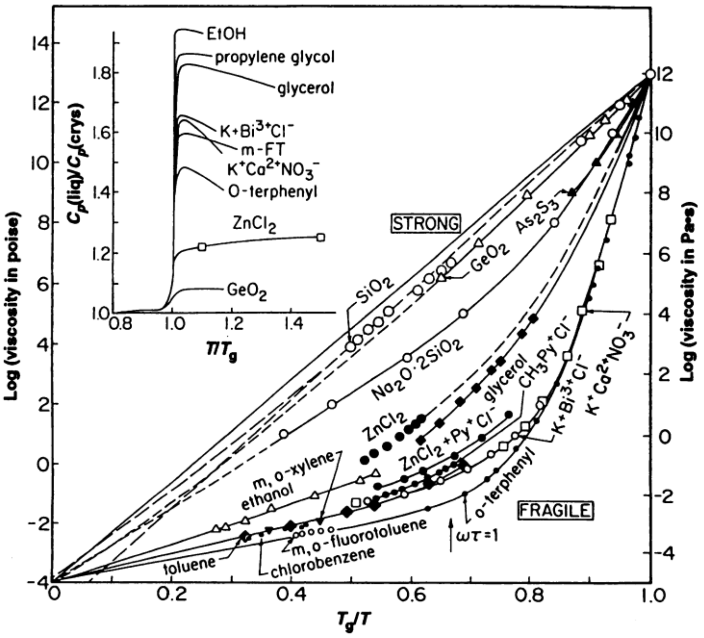

Figure 2-7. The so-called Angell plot, showing the changes in viscosity data for different alloys scaled by T_g^*. The inset shows the jump in c_p at T_g, which is in general large for fragile liquids and small for strong liquids. Taken from [48].

Another measure parameter of kinetic fragility is the fragility index m, which describes the slope of the VFT fit at the glass transition temperature T_g^* [26], and is expressed as

$$m = \frac{\partial log_{10}(x(T))}{\partial \frac{T_g^*}{T}} \quad \textbf{(2-10)},$$

where higher m values are indicator of a higher temperature sensitivity of the $x(T)$ around T_g and a more fragile liquid. This m value can be connected to D^* through following relation

$$m = \frac{D^* T_0 T_g^*}{\ln(10)(T_g^* - T_0)^2} \quad \textbf{(2-11)}.$$

Another approach for describing the non-Arrhenius behavior of viscosity (η) and the primary relaxation time (τ_α) is the Adam-Gibbs (AG) theory [56]. According to this theory, the supercooled liquid consists of groups of atoms that form cooperatively rearranging regions, adopting different configurations. As the liquid is further undercooled, these regions increase in size, requiring higher cooperativity for the relaxation process, which leads to a growing scarcity of available configurations [57]. This theory can be expressed as

$$f(\approx MD^{-1}) = f_0 \exp\left(\frac{C}{TS_c(T)}\right) \qquad \textbf{(2-12)},$$

in this relation, M is the factor reflecting the Einstein relationship between diffusivity and mobility, D is the diffusivity, f_0 holds the same context and value as the VFT pre-exponential factor (x_0) in Eq. (2-8), C is the free energy barrier for the cooperative rearrangements and $S_c(T)$ is the configurational part of the entropy of the liquid, whose loss with decreasing temperature explains the dramatic increase of η or τ_α upon approaching T_g. Since the temperature dependence of configurational entropy cannot be determined experimentally, it is often approximated by many authors [58,59] as the excess entropy of the liquid compared to the corresponding crystal, $\Delta S^{l-x}(T)$, by considering it purely configurational and neglecting the vibrational contribution.

In the work by Gallino et.al [1], the required configurational entropy of the liquid is calculated by the following equation

$$S_c(T) = S_cT_m^* - \int_T^{T_m^*} \frac{\Delta c_p^{l-x}(T')}{T'} dT' \qquad \textbf{(2-13)},$$

assuming a decrease in $S_c(T)$ during the undercooling from the fixed value of $S_cT_m^*$ with the same rate as the entropy difference between the liquid and the crystal. The value $S_cT_m^*$ is a property unique to the liquid phase, defined for a specific viscosity value of 1 Pa s (given that the melt viscosity of multicomponent BGM formers is usually higher). The underlying assumption is that the changes in vibrational contribution to the total entropy of the supercooled liquid with undercooling follow approximately a similar rate as that of the vibrational contribution of the crystal's entropy. This assumption is considered more appropriate than directly using the excess entropy change between the liquid and the crystal, and its validity has already been shown for Zr-based metallic glass-forming liquids [60]. Through this approximation, only the free enthalpy barrier to cooperative rearrangements C and $S_cT_m^*$ are left as fitting parameters. Figure 2-8 (a) shows the result of their work, plotting Fragility parameter (D^*) vs free activation energy per particle to cooperative rearrangements (C) , derived from the fit of Adam–Gibbs equation to the viscosity data for the investigated BMG forming liquids. As could be seen, a stronger glass is accompanied by a larger C, supporting the idea that in strong liquids, flow events are more localized, requiring a higher activation barrier to be overcome.

Figure 2-8 (b) shows the changes in the normalized configuration entropy plot of the investigated BMG forming liquids as a function of normalized temperature. They found that the T_0 from the VFT fits aligns very well with the temperature, at which the configurational entropy becomes zero in the Adam–Gibbs fits, which suggests the same microscopic origin and connects the kinetic and thermodynamic aspects of fragility.

Through these findings, one can see that the fragility parameter is connected to both kinetic and thermodynamic characteristics. The thermodynamic characteristic is normally correlated to the jump in specific heat capacity at $\mathrm{T_g}$ with the assumption $c_p^g(T) \sim c_p^x(T)$ (see Figure 2-5 (b)) [48,61], which is found to be larger in case of fragile liquids in comparison to strong liquids [48] as depicted in the inset of Figure 2-7.

From the kinetic characteristic (C), a more fragile behavior is connected to a more rapidly changing $S_c(T)$. In this regard, the sequence of the curves in Figure 2-8 (b) shows the general trend in the VFT plot of the corresponding compositions, going from the stronger Zr-based glass formers to the more fragile Pt-based and Pd-based glass formers, from left to right, indicating a proportional change of kinetic fragility and $S_c(T)$.

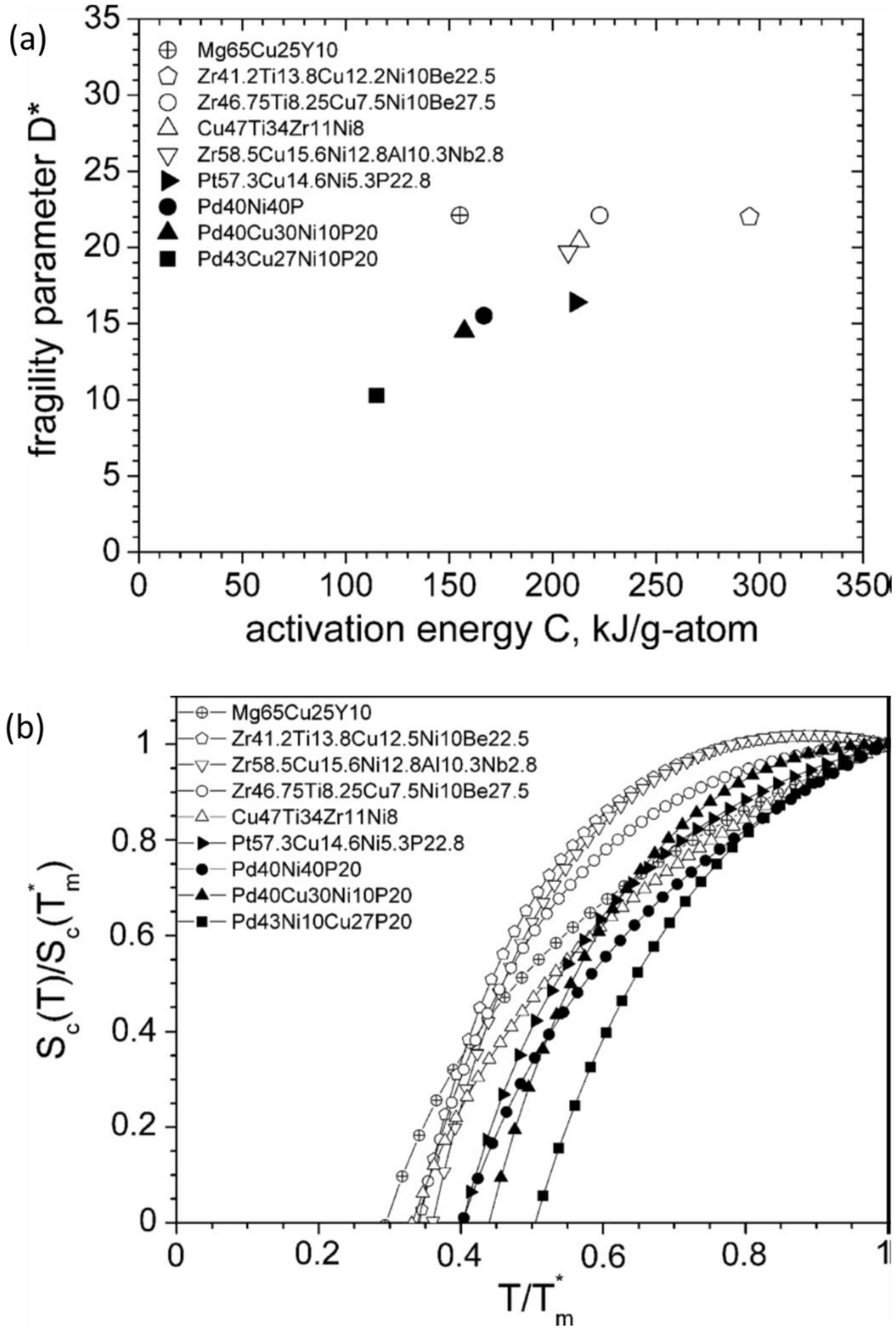

Figure 2-8. Results of [1], (a) Fragility parameter (D^*) vs free activation energy per particle to cooperative rearrangements (C) derived from the fit of Adam–Gibbs equation to the viscosity data for the investigated BMG forming liquids, (b) changes in normalized configuration entropy plot of the investigated BMG forming liquids as a function of normalized temperature.

2.5 Crystallization of Glass Forming Liquids

To understand the thermal stability and GFA of BMGs, it is essential to elucidate the crystallization behavior of the supercooled liquid. In this regard, the GFA describes how easily crystallization can be avoided during cooling, enabling the formation of a glass, which can be measured by the critical maximal casting diameter (d_c) or the critical minimum cooling rate (R_c) required to produce a fully amorphous sample. On the other hand, thermal stability is attributed to the resistance to crystallization upon heating determined by the temperature interval between the start of crystallization temperature T_x and glass transition temperature T_g , ($\Delta T = T_x - T_g$). Hence, a thermally stable metallic glass exhibits a broad temperature window where it remains in the amorphous state. This allows for extensive experimental investigations of its properties before crystallization sets in.

The crystallization kinetics are influenced by three main factors: the driving force for crystallization ($\Delta G^{l-x}(T)$), the interfacial energy between the liquid and the crystal, and the atomic mobility in the melt.

The driving force for crystallization and atomic mobility, in terms of melt viscosity (η(T)) and relaxation time τ_α (T), have been discussed in previous sections. The interfacial energy between the liquid and the crystal creates a nucleation energy barrier for forming a supercritical crystalline nucleus. Together, these factors define the nucleation and growth of crystals in an undercooled melt.

Crystallization is controlled by both nucleation and growth processes. The nucleation of a crystal precursor (nucleus) can occur homogeneously or heterogeneously and is driven by energetic fluctuations in the liquid phase, making it a statistical process. Understanding these aspects of crystallization kinetics is crucial for comprehending the origins of the thermal stability and GFA in BMGs.

The change in the Gibbs free energy of the system after nuclei formation below the melting temperature is influenced by the driving force for crystallization $\Delta G^{l-x}(T)$ and the interfacial energy between the liquid and the crystal γ^{l-x}, as described by the following equation [62]

$$\Delta G = -V_s \Delta G^{l-x}(T) + A_{SL}\gamma^{l-x} \qquad \textbf{(2-14)},$$

with V_s being the volume of the solid phase and A_{SL} the area of the interface between the solid and the liquid. Attention must be given to $\Delta G^{l-x}(T)$, that is the volumetric difference in Gibbs free energy between the liquid and the crystal acquired from Eq. (2-2).

Assuming the formation of a spherical crystalline nucleus with a radius of r, the changes in Gibbs free energy of the system can be rewritten as

$$\Delta G = -4/3\pi r^3 \Delta G^{l-x}(T) + 4\pi r^2 \gamma^{l-x} \quad \textbf{(2-15)}.$$

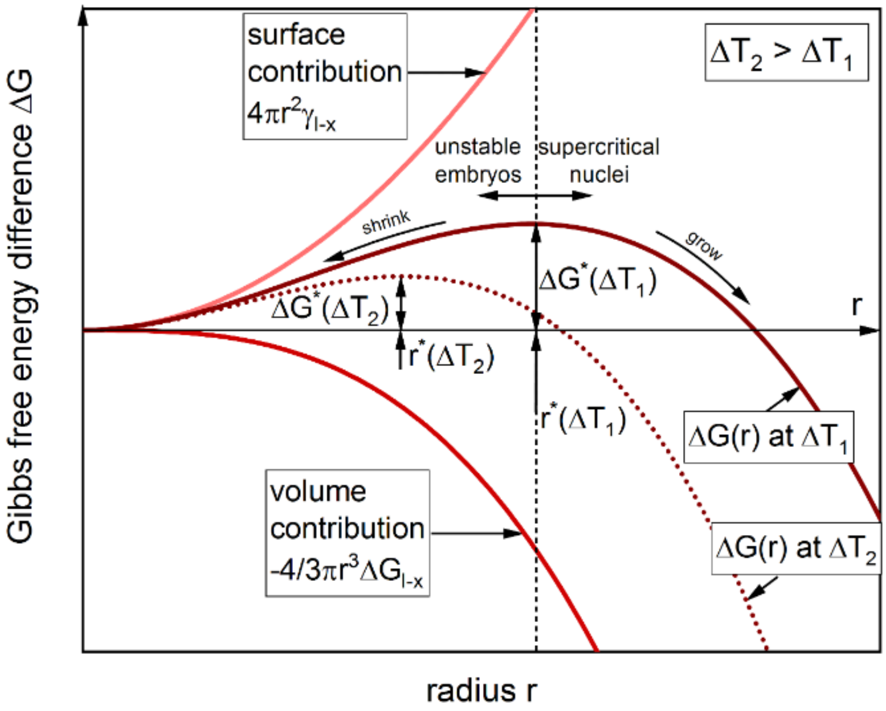

Figure 2-9. Gibbs free energy changes in a liquid imposed by the formation of a spherical crystalline nucleus with the radius r. The ΔG-curve contains a volume and a surface contribution. The critical radius r* represents the threshold below which nuclei are unstable. Clusters larger than r* are supercritical and will normally grow. Taken from [3].

The changes in Gibbs free energy of the liquid by the formation of the spherical crystalline nucleus with a radius of r is depicted in Figure 2-9. The critical radius r^*, which defines the smallest stable nucleus size, is determined by setting $\frac{\partial \Delta G}{\partial r} = 0$. At cluster sizes below this radius, the cluster remains an unstable embryo and the system can lower its Gibbs free energy by dissolving the cluster, however, above the critical radius a supercritical nucleus is formed that can grow and contribute to the crystallization of the entire liquid. At this critical radius, the Gibbs free energy barrier for nucleation, denoted as ΔG^*, is encountered. This barrier must be overcome to form a supercritical nucleus, which leads to the crystallization of the system. The r^* and ΔG^*functions are described as below

$$r^* = \frac{2\gamma^{l-x}}{\Delta G^{l-x}(T)} \quad \textbf{(2-16)},$$

$$\Delta G^* = \frac{16\pi {\gamma^{l-x}}^3}{3\Delta G^{l-x}(T)^2} \qquad \textbf{(2-17)},$$

which can be rewritten as below considering the Turnball approximation for the driving force of crystallization (Eq. 2-5) as a function of undercooling (ΔT)

$$r^* = \frac{2\gamma^{l-x} T_l}{\Delta H_m \Delta T} \qquad \textbf{(2-18)},$$

$$\Delta G^* = \frac{16\pi {\gamma^{l-x}}^3 {T_l}^2}{3{\Delta H_m}^2 \Delta T^2} \qquad \textbf{(2-19)}.$$

Based on the relationship of r^* and ΔG^* with undercooling, it can be concluded that the possibility of forming a supercritical nucleus rises as the undercooling increases, as illustrated in Figure 2-9. Additionally, from the ΔG^* equation, we can infer that interfacial energy is beneficial for glass formation γ^{l-x} , because it contributes as an energy barrier for crystallization.

In case of heterogeneous nucleation, the value of ΔG^*will be smaller, since the energy barrier is decreased due to a smaller interfacial energy between the solid and the liquid phase. Heterogeneous nucleation can be triggered by mold walls or impurities, which are challenging to avoid during the alloying and casting of BMGs.

Using information about the nucleation barrier, whether heterogeneous or homogeneous, and the atomic mobility within the system, one can calculate the nucleation rate $I(T)$ as

$$I(T) = Av(T)\exp\left(\frac{\Delta G^*}{k_B T}\right) \qquad \textbf{(2-19)},$$

with A being a constant, υ(T) the atomic jump frequency, and k_B the Boltzmann constant. The atomic jump frequency υ(T) signifies the rate at which atoms attach to a supercritical cluster, thereby representing the atomic mobility in the system, which is directly linked to the average atomic diffusion coefficient, D, which in turn relates to the viscosity through the Stokes-Einstein relation (Eq. 2-6). Replacing ΔG^* and υ(T) using Eq. 2-17 and Eq. 2-6 respectively, results in the following expression for $I_v(T)$

$$I_v(T) = A_v/\eta(T)\exp\left(-16\pi\gamma^{l-x}/(3k_b T[\Delta G^{l-x}(T)]^2)\right) \qquad \textbf{(2-20)}.$$

After the formation of stable nuclei, the Gibbs free energy of the system can be further reduced through the growth of crystallites, which involves minimizing energetically unfavorable interfaces. The growth rate $u(T)$ of the crystals can be expressed as [63]

$$u(T) = \frac{f}{a_0} D\left[1 - \exp\left(-\frac{\Delta G^{l-x}}{RT}\right)\right] \qquad \textbf{(2-21)},$$

where f is a constant reflecting the roughness of the interface between the crystal and the liquid and is considered equal to 1 if $\Delta S_m = \frac{\Delta H_m}{T_l} < 2R$ (rough interface) and $0.2\frac{(T-T_l)}{T_l}$ if $\Delta S_m = \frac{\Delta H_m}{T_l} >$

$4R$ (smooth interface) [63,64], a_0 corresponds to the average atomic diameter, and D is the atomic diffusivity.

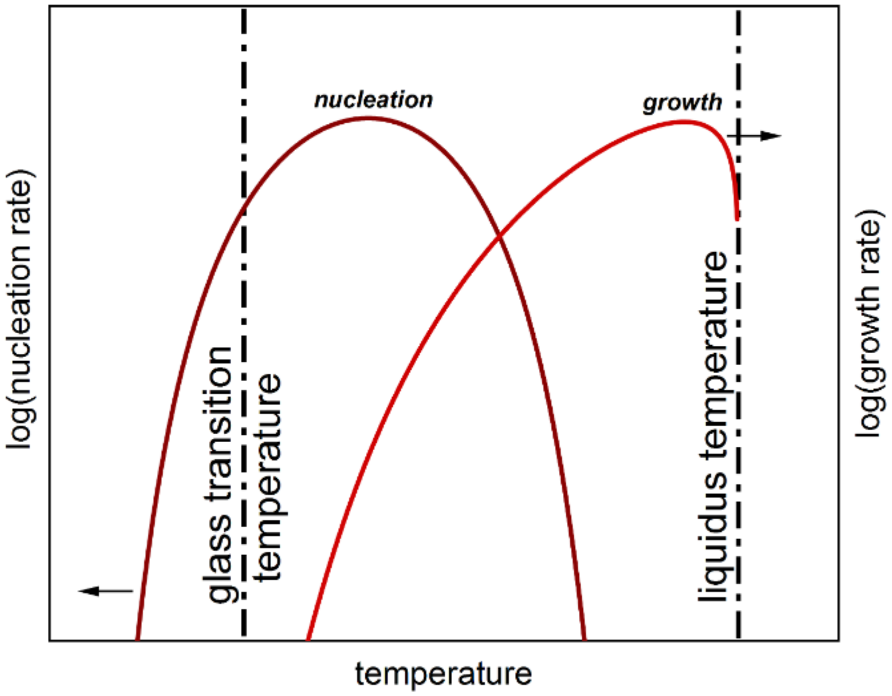

Figure 2-10. Changes of $I(T)$ and $u(T)$ as a function of temperature. At the liquidus temperature $\Delta G^{l-x} = 0$.Taken from [3].

Schematic change of $I(T)$ and $u(T)$ as a function of temperature in logarithmic scale, is illustrated in Figure 2-10. At higher temperatures and low undercoolings, atomic mobility is high and the Gibbs free energy difference between the liquid and crystal phases is small. Consequently, the nucleation rate is low, and crystallization is predominantly controlled by growth. In contrast, at lower temperatures, the higher driving force leads to nucleation dominating the crystallization process. This variation in controlling factors across temperature ranges commonly results in the observed dependence of crystalline microstructure on the degree of undercooling, in a way that greater undercooling tends to produce a finer-grained microstructure.

The crystallization process upon undercooling is controlled by the combined influence of $I(T)$ and $u(T)$ with the assumption that they are independent of time and the transformation is polymorphic [43]. For a given temperature T, the volume fraction X of the system that has crystallized in the time t, can be modelled by the Johnson-Mehl-Avrami-Kumogorov (JMAK) equation [43]

$$X(t) = 1 - exp\left[\frac{\pi}{3} I(T) u(T)^3 t^4\right] \qquad \textbf{(2-22)}.$$

This equation can be rewritten for a fixed volume fraction in the following form

$$t(T) = \left(\frac{-3\ln(1-x)}{\pi I(T) u(T)^3}\right)^{1/4} \qquad \textbf{(2-23)},$$

In which $t(T)$ can be illustrated as a function of temperature in the form of time-temperature-transformation (TTT) diagram, showing the typical C-shape [5] due to the competition between $I(T)$ and $u(T)$ with the nose bearing the minimum waiting time for crystal formation, shown as t_x^*, where growth and nucleation rate superimpose most constructively.

The nucleation rate and the growth rate are both influenced by two key factors: the thermodynamic contribution, which is expressed through the Gibbs free energy difference, and the kinetic contribution, which is governed by atomic diffusivity. Additionally, $I(T)$ is affected by the interfacial energy between solid and liquid γ^{l-x}. To visualize the impact of the mentioned parameters (atomic mobility, interfacial energy, and driving force for crystallization) on the crystallization time in the JMAK equation, Figure 2-11 displays three schematic TTT diagrams. Assuming the Turnbull approximation, Eq. 2-5, the driving force is represented via the entropy of fusion ΔS^m, the atomic mobility is represented via the kinetic fragility using the viscosity, and the influence of the interfacial energy between liquid and crystal is represented directly via γ^{l-x}.

System (1) in Figure 2-11 is indicative of a poor glass-former with a low GFA, and a minimum crystallization time of 1.7×10^{-8} s. Concerning the minimum crystallization time, $t_x^*(s)$, an empirical equation relating the crystallization nose time $t_x^*(s)$ to the critical casting diameter d$_c$ (mm) was developed by Johnson et al. [65] as

$$t_x^*(s) = 0.00419\ (d_c)^{2.54} \qquad \textbf{(2-24)}.$$

Using this relation results in a critical casting thickness of 7.5 µm for system (1), corresponding to the minimum waiting time for crystal formation, t_x^*. Alloys possessing a high driving force, a kinetically fragile liquid, and a low interfacial energy, are anticipated to exhibit these characteristics.

System 3) corresponds to an excellent glass-former with a critical casting thickness of 63 mm, whereas System 2) represents a good glass-former with an intermediate critical casting thickness among the three attributes. Systems exhibiting a strong liquid behavior, a high interfacial energy, and a moderate driving force for crystallization can all be linked to better glass formers having a high GFA.

The changes in glass transition temperature T_g , which is shown as T_g – dashed lines in Figure 2-11 is based on the mathematical expression

$$T_g = T_0 + \left(\frac{D^* T_0}{\ln\left(\frac{\tau_a}{\tau_a}\right)}\right) \qquad \textbf{(2-25)},$$

which is derived from the VFT equation and illustrates the changes in the glass transition temperature for liquids with various fragilities as depicted in Figure 2-11.

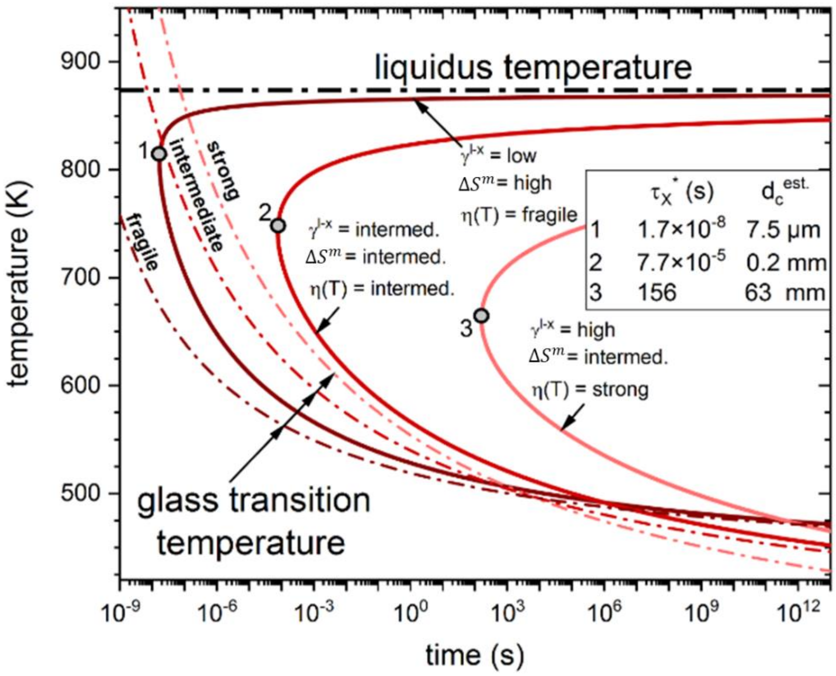

Figure 2-11. The effect of the interfacial energy (γ^{l-x}), the Gibbs free energy difference between the liquid and the crystal (ΔG^{l-x}, indicated by the entropy of fusion, ΔS^m), and the kinetic fragility of the liquid on the changes in crystallization nose in a TTT diagram. GFA gradually improves from system 1 to system 3 by varying these factors. Taken from [3].

So far, all the discussion focus was on homogeneous nucleation and the sole intrinsic characteristics of the liquid. When extrinsic variables are present, heterogeneous nucleation is anticipated, leading to a decreased nucleation barrier ΔG^*because the solid embryo adheres to the external interface. The reduced nucleation barrier $\Delta G^*_{het}$is expressed as

$$\Delta G^*_{het} = \Delta G^*_{hom} S(\theta) \qquad \textbf{(2-26)},$$

here $S(\theta) = \frac{(2+cos\theta)(1-cos\theta)^2}{4}$, and $0° < \theta < 180°$ is the wetting ability of the embryo, which has the biggest effect on the ΔG^*_{het} at low angels. The effect of the wetting angel on the ΔG^*_{het} is shown schematically in Figure 2-12, where a higher wetting angel results in a higher energy barrier.

Higher cooling rates are necessary for the production of amorphous samples in the event of potential heterogeneities, as Figure 2-13 schematically illustrates the effects of heterogeneous nucleation on the crystallization nose in the TTT diagram and, subsequently, the critical cooling rate (CCR) [66,67]. Heterogeneous nucleation has been found to be avoided by the use of high purity elements [67,68], melting alloy in B_2O_3 (fluxing) [69], and water quenching in SiO_2 [70] as opposed to traditional copper mold casting.

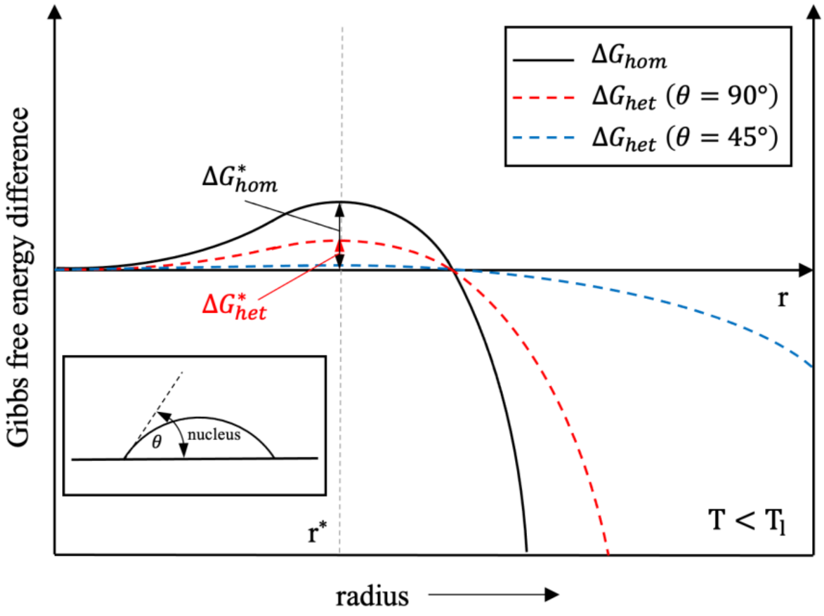

Figure 2-12. Schematic illustration of the effect of wetting angel on the reduction of the energy barrier for stable nucleus formation, considering heterogeneous nucleation. A higher wetting angel results in a higher energy barrier. Taken from [71].

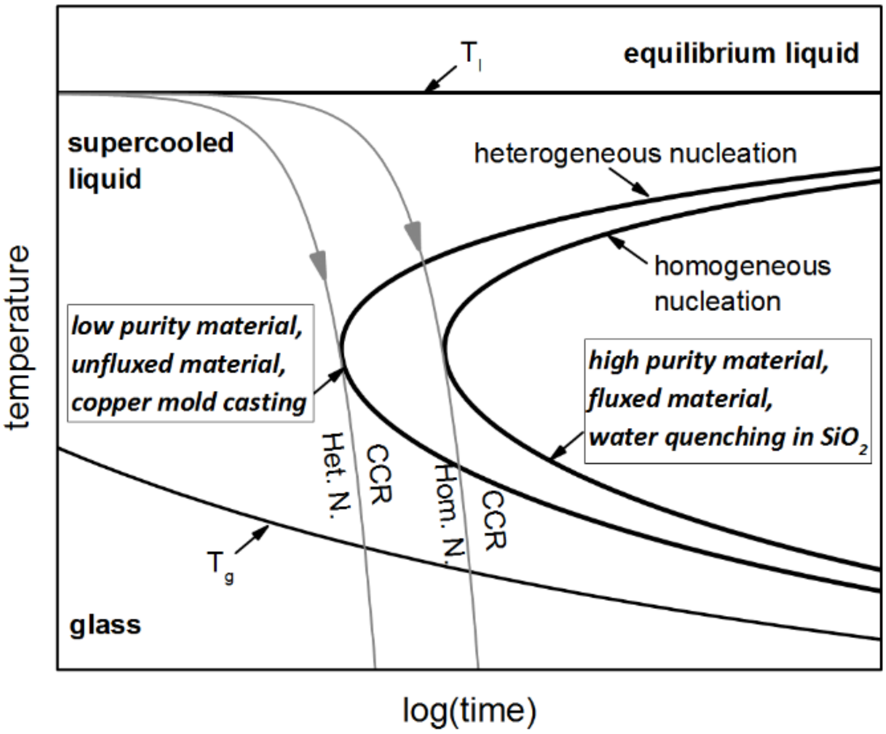

Figure 2-13. Schematic TTT diagram of a glass forming liquid, illustrating the effects of homogenous and heterogenous nucleation on the CCR and crystallization nose. Taken from [3].

2.6 Structure of Glass Forming Liquids

Since the discovery of metallic glasses in 1960 [4], their atomic structure has been a subject of inquiry. Unlike conventional crystalline metals that exhibit long-range periodic atomic arrangements, metallic glasses lack such order in their structure. As a result, no sharp Bragg diffraction peaks can be seen in their X-ray diffraction experiments, due to the random fluctuation of the atomic positions in their disordered atomic structure, which was already noticed for the first metallic glass produced in 1960. Understanding the atomic structure of metallic glasses is crucial as it directly influences their properties.

The atomic structure of metallic glasses is defined by short-range order (SRO) and medium-range order (MRO). SRO is defined based on the random packing model of hard spheres [72,73] and refers to the local arrangement of atoms around a central atom, basically in the form of icosahedral arrangements as local structural units (clusters), where twelve atoms surround a center atom. This local arrangement often resembles the structure in simple monoatomic liquids, where atoms considered as hard spheres are packed efficiently with irregular polyhedra but without the periodicity seen in crystals [74–76]. Simultaneously, for metal-metalloid glasses, trigonal prisms connecting via edge sharing as local structural units were proposed by Gaskell [77].

MRO, on the other hand, describes correlations between the SROs that extend beyond the immediate neighbors but do not reach the long-range periodicity of crystalline lattices [78].

Despite the development of various models to describe the structure of metallic glasses (MGs), verifying these local atomic structures remains challenging due to the limitations of experimental techniques. In 2013, Hirata et al. successfully obtained two-dimensional images of distorted icosahedral clusters in a representative $Zr_{80}Pt_{20}$ metallic glass using Angstrom-beam electron diffraction (ABED) for the first time [79] as shown in Figure 2-14. Interestingly, they found that most local atomic arrangements have an intermediate structure between the icosahedron and FCC (Face-Centered Cubic) to retain dense atomic packing and a low energy state.

Generally, the distortion of icosahedra has been attributed to atomic size disparity of constituent elements and/or kinetic fluctuation during glass formation, leading to variations in atomic bonding length, as well as atomic scale stress and strain in metallic glasses [80,81]. However, unlike the random geometric variations caused by the chemical and kinetic effects, the distorted icosahedra reported here consistently possessed partial FCC symmetry. This suggests that the distortion of icosahedra in the metallic glasses is related to the geometric frustration arising from the competition between two low-energy states (FCC and icosahedron) with dense atomic packing.

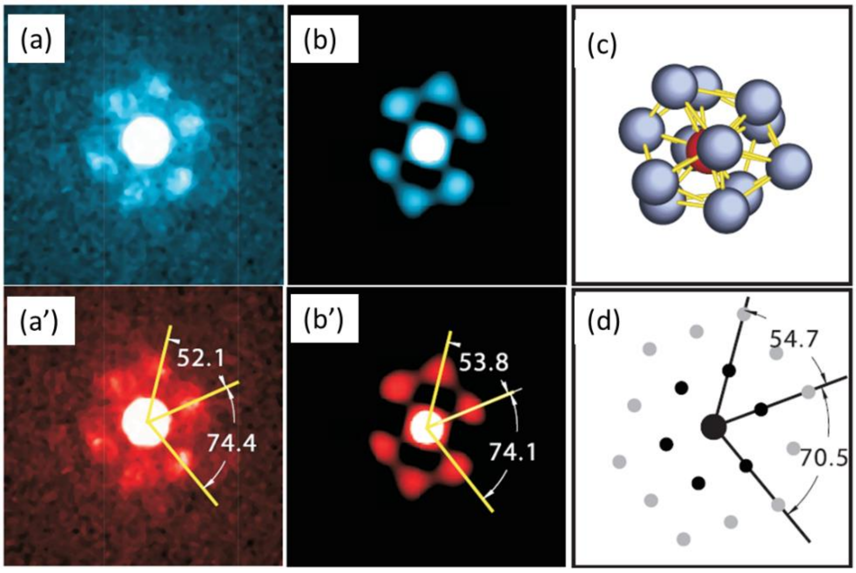

Figure 2-14. ABED patterns of a distorted icosahedron with an FCC-like orientation, a-a′) Experimental ABED pattern and the corresponding characteristic diffraction angles in the experimental ABED pattern obtained from $Zr_{80}Pt_{20}$, b-b′) Simulated ABED pattern and the corresponding characteristic diffraction angles in the simulated ABED pattern. c) Illustration of the distorted icosahedron producing the ABED pattern shown in (b). d) Calculated [110] diffraction pattern of a FCC cluster. Taken from [79].

The chemical variation and kinetic fluctuation may provide structural perturbations during the development of the intermediate atomic configuration by preventing the formation of the ideal icosahedron and FCC clusters. This atomic packing scheme, characterized by low structure symmetry but dense atomic arrangement, has not been observed in any crystal or quasicrystal and represents a unique atomic structural feature of metallic glasses. This proves that metallic glasses are essentially frozen supercooled liquids, and the local structure revealed by ABED corresponds to the inherent structure of the supercooled liquid just before it transitions to the glassy state.

In different alloy systems, the constituent elements, their size distribution, and their chemical interactions can lead to different local structural units or clusters. The solvent atoms around the central solute atom form different types of coordination polyhedra. The size ratio of the constituent elements influences the coordination number (Z) needed for efficient space filling. Figure 2-15 illustrates six different Kasper polyhedra corresponding to these coordination numbers [82].

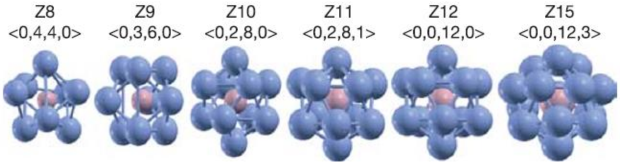

Figure 2-15. Kasper polyhedra corresponding to different coordination numbers (Z), which are the dominant coordination polyhedra in relaxed metallic glasses.Taken from [82].

The medium-range order (MRO), defined as the next-level structural organization beyond the SRO, is even less understood. MRO refers to the connection type of the local structural 'units' in a way that fills the three-dimensional (3D) space. Understanding the characteristics of the MRO remains one of the most significant questions in metallic glass (MG) research.

Based on Miracle's so-called efficient cluster packing (ECP) model [83] and its further elaboration [84], the efficiently packed solute-centered atomic clusters serve as local representative structural elements (RSE). These clusters are considered like spheres that are again densely packed to fill the 3D space, producing a quasi-periodic arrangement like a face-centered cubic or hexagonal close-packed structure, explaining the MRO. The first coordination shell can be shared between neighboring clusters to reduce internal strains. Additionally, the solvent atoms are located in random positions, while there is no orientational order between the clusters. Finally, in order to meet the requirements for topological SRO within the cluster, all solute atoms have a particular desired size ratio with respect to the solvent atoms, which are the majority species.

The Miracle model is purely based on geometrical considerations and ignores chemical effects. Ma et al. extended the idea of efficient cluster packing by incorporating the impact of chemical affinity on the SRO [82]. The simulated cluster assemblies for $Ni_{80}P_{20}$, $Ni_{81}B_{19}$, and $Zr_{84}Pt_{16}$ metallic glasses are shown in Figure 2-16. According to their findings, icosahedra fragments are present, which suggests an icosahedral-type MRO or cluster ordering. In a metallic glass with a high solute concentration, the dominant type of MRO can change. When solute-solute contacts become inevitable, the solute atoms make string-like structure arrangements, surrounded by solvent atoms. These so-called extended clusters can connect through edge-, vertex- or face sharing, which results in a different type of MRO [82].

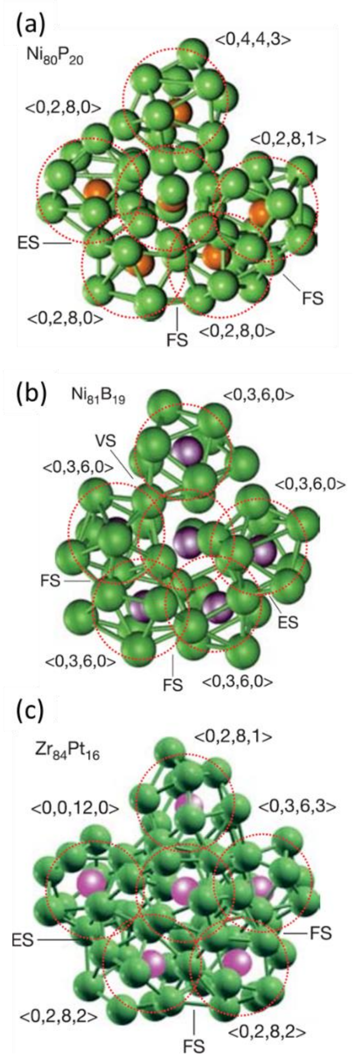

Figure 2-16. 3D model of an assembly of clusters in a) $Ni_{80}P_{20}$, b) $Ni_{81}B_{19}$, and c) $Zr_{84}Pt_{16}$ metallic glass. The solute (P, B, Pt) centered clusters, shown by the dashed circles, exhibit icosahedral type ordering as their MRO. The Voronoi index for each cluster is given in triangular brackets to indicate its identity. The combination of edge sharing (ES), vertex-sharing (VS), and face sharing (FS) between the clusters defines the MRO. Taken from [82].

One of the main techniques for studying the structure of metallic glasses is synchrotron X-ray diffraction, which has been in use for several decades. The underlying principle is discussed in Ref. [78]. The structural information is conveyed via the structure function, S(Q), as well as in the Fourier transformation of S(Q), the pair distribution function, G(r).

In general, the pair distribution function indicates the probability of finding an atom in the distance r from a reference atom. A common G(r)-curve for a metallic glass is presented in Figure 2-17. The first peak in G(r) is correlated to the first coordination shell around the central atom, while the second peak represents the second nearest-neighbor shell. The shape and position of the second peak in G(r) provide insight into the MRO and the prevailing cluster connection schemes

[85]. A splitting of the second peak is an indicator of different cluster connection schemes between neighboring clusters, such as the sharing of edges, faces, and vertices.

A recent study by Gross et al. [86] on compositionally comparable $Pt_{42.5}Cu_{27}Ni_{9.5}P_{21}$ and $Pd_{43}Cu_{27}Ni_{10}P_{20}$ alloys, in which Pt and Pd are considered to be topologically equivalent in structural models, revealed a change in the local representative structural unit with a change in alloy composition. In Pt-P-based liquids, trigonal prisms are the dominant representative structural unit, while the influence of icosahedral SRO increases with the replacement of Pt by Pd, resulting in the diminished presence of trigonal prisms.

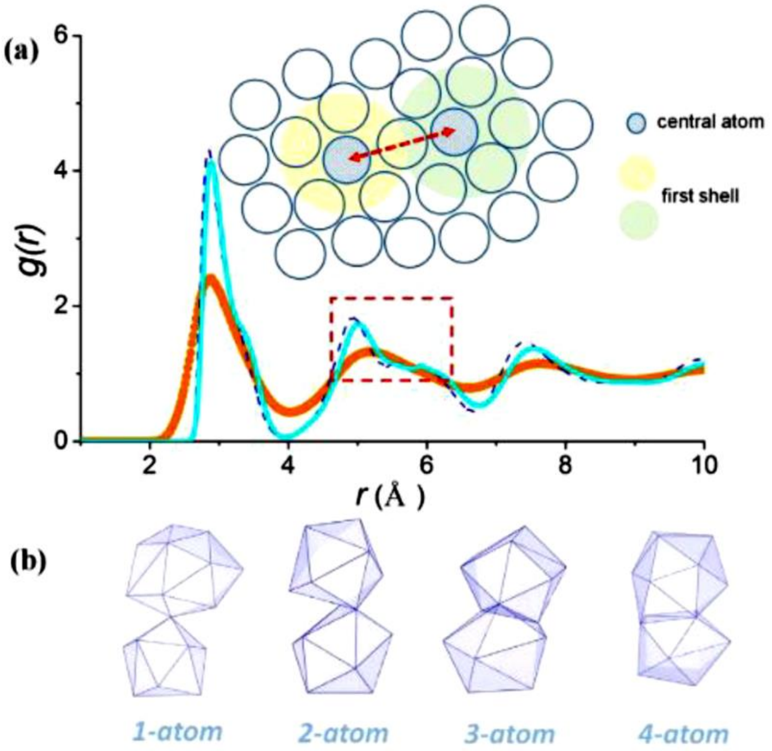

Figure 2-17. a) Simulated pair distribution function g(r) of amorphous Ta in liquid (orange) and glassy (Blue) states. The inset shows a 2D illustration of the atomic arrangement, highlighting the shells surrounding a central atom. The second peak in g(r) represents the distance to the second nearest neighbor, where both the liquid, and the glassy structure show a split, which is correlated to the formation of different connections between the atomic clusters. b) Schematic illustration of different cluster connection schemes between neighboring clusters, consisting of 1-atom, 2-atom, 3-atom, and 4-atom connections. Taken from [85].

3 CALPHAD Modeling

3.1 Introduction to CALPHAD

The CALPHAD (CALculation of PHAse Diagrams) method was first developed by Kaufman and Bernstein in 1970 [87] to address gaps in material science, especially in understanding phase equilibria and thermodynamics, where the phase diagrams are often only partially known at best. Initially, their models, consisting of the regular solution and stoichiometric models, were working to calculate phase equilibria within a reasonable time frame. Still, they could not accurately predict the physical properties of many phases, particularly those with short or long-range order. Many more computer programs for thermodynamic calculations were developed afterward in the 1970s and 1980s. Over time, these models have improved significantly to provide accurate thermodynamic descriptions with the help of experimental data. These developments also led to the creation of thermodynamic databases for commercial materials.

The integration of binary and ternary system descriptions into multicomponent databases depends on high-quality, reliable thermodynamic data. In Europe, efforts to develop a unified database led to the formation of SGTE (Scientific Group Thermodata Europe) [88], with Dinsdale [89] compiling reference data for pure elements for this group, which serves as the foundation for today's multicomponent databases.

The CALPHAD method describes the Gibbs energy and other properties of phases as functions of temperature, pressure, and composition. Its formalism allows for extrapolation to higher-order systems after defining binary, ternary, and quaternary systems. This makes it a powerful tool for alloy development and process design compared to traditional cost and time-consuming experimental methods. CALPHAD uses various experimental data and first principles results to fit the Gibbs energy, diffusion mobility, and other property functions of lower-order systems, which are then compiled into multicomponent databases. These databases are used widely to predict material properties and microstructure evolution, with the ongoing development of auxiliary property databases expanding their applications [90].

The strength of the CALPHAD method lies in being currently the only method available for efficient calculations in multicomponent, multiphase systems, with the accuracy needed for practical applications. Additionally, CALPHAD calculations can be used to acquire information about metastable equilibria and also the driving forces for the formation of the stable phases. This has made the CALPHAD method an essential tool for many industries and part of ICME (Integrated Computational Materials Engineering) [91]. The Materials Genome Initiative (MGI) [92], which was announced in 2011, emphasizes the importance of computational tools for the rapid and cost-effective development, manufacturing, and deployment of advanced materials. In this context, CALPHAD databases and software can be seen as an early materials genome [93–95].

The next section provides an overview of the thermodynamic models used to describe the Gibbs energy, which forms the foundation of CALPHAD applications in metallic glasses.

3.2 Thermodynamic Models

3.2.1 (Undercooled)Liquid and Amorphous State

To model glass forming liquids, it is important to understand the nature of the glass transition. As stated by Kauzmann in his classical article from 1948 [33], a glass can be defined as an amorphous or non-crystalline material in which certain internal degrees of freedom typical of the liquid state, lack enough time to reach thermodynamic equilibrium with their surroundings. Using this perspective as a basis for developing a phenomenological CALPHAD modeling of the glass transition for a pure substance, a thermodynamic model for the liquid/glass state should be selected first. Additionally, this model should be able to present the stable or metastable equilibrium state of the liquid in terms of the external control variables, such as pressure and temperature, as well as at least, one internal variable [96]. It should be noted that the modeling of the liquid phase has been a long-standing challenge for the CALPHAD community due to the disordered structure of the liquid and the progressive SRO and MRO, which lead to an increase in the heat capacity of the undercooled liquid. In this context, normally treating the glass transition as a second-order transformation, according to the thermodynamic scheme proposed by Ehrenfest [28], as discussed previously in section (2.2), where enthalpy, entropy, and Gibbs free energy show no discontinuity at T_g, but the specific heat does, is a good first approach. To date, experiments have shown this to be a reasonable first approximation and a practical modeling assumption [12].

The first class of thermodynamic models, known as the 1-state model, treats the liquid and glass as a single phase, where the liquid state exists above the glass transition temperature (T_g), and the glassy state exists below T_g. In this model, the Gibbs free energy of each phase φ is described by polynomials and is expressed as

$$G^{\varphi} = G_{ref}^{\varphi} + G_{id}^{\varphi} + G_{ex}^{\varphi} \quad \textbf{(3-1)},$$

where G_{ref}^{φ} is the contribution of the pure components of the phase φ, G_{id}^{φ} is the ideal mixing contribution and G_{ex}^{φ} is the excess Gibbs free energy of mixing, arising from non-ideal interactions between the components. All of these terms are temperature, pressure, and composition dependent, with varying empirical parameters based on the adopted model.

The use of polynomial basis thermodynamic functions has been widely accepted and applied as a standard mathematical representation of Gibbs energy of the pure elements. These thermodynamic assessments are documented in a database compiled by A. Dinsdale [89], known as the second-generation database. However, the properties of the undercooled liquid of pure elements are not known and the database relies on extrapolation for these temperature ranges. Based on that compilation, a wide range of databases for different kinds of materials (steels, slags, cemented carbides, etc.) in the second-generation database is established. Despite the successful application of these databases for decades, the empirical models used were valid only down to 298 K.

Regarding selecting a suitable thermodynamic model for the glass transition, the 1-state models that are reviewed by Palumbo and Battezzati [12], appear to be insufficient as they do not include any internal variable and do not describe the behavior of the undercooled liquid properly.

The second class of thermodynamic models consists of the 2-state models, which also is known as Two-Level Systems (TLS) in the CALPHAD research community. According to 2-state models, the liquid is characterized as a combination of two different kinds of structural entities: molecules or atoms, with the molar fraction of one or the other type of entity serving as the internal variable. This approach considers a gradual transformation of the liquid-amorphous state during cooling, from a condition in which most atoms or molecules are in a liquid-like state to a condition in which all the atoms or molecules are in a solid-like state. In the solid-like state, it is assumed that atoms or molecules have only vibrational degrees of freedom, whereas in the liquid-like state it is imagined they also have a large fraction of translational degrees of freedom. Thus, amorphous solidification corresponds to the gradual loss of translational degrees of freedom [97].

In the simplest version of the two-state model [96], the unary liquid is considered an ideal solution of these two types of structural entities, solid-like (A), and liquid-like (B) atoms or molecules which are in chemical equilibrium, and its Gibbs energy is expressed as

$$G^{liq} = \chi_A G_A + \chi_B G_B + RT(\chi_A ln\chi_A + \chi_B ln\chi_B) \qquad \textbf{(3-2)},$$

with χ being the respective entity's molar fraction. By introducing $\chi = \chi_B$, and $\Delta G_d = G_B - G_A$, G^{liq} could be rewritten as

$$G^{liq} = G_A + \chi\Delta G_d + RT\big((1-\chi)\ln(1-\chi) + \chi ln\chi\big) \qquad \textbf{(3-3)}.$$

The equilibrium value of χ is determined at each temperature by the condition of minimum Gibbs energy, $\frac{\partial G^{liq}}{\partial \chi} = 0$, as

$$\chi_e = \frac{\exp\left(-\frac{\Delta G_d}{RT}\right)}{1+\exp\left(-\frac{\Delta G_d}{RT}\right)} \qquad \textbf{(3-4)},$$

and finally, by inserting Eq. (3-4) into Eq. (3-3), the Gibbs energy of the liquid–amorphous state can be described as

$$G^{liq-am} = G_{am} - RTln\left[1 + \exp\left(-\frac{\Delta G_d}{RT}\right)\right] \quad \textbf{(3-5)}.$$

The solid-like atoms are considered to have the same c_p and the same entropy as the crystalline solid phase [98]. Hence, a mathematical representation comparable to that of the solid crystalline phase can be used for G_{am} as will be discussed in the next section (3.2.2). ΔG_d is also expressed as a temperature-dependent function given by

$$\Delta G_d = A + BT + CT\ln T + \cdots \quad \textbf{(3-6)},$$

with A, B, and C being the parameters that need to be optimized. Considering the empirical nature of this equation, if necessary more terms could be added to fit the experimental data. As a first approximation approach, one can fix the value of B to $-R$, the gas constant, which is referred to as the communal entropy. If it is not possible to fit the experimental data, by knowing the entropy of fusion experimentally, B can be put to $-\Delta S_m$ [89]. The experimental value for the enthalpy of fusion can be also used as the initial value for A [16,99].

Since Agren's pioneering work [100] and the Ringberg Workshops [101,102], the simple ideal 2-state model has been widely used in the CALPHAD community to describe the liquid state in connection with the development of the so-called "3rd generation databases" for pure elements and few binary compositions [16,97,99,103–107], which provides a sounder physical basis for the description of the Gibbs energy [97]. However, not all liquids can be characterized by an ideal 2-state model, and it seems to be a more promising modeling option for liquids classified as fragile liquids [108].

So far, there haven't been many studies on extending the two-state model to ternary compositions. Only one study by Alvares et al. [98] has used the two-state model to describe the liquid phase of the Fe-Nb-B system which still lacks adequate experimental data for the (undercooled)liquid assessment.

The third class of the thermodynamic models, which is mostly used for oxides, is based on a bond lattice model for analyzing the structure of condensed matter introduced by Angell and Rao [109]. In this context which is based on the 'configuron' concept, a configuron refers to a fundamental configurational excitation that occurs when a chemical bond is broken. The Configuron Percolation Theory (CPT) further developed by Ojovan et al. [110] builds upon this bond lattice framework and considers the glass transition as a percolation of broken bonds. Formally, these types of models can also be viewed as 2-state models, where the high energy state corresponds to the broken bond and the low energy state represents the intact bond, which is in contrast to the more conventional particle lattice models that focus on the configurational states of individual atoms or molecules.

3.2.2 Solid State

According to the model developed by Chen and Sundman [103], the description of Gibbs energy of the solid phase can be derived from the function of heat capacity which can be expressed for the temperature range below the melting point as follows

$$c_p = 3R\left(\frac{\Theta_E}{T}\right)^2 \frac{e^{\frac{\theta_E}{T}}}{(e^{\frac{\theta_E}{T}}-1)^2} + aT + bT^n + c_p^{mag} \qquad \textbf{(3-7)},$$

in which Θ_E is the Einstein temperature of the solid phase. The harmonic lattice vibration is represented by the first term. The contributions from low-order anharmonic corrections and electronic heat capacity are represented by the second term, a, and the high-order anharmonic lattice vibration is included by the third term, b. Depending on the shape of the heat capacity curve, the number ‘n’ can be 2, 3, or 4, and if necessary, another T^m term can also be added.

As different phases show varying behaviors connected with the high-order anharmonic vibration, other power series of temperature can also be used to fit the heat capacity data in the intermediate temperature regions [16,111]. The last term, c_p^{mag}, is also deduced from the magnetic transformation.

Finally, by integrating Eq. (3-7) with respect to the temperature, the Gibbs energy expression can be calculated as follows

$$G = E_0 + \frac{3}{2}R\theta_E + 3RTln\left[1 - \exp\left(-\frac{\theta_E}{T}\right)\right] - \frac{a}{2}T^2 - \frac{b}{n(n+1)}T^{n+1} - \int_0^T\left[\int_0^T \frac{c_p^{mag}}{T}dT\right]dT \qquad \textbf{(3-8)},$$

in which E_0 shows the cohesive energy (total energy without the vibrational contribution) at 0 K, the second term indicates the zero-point lattice vibration energy, which is described by the Einstein model here, and the last term is considered as the magnetic disordering effect contribution to the Gibbs energy, which is different for ferromagnetic and paramagnetic elements.

In CALPHAD, the Gibbs energy of a solid phase is normally constructed artificially to prevent the solid from being more stable than the liquid above the melting point. The coefficients in the heat capacity (c_p) expression ($a, b, \ldots$) should be determined by ensuring two conditions: the heat capacity and its first temperature derivative are continuous at the melting point, and the heat capacity of the solid at an arbitrary high temperature (e.g., 4000 K) matches that of the liquid [16]. The enthalpy and entropy of fusion are also used as fitting parameters for calculating Gibbs energy. These requirements ensure the continuity of heat capacity and its first derivative of the solid phase at the melting point [97].

In the case of solution phases or intermediate compounds, the heat capacity is frequently not known or is difficult to measure. In such cases, the Neumann-Kopp rule would be applied [90], in which the heat capacity is estimated as the weighted sum of the heat capacity of its components ($C_p^m = \sum_i x_i . C_{p,i}$).

4 Pd-Ni-S Novel Ternary Glass Forming System

This simple ternary system was studied experimentally by Karup-Moller et al. [19] for the first time in 1992. Two hundred and thirteen 100-mg charges were weighed out from pure Pd, Ni, and S elements, sealed in evacuated silica glass tubes, preheated to 573 K (300°C), and annealed at 673, 823, 998, and 1173 K (400, 550, 725, and 900 °C) for up to 15 days. Again, after regrinding the annealed samples, they were pelletized under a pressure of 4000 kg/cm^2, and were annealed for another 21 days, and were finally quenched. These quenched samples were further studied in polished sections by reflected light microscopy and electron microprobe analysis. Finally, based on these experimental phase studies, the isothermal ternary phase diagram of the Pd-Ni-S system at 673, 823, 998, and 1173 K (400, 550, 725, and 900 °C) was constructed. These isothermal ternary diagrams are shown in Figure 4-1. The 'hatched area' indicates the compositional range that is in a liquid state at the corresponding temperatures, suggesting that the entire system fully solidifies below 673 K (400°C).

The glass-forming ability of this system was recently studied by Kuball et al [18]. This system was an intriguing case study, as it shares similarities with the classic Pd-Ni-P glass-forming system. Sulfur, as the direct neighbor of phosphorus on the periodic table, has a comparable atomic diameter and electronegativity. This suggested that sulfur might behave similarly to phosphorus in the case of the glass-forming ability of this system. However, bulk glass-forming systems are typically highly sensitive to even minor compositional changes. Therefore, the successful one-to-one substitution of phosphorus by sulfur, while still maintaining glass formation, was rather unexpected.

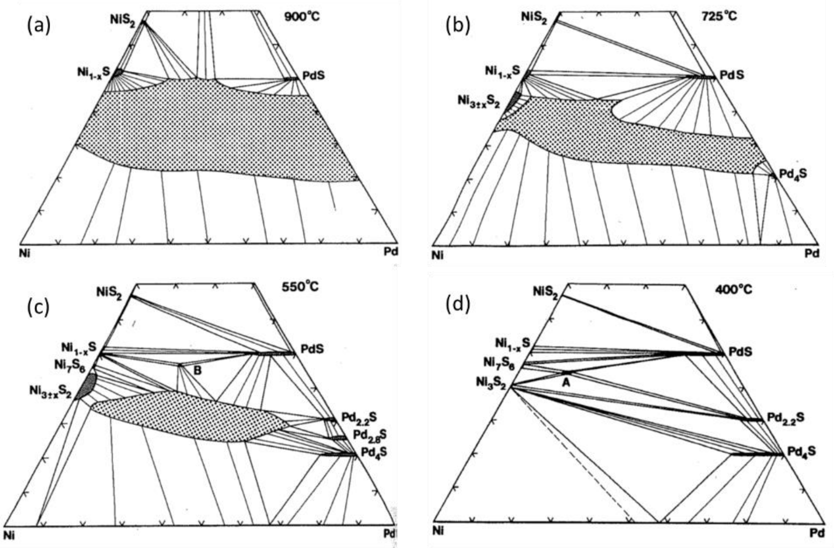

Figure 4-1. Isothermal Ternary Phase Diagram of Pd-Ni-S system at a) 1173 K (900°C), b) 998 K (725°C), c) 823 K (550°C), and d) 673 K (400 °C). The 'hatched area' indicates the liquid state of the particular composition range at the respective temperatures. Taken from [19].

From a technological perspective, the use of sulfur instead of phosphorus in glass-forming systems offers significant advantages. Sulfur exhibits a stable liquid phase under ambient pressure and lacks the toxic properties associated with phosphorus, simplifying the alloying process and improving overall processability [18].

Binary phase diagrams of Pd-S and Ni-S systems are shown in Figure 4-2. A eutectic reaction can be observed in the Pd-S diagram at 28 at. % sulfur (Figure 4-2(a)), and the Ni-S system at 33 at. % sulfur (Figure 4-2 (b)). These eutectic points are relatively deep in both systems; there is a difference of about 900 K between the melting point of pure Pd and the eutectic point in Pd-S and a difference of about 800 K between the melting point of pure Ni and the eutectic point in Ni-S. Interestingly, as can be seen in Figure 4-2 (c), the Pd-Ni binary system depicts an FCC (Pd-Ni) solid solution with a liquid-solid solution transformation happening at 1237° C (1510 K, 45.4%at Pd).

Since both sulfide systems, Pd-S and Ni-S, contain eutectic points; it is expected for the ternary Pd-Ni-S system to also show a eutectic reaction. As explained in section 2.1, deep eutectic points are correlated with high glass forming ability. Therefore, regarding deep eutectic points, it is expected that the glass forming region of the ternary Pd-Ni-S system is located within the boundaries of the liquid region depicted in Figure 4-1 (c). With this idea in mind, Kuball et al. [18] conducted a comprehensive study on this region to determine glass-forming compositions, and their approach proved to be successful.

According to Kuball et al. [18], as shown in Figure 4-3, the region where a BMG with a diameter of 1.6 mm can be produced is restricted to about 24–27 at.% S. In other metal-metalloid systems, the BMG-forming regions are found in different metalloid ranges; for example, around 20 at. % for Pd-Ni-P (10 mm rod) [112], and around 25 at. % for Pt-Ni-P [113]. As noted by Chen et al. [113], these metalloid content limits appear to be closely related to the locations of the binary eutectic points. Figure 4-3 also shows that the BMG-forming region is confined to palladium contents of 30 to 36.5 at. %, which is a much narrower range than that for Pd-Ni-P (25–50 at. %)[112].

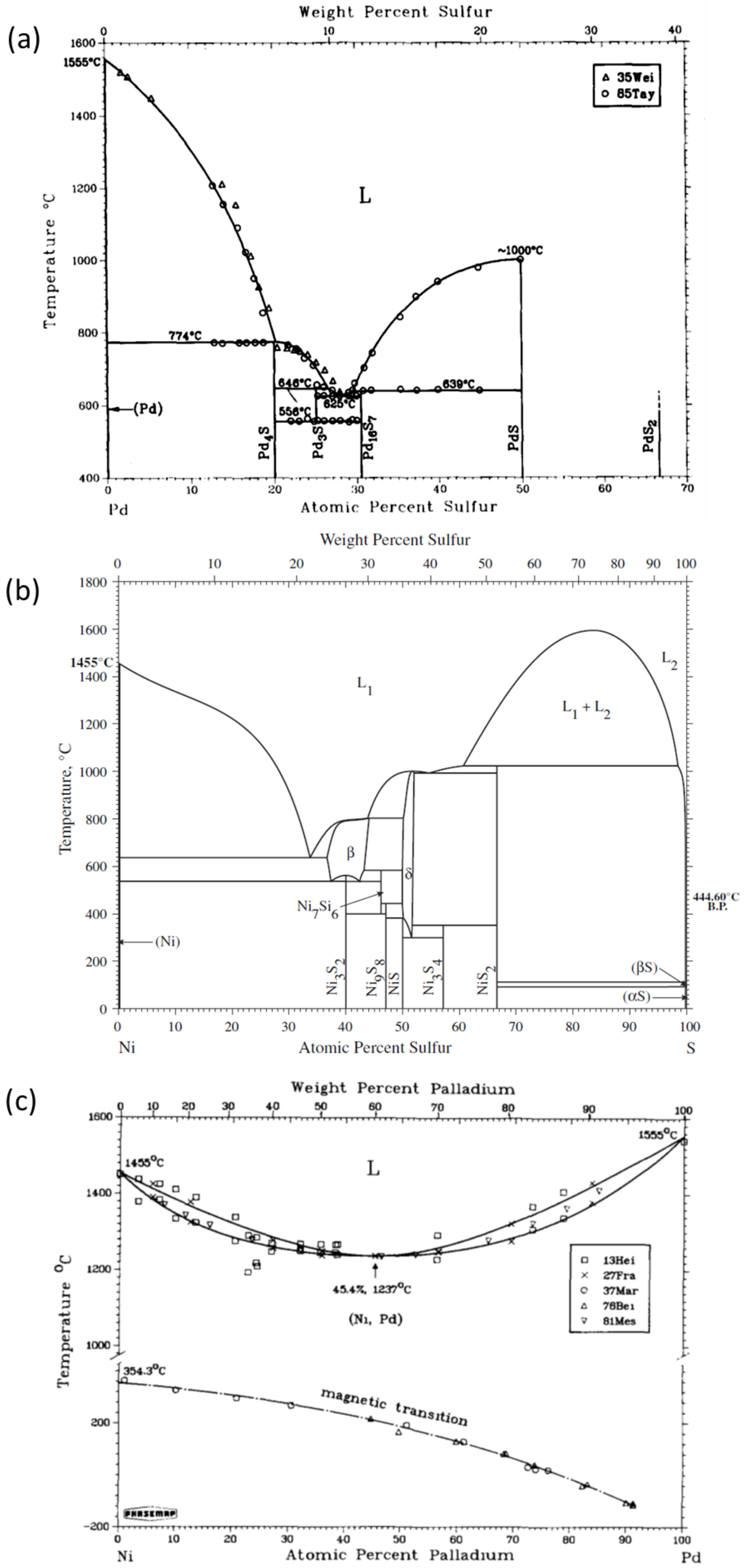

Figure 4-2. Binary Phase diagrams of a) Pd-S, b) Ni-S, and c) Pd-Ni. Taken from [114–116].

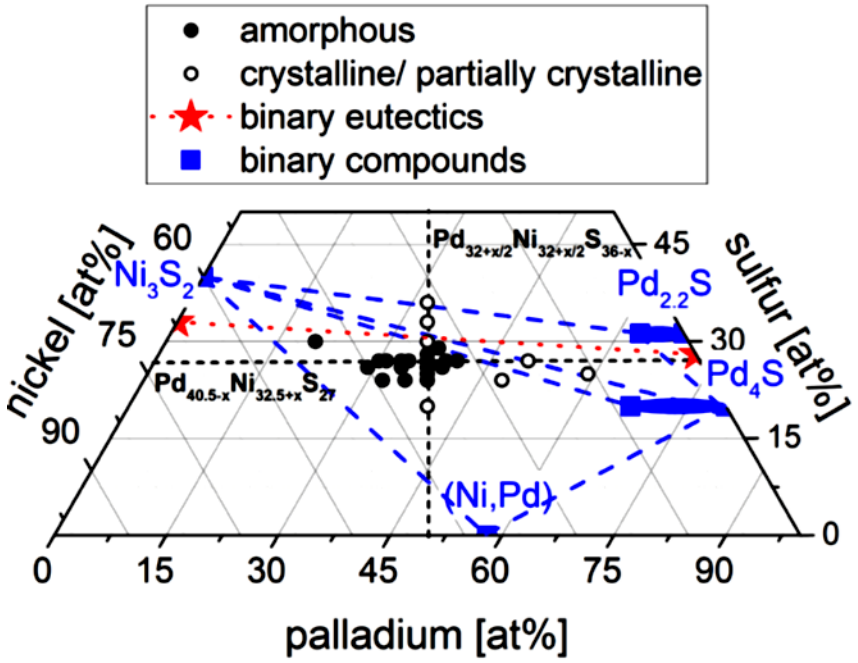

Figure 4-3. Glass forming region (GFR) in the ternary Pd-Ni-S system. Open circles indicate partially or fully crystalline samples, while filled circles denote fully amorphous samples with a thickness of at least 300 mm. The dashed blue lines represent the equilibrium phase fields at 673 K (400°C), as reported by Karup-Moller [19]. Taken from [42].

As seen in the equilibrium thermodynamic data of the ternary Pd-Ni-S system depicted in Figure 4-1, this system exhibits a relatively simple thermodynamic characteristic compared to other ternary systems. Furthermore, as shown in Figure 4-3, the only crystalline phases that compete with the glass-forming ability of this system are Pd_4S, Ni_3S_2, and the (Pd,Ni) solid solution. This observation has been also confirmed by high-energy synchrotron studies on these samples, which did not reveal the presence of any other metastable phases [18].

This simple thermodynamic landscape makes the Pd-Ni-S ternary system an attractive candidate for CALPHAD (Computer Coupling of Phase Diagrams and Thermochemistry) studies of glass-forming systems. In the work presented in this thesis, the authors have focused on the CALPHAD modeling of the ternary Pd-Ni-S system, with the aim of achieving a more realistic description of the (undercooled) liquid state in glass-forming compositions, which has been lacking for the ternary glass forming compositions by far, as discussed in Section 3.2.1.

The following chapters will present the acquired methodology for the experimental and modeling work, as well as the corresponding results and further discussions.

5 Experimental Methods

5.1 Sample Synthesis

Figure 5-1 shows the selected compositions of the Pd-Ni-S system that were studied in a ternary isothermal section of the phase diagram at 673 K. These compositions were selected to cover the whole glass-forming area as determined by Kuball et al. [18] to provide sufficient thermodynamic input data for the CALPHAD modeling. The Pd-S and Ni-S Pre-alloys were prepared by inductively melting the high-purity raw elements Pd (99.999 wt%), Ni (99.995 wt%) and S (99.9995 wt%) in silica quartz tubes under a high purity argon atmosphere (99.9999 wt%), as shown in Figure 5-2 for Ni-S. Subsequently, the pre-alloys were fluxed by remelting in dehydrated B_2O_3 to reduce the number of heterogeneous nucleation sites and enhance the glass-forming ability, as described in [70]. Boron oxide can be utilized as long as the elements within the metallic glass system have a lower affinity for oxygen than boron. This method was first introduced by Turnbull et al. in 1982 [55] and has become a standard practice in Pd-Ni-P alloys and various other metallic glass-forming systems.

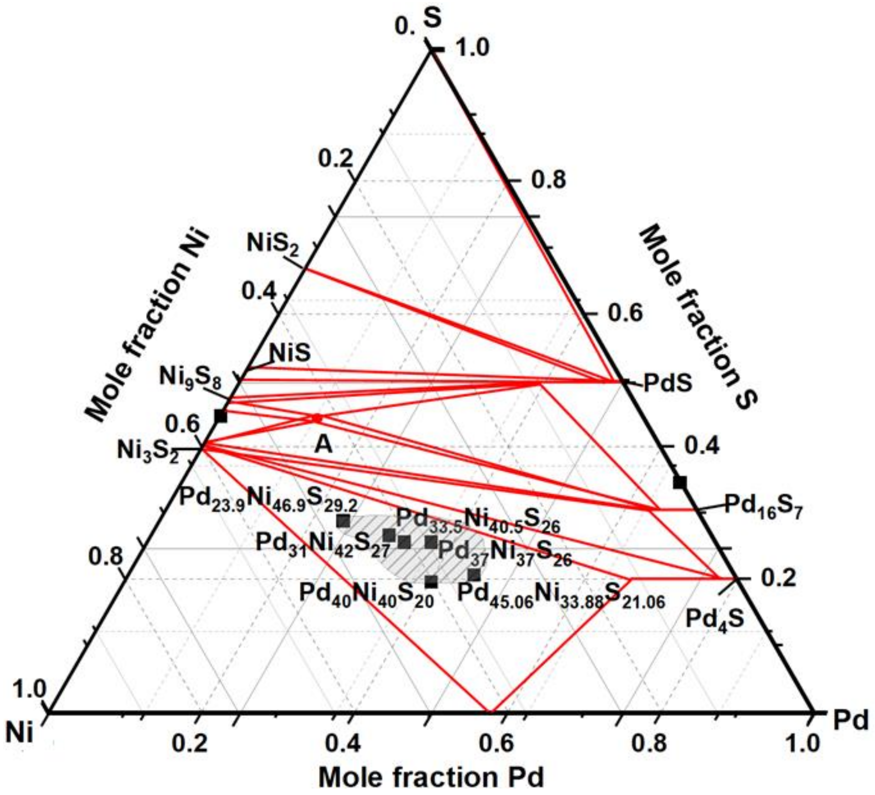

Figure 5-1. Position of the investigated Pd-Ni-S compositions in the ternary phase diagram, located within the shaded glass-forming region (GFR), according to [18].

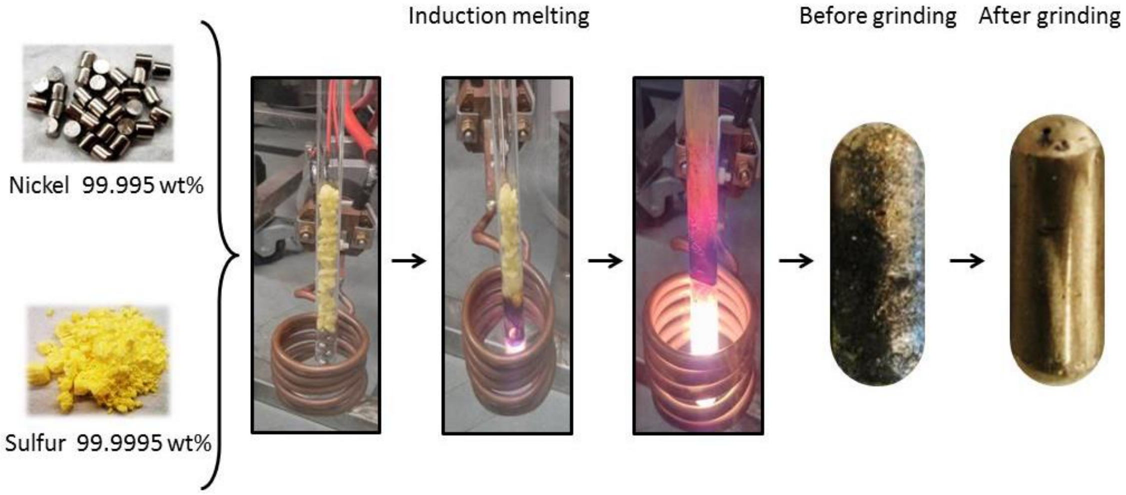

Figure 5-2. Synthesis procedure of nickel-sulfur (Ni-S) pre-alloy. On the left: Pure nickel and sulfur with their purities indicated. In the middle: Nickel and sulfur in a quartz tube undergoing induction melting. On the right: Ni-S binary alloy before and after grinding. Taken from [2].

Finally, as shown schematically in Figure 5-3, the purified pre-alloys were melted in an arc furnace together with the missing amounts of necessary elements to reach the final compositions. The master alloys of the compositions with marginal GFA were inductively re-melted and subsequently melt spun onto a rotating copper wheel to obtain thin ribbons of approximately 20-50 μm thickness. The melt spinning parameters were adjusted according to each alloy system's melting point and viscosity, and the amorphous state of every sample was evaluated via X-ray diffraction using a PANalytical X'Pert Pro diffractometer.

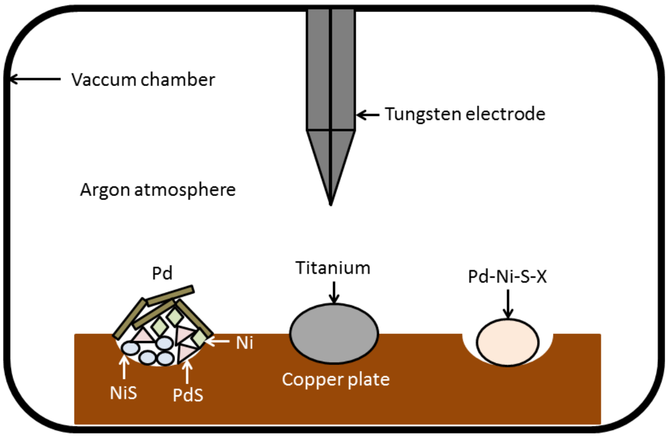

Figure 5-3. Schematic arrangement of the pre-alloys together with other elements (left) in the electric arc furnace, along with the final ingot (right) after melting, and the titanium getter for oxygen absorption (center). Taken from [2].

5.2 Calorimetry Measurements

Calorimetric measurements enable the determination of the heat exchange within a sample resulting from physical changes, reactions, or phase transitions. This data reveals melting and crystallization enthalpies, molar heat capacities, and details about the glass transition in amorphous samples.

In this work, different types of calorimetric measurement methods, including differential scanning calorimetry (DSC), differential thermal analysis (DTA), and fast differential scanning calorimetry (FDSC) are used. Here, the functional principle of these methods will be briefly discussed; a comprehensive overview of calorimetry can be found in [117,118].

5.2.1 Differential Scanning Calorimetry (DSC) and Differential Thermal Analysis (DTA)

In measurements using a DSC, the heat needed to change the temperature of a sample is measured in regard to a reference. In a power-compensated DSC, both of the sample and reference are subjected to the same temperature program in two identical small furnaces, while the heat flow is recorded as a function of time or temperature. This type of DSC operates on the "null principle," maintaining a zero-temperature difference between the sample and reference by adjusting the heating power of each furnace. Consequently, the heat flow $\dot{Q}$ is directly correlated to the difference in heating power ΔP, which is measured in milliwatts (mW). For an empty reference furnace, the heat flow $\dot{Q}$ can be expressed as

$$\Delta P \sim \dot{Q} = m\, c_p \frac{dT}{dt} \qquad \textbf{(5-1)},$$

in which m represents the mass of the sample, c_p is the specific heat capacity of the sample at constant pressure, and $\frac{dT}{dt}$ is the heating rate. In a power-compensated DSC, highly accurate heat flow measurements up to temperatures of about 1000 K can be carried out.

Just like DSC measurements, DTA measurements also allow the determination of the heat flow into a sample during a specific temperature program. In a DTA, the measurement head comprises a sample and a reference holder, both placed in a single furnace. These holders are connected to a thermocouple that measures the temperature difference between them as the sample and reference undergo the same thermal program. An exothermic (e.g., crystallization) or endothermic (e.g., melting) reaction results in a detectable temperature difference, ΔT_{SR}, between the sample and the reference. According to Newton's law of cooling, the heat flow, which is directly proportional to ΔT_{SR} , can be described as follows

$$\dot{Q}R = \Delta T_{SR} = mc_pR\frac{dT}{dt} \qquad \textbf{(5-2)},$$

in which m and c_p represent the mass, and the specific heat capacity of the sample, $\frac{dT}{dt}$ is the heating rate, and R is the thermal resistance which is dependent on both the experimental setup and the DTA instrument itself. Although DTA analysis is less accurate than DSC, it can be used up to very high temperatures of about 1900 K, making it suitable for melting studies.

5.2.1.1 Standard Scan

In this work, thermal analysis in the form of standard scans was carried out using a power-compensated Perkin Elmer DSC 8000 with a heating rate of 0.333 K/s (20 K/min) under a constant flow of 20 ml min^{-1} high-purity Argon atmosphere (99.9999 wt%). For every scanning rate and crucible combination, temperature and heat flow calibrations were done under the same constant flow of 20 ml min^{-1} high-purity Argon gas (99.9999%), using the melting transitions of In, Sn, Zn.

For low temperature measurements up to a maximum temperature of 723 K, Al-pans were used due to their better sensitivity. For examinations in higher temperature regions up to a maximum temperature of 973 K, graphite crucibles were utilized. Each sample was remeasured after crystallization, enabling us to use the signal of the crystallized sample to correct the baseline.

To study the melting events up to very high temperatures, a NETZSCH STA 449 Jupiter differential thermal analyzer (DTA) was used.

The used DTA in this work allows measurements up to 1873 K (1600 °C) with heating and cooling rates up to 0.833 K/s (50 K/min). Temperature and heat flow calibrations were carried out at a heating rate of 0.333 K/s (20 K/min), using the melting transitions of In, Sn, Zn, Al, Ag, Au, and Cu. Measurements were conducted using a heating rate of 0.333 K/s (20 K/min) under a constant purge gas flow of 50 ml/min high-purity Argon gas (99.9999%) and a protective gas flow of 20 ml/min Argon gas. For this high-temperature region, Al_2O_3 crucibles were used.

5.2.1.2 Molar Isobaric Specific Heat Capacity Measurement

Another important thermodynamic property of a system that can be measured by calorimetric methods, is the molar heat capacity. This property is very important in the case of calculating thermodynamic functions as discussed in section 2.3. Theoretically speaking, this parameter can be obtained using the Eq. (5-1). However, in practice, this relation is not directly applicable for measuring the exact heat capacity value of the system as a function of temperature, because of the additional heat flow term contributed by the measurement pans. The effect of the measurement pans can be omitted by measuring the heat capacity of the sample in regard to a sapphire standard using a step method [1,40]. In this method, which is visualized in Figure 5-4 (a), the sample is heated to a temperature T_1 using a constant heating rate of $q_h = 0.333\ K/s\ (20\ K/min)$ which corresponds to the shaded grey area in Figure 5-4 (b) of the recorded heat flow signal of a step method measurement, and then is held isothermally for a time of $\Delta t = 120\ s$ until the heat flow signal equilibrates. Afterward, the sample is heated up by 10 K to T_2 and is held again isothermally, to acquire a c_p value at a higher temperature. This stepwise heating and holding continues until the desired temperature range is achieved. Finally, the heat flow of a single temperature is obtained as follows

$$\dot{Q} = \dot{Q}_{q_h} - \dot{Q}_{iso} (= \dot{Q}_{\dot{T} \neq 0} - \dot{Q}_{\dot{T}=0}) \qquad \textbf{(5-3)},$$

in which $\dot{Q}_{q_h}$ is the heat flow right at the end of the heating interval, and $\dot{Q}_{iso}$ is the equilibrium heat flow during the isothermal holding interval as shown in Figure 5-4 (b). The procedure is repeated with an empty pan just like the pan used for sample measurement and a Sapphire standard. Eventually, the molar isobaric specific heat capacity can be calculated as follows

$$c_p(T)_{sample} = \frac{\dot{Q}_{sample} - \dot{Q}_{pan}}{\dot{Q}_{sapphire} - \dot{Q}_{pan}} \times \frac{m_{sapphire} \mu_{sample}}{m_{sample} \mu_{sapphire}} \times c_p(T)_{sapphire} \qquad \textbf{(5-4)},$$

in which m is the mass, μ is the molar mass, and $c_p(T)_{sapphire}$ is the known molar specific heat capacity of sapphire.

Hence, using the step method, the absolute value of the specific heat capacity in the glassy, crystalline, and supercooled liquid state for Pd-Ni-S alloy variations was determined in a power-compensated Perkin Elmer DSC8500 equipped with a three-stage intracooler which enables accurate low-temperature measurements. Specific molar heat capacity was measured for a temperature range from 223 K to 873 K, always using the same pans (Aluminum for low-temperature range, glassy and crystalline state, and graphite for high-temperature range, liquid state), while performing all four runs (empty pans, sapphire, amorphous sample, crystalline sample) on the same day to minimize any possible experimental errors.

For a better evaluation of the supercooled liquid region, one could vary the starting temperature of the applied heating program, while still keeping the 10 K temperature steps. This procedure helps obtain more data points of the specific heat capacity at a wider temperature range and improves the temperature resolution. However, due to the low thermal stability of the supercooled liquid in Pd-Ni-S variations, achieving data points in the supercooled liquid was challenging. The measurements were carried out for each temperature range once per heating and once per cooling and the average value for each temperature was considered for plotting and further analysis.

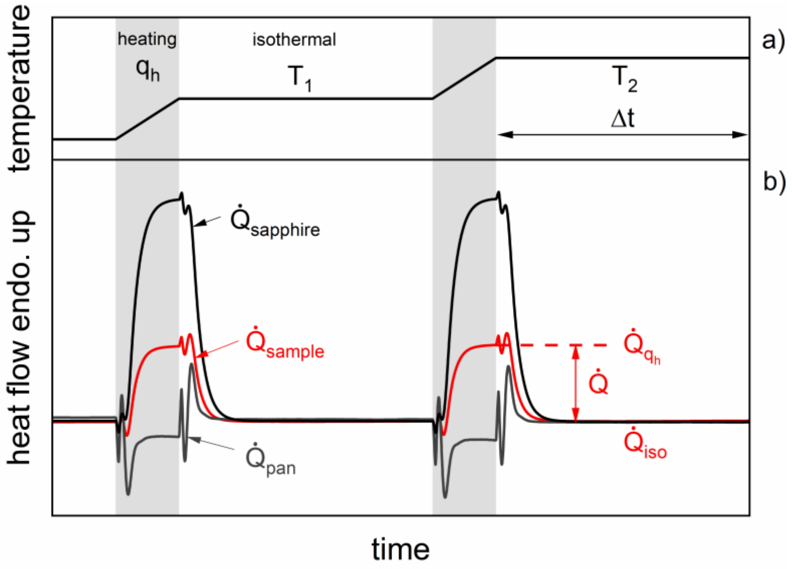

Figure 5-4. Schematic a) step-wise temperature profile and b) heat flow curves from a DSC specific heat capacity measurement using the step method. The shaded grey areas depict the heating interval while the white sections indicate the isothermal holding time (Δt). Red heat flow signals are from the sample, black from the sapphire and gray from the empty pan measurement. Taken from [119].

5.2.2 Fast Differential Scanning Calorimetry (FDSC)

Conventional DSC instruments have developed into a widely used standard method because of their great strength in obtaining complex information about physical transitions, the kinetics and enthalpies of chemical reactions, the structure of materials, and other transformations quickly and easily. Current modern conventional DSC instruments possess a signal time constant of about 1 s. Their applicable scanning rates lie between 0.1 and 300 K/min. However, these rates are not sufficient for the modeling of the technical production processes like casting due to the used high cooling rates. The metastable structures like metallic glasses which result from such processing techniques, can show diffusion or reorganization effects while using the typical low scanning rates during heating, leading to misinterpretation of the conventional DSC measurements. To address these limitations of conventional DSCs, dynamic calorimeters are needed to analyze relevant cooling rates, study reorganization during heating, and determine the kinetics of fast transformations [120–122]. The need to expand the applicable scanning rate range for dynamic calorimetry has led to the development of fast differential scanning calorimetry (FDSC) which enables a more detailed investigation of metastable materials [123].

The first fast differential scanning calorimetry, Flash DSC 1, was introduced in 2010 [124], which was designed for DSC measurements on organic materials, particularly polymers, at high heating and cooling rates of up to several thousand Kelvin per second. This device utilized the

UFS 1 sensor, capable of operating in a temperature range of –95 to 520 °C [125]. Despite its initial focus on organic materials, questions soon arose about its potential for studying inorganic materials, including metal alloys. Subsequently, applications involving relatively low melting alloys were published [126–129].

To extend the capabilities of FDSC 1, the Flash DSC 2+ was developed [130], allowing measurements at higher temperatures up to 1000 °C with the new UFH 1 sensor. This required a reduction in the active sensor area to achieve higher heating and cooling rates. Additionally, the new instrument was designed to measure samples under oxygen-free conditions, necessitating the development of new mechanical components, electronics, software, and modified sensor calibration procedures.

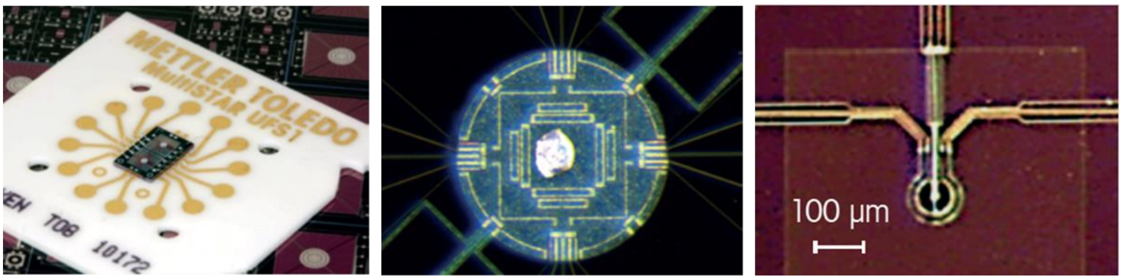

Figure 5-5. Flash DSC sensors, the left picture features a ceramic substrate with electrical connections and a membrane divided into two active zones (for sample and reference). The pictures in the middle and right show the membrane with a closer look at the active zones of the UFS 1 with a sample (middle) and the UFH 1 (right). Taken from [130].

Both types of sensors, UFS1 and UFH1, consist of a ceramic substrate with electrical connections and a membrane divided into two parts: one for the sample and one for the reference. The sensors are pin-compatible. The electronics of the Flash DSC 2+ were modified to be able to perform measurements with both sensors.

In Figure 5-5, both UFS1 and UFH1 sensors are shown. Each sensor consists of two thermally decoupled silicon nitride membranes with an active zone (a furnace) on each. The UFS1 sensor's active zone has a diameter of 500 µm, which incorporates resistance heaters and thermocouples for temperature measurement. Temperature homogeneity is the greatest in the quadratic area between the resistors, where the sample should be placed. A typical sample should have an area of about 150 µm by 150 µm or smaller, with its maximum thickness primarily depending on the sample's thermal conductivity. The UFH 1 sensor is similar to the UFS1, but it has a thinner membrane, and the temperature sensor is located at the center of the active zone, surrounded by two resistance heaters. Consequently, the sample placement area has a diameter of about 80 µm [130], requiring the samples to be in a good thermal contact with the sensor and sufficiently thin. Up to a temperature of about 800 °C, the characteristics of the sensor remain relatively stable. However, at higher temperatures, the thermal resistors can change over time, leading to baseline drift. Additionally, above 800 °C, the sensor's lifespan decreases with increasing temperature. In practice, we were also not able to heat above 800°C as the sensor broke quickly, technically limiting the use of the Flash DSC 2+ to the maximum temperature of 800°C.

The Flash DSC 2+ used in this work, produced by Mettler-Toledo and equipped with a MultiSTAR UFH 1 high-temperature chip sensor, is shown in Figure 5-6. An attached Huber HC100 intracooler allows reaching cooling rates of up to 40,000 K/s. While the measuring process is running, the system is continuously purged using a high-purity argon (99.9999%) gas flow of 60 ml/min to hinder oxidation effects on the metallic samples.

Due to the small active sensor area, a precise sample preparation is required. As mentioned in section 5.1, thin ribbons with a thickness of about 20 μm are prepared in the melt-spinning device. Small pieces of these ribbons are cut and subsequently placed under a stereomicroscope and then small samples are cut off with the help of a micro-scalpel. The samples are afterward positioned onto the active area of the chip sensor using hairs with very fine ends.

A good thermal contact between the sample and sensor is necessary for successful Flash DSC measurements. The pre-melting of the sample on the surface of the sensor is currently the method which is most frequently used to improve thermal contact. In this regard, the small metallic sample is heated up and cooled down subsequently several times using moderate heating and cooling rates ($50\ K/s$), until the output signal is stable enough to ensure the best possible thermal contact for further measurements.

After the pre-melting procedure of the sample onto the chip-sensor and establishing a good thermal contact, an estimation of the sample mass can be provided using the enthalpy of fusion measured by conventional DSC, ΔH_m^{DSC}, for a known mass as a reference value using the following equation [131,132]

$$m_{FDSC} = \frac{\Delta H_m^{FDSC}}{\Delta H_m^{DSC}} \times m_{DSC} \qquad \textbf{(5-5)}.$$

Figure 5-6. Flash DSC2+ produced by Mettler-Toledo. Taken from [130].

The sample mass was optimized subsequently to prevent sample size effects on thermal stability, such as the dependence of critical cooling and heating rates on sample mass [131,133].

After measuring the sample, a calibration material such as indium or aluminum can be placed on the sensor (e.g. on the reference side). The measured onset temperature of the melting peak can be used subsequently to correct the sample temperature in the evaluation process. Additionally, the eutectic temperature determined in the conventional DSC for the same sample could be also used to correct the temperature offset of the FDSC sensors [134].

The applied measuring programs are explained in the next sections. More information on the Flash DSC, possible applications, and practical information can be found in reference [135].

5.2.2.1 Critical Cooling Rate Measurements (CCR)

Critical cooling rate experiments are done in the first step to determine the minimum required cooling rate (R_c) to bypass crystallization. CCR measurements were only carried out for better glass forming compositions, namely $Pd_{31}Ni_{42}S_{27}$, $Pd_{33.5}Ni_{40.5}S_{26}$, and $Pd_{37}Ni_{37}S_{26}$, following the methodology described in [132] as shown in Figure 5-7, applying Various cooling rates between 1 and 32768 K/s. The rest of compositions could not reach the glassy state even with the very high cooling rates applicable by FDSC.

First, the sample is heated up to an equilibration temperature well above the liquidus temperature of the respective alloy and held isothermally for homogenization of the liquid. Since the liquidus temperatures of the Pd-Ni-S alloy variations are well below the maximum possible temperature for the UFH 1 chip-sensor (800°C), sufficient overheating is feasible. However, due to the volatile nature of sulfur, samples couldn’t be held at very high temperatures for a long time, otherwise, the composition would have changed, and the sample could no longer be used. To avoid crystallization, it is crucial to subject the material to a degree of overheating and holding time well above the liquidus temperature [136,137]. This process dissolves heterogeneities or atomic clusters remaining from crystals [138–140]. These nuclei, if not dissolved, act as heterogeneous nucleation sites, negatively impacting the GFA of the liquid, demanding a higher critical cooling rate, and finally affecting the shape of the Time-Temperature-Transformation (TTT) diagram [137]. Other possibilities like liquid to liquid transition (LLT) below or above T_l by the formation of ordered atomic clusters in metallic melts [141–143] or liquid to liquid separation (LLS) at temperatures above T_l [144,145] could also affect the homogeneity of the melt. In [140], Q. Cheng et.al proved experimentally via fast scanning calorimetry that the homogenization temperature of a prototyped Au-based metallic melt is 192 K above its liquidus temperature. For this reason, we tried overheating up to 200 K above the liquidus temperature and holding times ranging from 0.1 s to 10 s to achieve the best result. However, there was a minimal discrepancy in the outcomes obtained at various annealing temperatures, signifying the uncomplicated nature of the melt and implying a lack of substantial overheating requirement.

In the next step, the fully equilibrated liquid is rapidly cooled to the target temperature, below the glass transition temperature T_g, and then is reheated to the equilibration temperature at a controlled heating rate. The utilized cooling rates range from 1 K/s up to 32768 K/s in a logarithmic scale to provide a reasonable scaling in the plot. For the Pd-Ni-S alloy variations, heating is performed at 100 K/s, because this rate has shown the most stable measurement signal. Those steps are then repeated for the various indicated cooling rates. Finally, for each cooling step the crystallization enthalpy, ΔH_x , is determined from the subsequent heating step. The resulting enthalpies are normalized to the maximum attained enthalpy to identify the critical cooling rate, which is the first cooling rate that fails to re-attain a fully amorphous sample, indicated by less than 100% crystallization enthalpy ΔH_x.

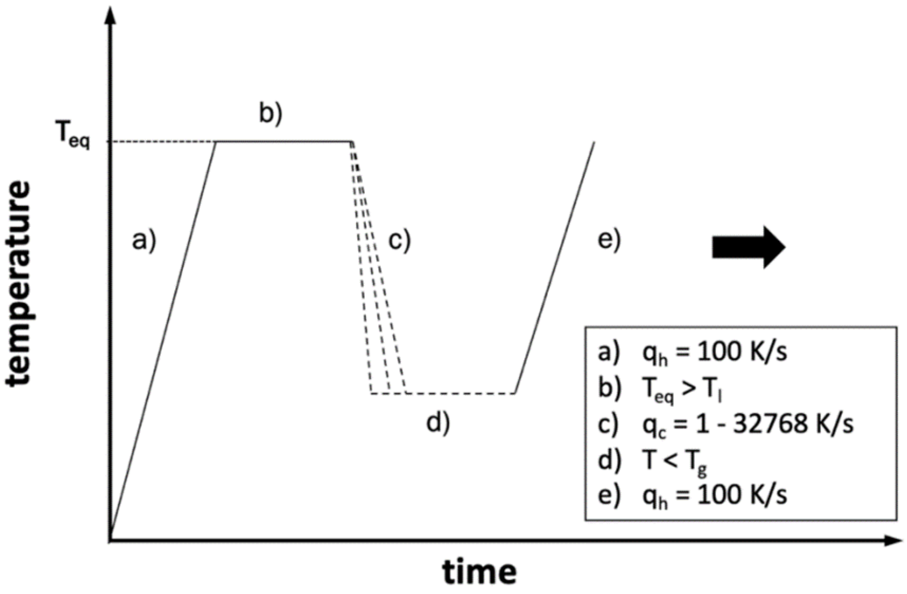

Figure 5-7. Critical cooling rate measurements temperature program. a) and b) Overheating the sample to the equilibrium liquid state and holding it, ensuring the homogenization of the liquid. c) Quenching the liquid with varying cooling rates. d) Short equilibration at temperatures far below the glass transition. e) Further heating scan to determine the crystalline percentage in the sample.

5.2.2.2 Isothermal Time- Temperature-Transformation (TTT) Diagram Measurements

In-situ examination of crystallization behavior can be conducted using Fast Differential Scanning Calorimetry (FDSC) through isothermal measurements, enabling the recording of Time-Temperature-Transformation (TTT) diagrams for the transformation kinetics of an undercooled metallic melt into the crystalline state. Via very fast cooling rates provided by FDSC, comprehensive examination of TTT diagrams, especially at the nose region, has become achievable for various Bulk Metallic Glasses [133,146,147].

The thermal protocol of the samples shown in Figure 5-8 consisted of heating above the liquidus temperature at 773 K, and 823 K with a holding time of 1 and 10 s to see the effect of different parameters on the final TTT diagram, followed by quenching at a rate of 40000 K s^{-1} to the desired isothermal temperature. In the case of measured compositions, the change in annealing temperatures and holding times does not affect the crystallization times significantly, however, longer holding times lead to a faster deterioration of the sample due to the sulfur evaporation. Each isotherm was measured at least three times to provide enough statistics. Especially at high temperatures above the nose and the minimum crystallization time, due to the nucleation-controlled crystallization, more statistics are needed. At this high-temperature range, the crystalline growth rate has its maximum and in the case of the formation of a supercritical nucleus, the sample would experience a rapid and short crystallization in a large timescale, resulting in a large scatter of crystallization times at high temperatures [3]. As shown in Figure 5-9, by integrating the area underneath the exothermal crystallization event in each isothermal measurement, the times at which 1%, 50%, and 99% of the heat release occurred, are determined and are used for the construction of the TTT diagram.

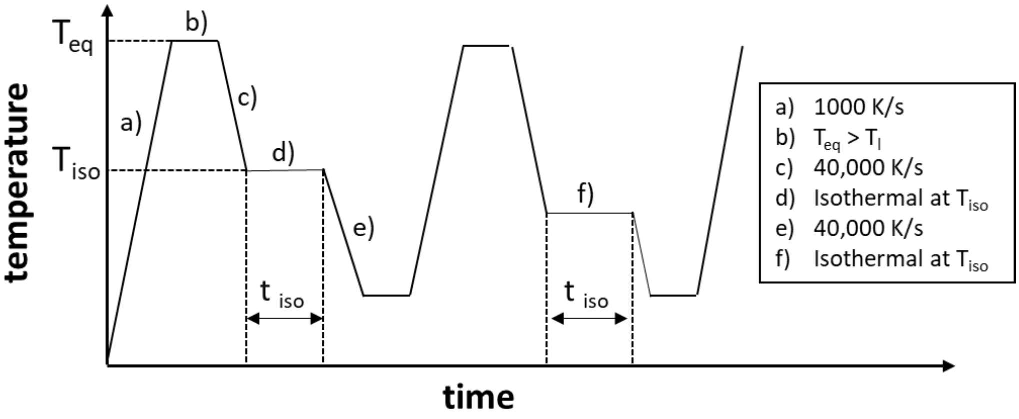

Figure 5-8. Time-Temperature-Transformation (TTT) diagram measurements program upon cooling. a) and b) Overheating the sample to the equilibrium liquid state and holding it, ensuring the homogenization of the liquid. c) Rapid cooling of the sample with a constant cooling rate faster than the critical cooling rate. d) Isothermal holding at the target temperature for a sufficient time for full crystallization of the sample. e) Quenching of the sample and reheating to the equilibrium liquid temperature.

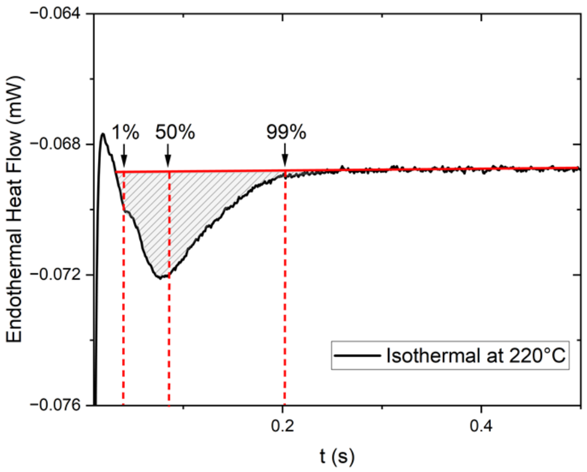

Figure 5-9. Exothermal crystallization event in an isothermal measurement at 220°C, the times at which 1%, 50%, and 99% of the heat release occurred, are determined based on the enthalpy of crystallization and are used for the construction of the TTT diagram.

5.2.2.3 Step - Response Analysis Method

Step response analysis during cooling with a base frequency of 10 Hz was used to assess the atomic mobility [148,149] . By quenching the sample to a temperature well below the glass transition temperature (T_g) and applying further temperature down jumps of 2 K followed by isothermal holding times of 0.1024 s, the complex frequency dependent specific heat capacity $c_p^*(\omega)$ is calculated through Fourier transformation of the heat flow rate and the instantaneous cooling rate as follows

$$c_p^*(\omega) = \frac{\int_0^{t_p} HF(t)e^{-i\omega t dt}}{\int_0^{t_p} q_c(t)e^{-i\omega t dt}} \qquad \textbf{(5-6)}.$$

By changing the duration of the period, t_p, and accessing higher harmonics, a frequency range from 1 to 180 Hz could be accessed and finally, the frequency-dependent dynamic glass transition temperature, $T_{g,dyn}$, and the temperature dependent relaxation time, $\tau_\alpha = 1/\omega$, are obtained.

In the case of Pd-Ni-S variations, the step response analysis could be only carried out on better glass forming compositions, $Pd_{31}Ni_{42}S_{27}$, $Pd_{33.5}Ni_{40.5}S_{26}$, and $Pd_{37}Ni_{37}S_{26}$. Figure 5-10 shows the recorded heat flow response of $Pd_{37}Ni_{37}S_{26}$ during the step response analysis carried out in cooling. The sample is cooled with 30000 K/s to bypass the crystallization and further temperature down jumps of 2 K with a cooling rate of 2000 K/s followed by isothermal holding time of 0.1024 s are applied. These temperature down-jumps of 2 K are small enough to ensure the linearity of the response, since the thermal fluctuations of the glass forming systems are known to be larger than 2 K [149,150], enabling us to assess the atomic dynamics associated with the glass transition, most importantly α-relaxation [148,149,151]. The glass transition happens approximately in the range of 190 °C to 160 °C. In the case of better glass forming systems like $Pt_{57.3}Cu_{14.6}Ni_{5.3}P_{22.8}$ [152] more data before glass transition could be collected and a wider frequency range could be investigated.

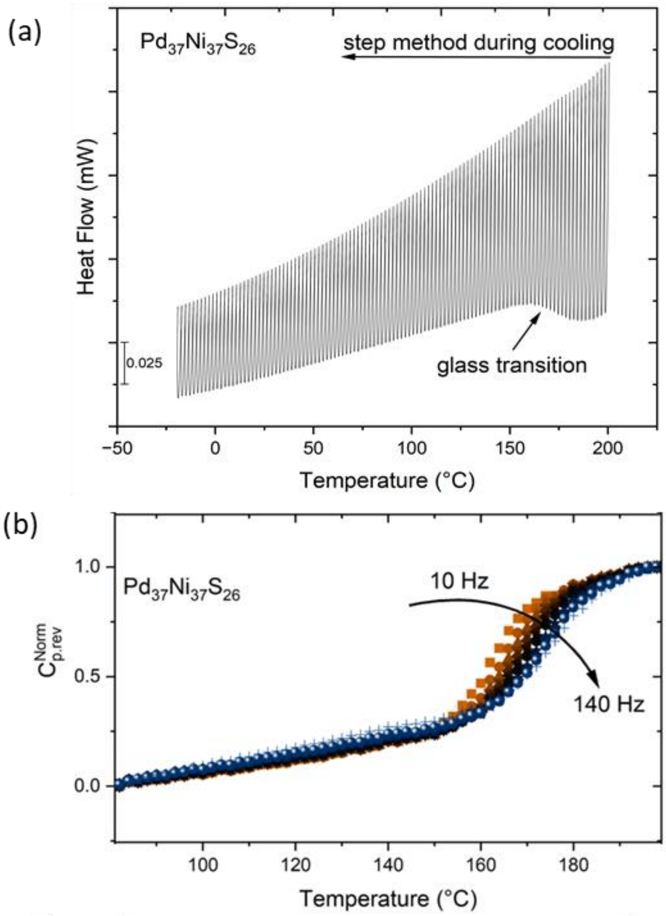

Figure 5-10. a) Recorded heat flow signal of $Pd_{37}Ni_{37}S_{26}$ measured using step response method in cooling. The sample is cooled fast to bypass the crystallization and further temperature down jumps of 2 K followed by isothermal holding of 0.1024 s are applied. The glass transition happens almost from 190 °C to 160 °C. In the case of better glass forming systems like $Pt_{57.3}Cu_{14.6}Ni_{5.3}P_{22.8}$ more data before glass transition could be collected and a wider frequency range could be investigated [152], b) Reversing specific heat as a function of temperature and frequency obtained from step response analysis at 10 Hz by FDSC for $Pd_{37}Ni_{37}S_{26}$.

5.3 High-energy Synchrotron X-ray Diffraction

The formation of the primary phase in the alloys upon undercooling was studied using wide-angle X-ray scattering (WAXS) experiments carried out at the Deutsches Elektronen-Synchrotron (DESY) in Hamburg, Germany. Samples with various compositions were heated to a fully molten state and then cooled down with an average cooling rate of about 200 K/s. All experiments were carried out under aerodynamic levitation (ADL) conditions to minimize the impact of heterogenous nucleation [153]. In this technique, samples do not get in contact with any container material. As a result, aerodynamic levitation facilitates high-temperature experiments without the issues related to the chemical interaction between sample and container walls, such as the corrosion of oxide crucibles by silicate melts [154,155], which also prevents the heterogeneous nucleation caused by contact with the container wall.

This method is better suited to Pd-Ni-S compositions in comparison to electrostatic levitation (ESL), due to their high vapor pressure. In the case of electrostatic levitation, the sample is processed under high vacuum conditions, and the levitation relies on the condition that the sample has (static) charges on its surface [156–160]. Typically, when the sample (material) starts to evaporate, this also brings away charges on the surface. Therefore, ESL usually does not work with materials which have high vapor pressures, apart from the drawback that evaporation will also change the sample composition at some point. In the case of PdNiS or PdNiP compositions, it has not been exactly determined what was evaporating, but it is supposed that it is sulfur or phosphorus.

The utilized aerodynamic levitation facility provided by the Institute of Materials Physics in Space at the German Aerospace Center is shown in Figure 5-11. A close-up view of the levitation chamber with a water-cooled levitation stage at the bottom with a converging-diverging nozzle mounted on top of it is also shown in Figure 5-12. The nozzle is fixed by a screw-bracket, and a test sample is mounted into the levitation nozzle.

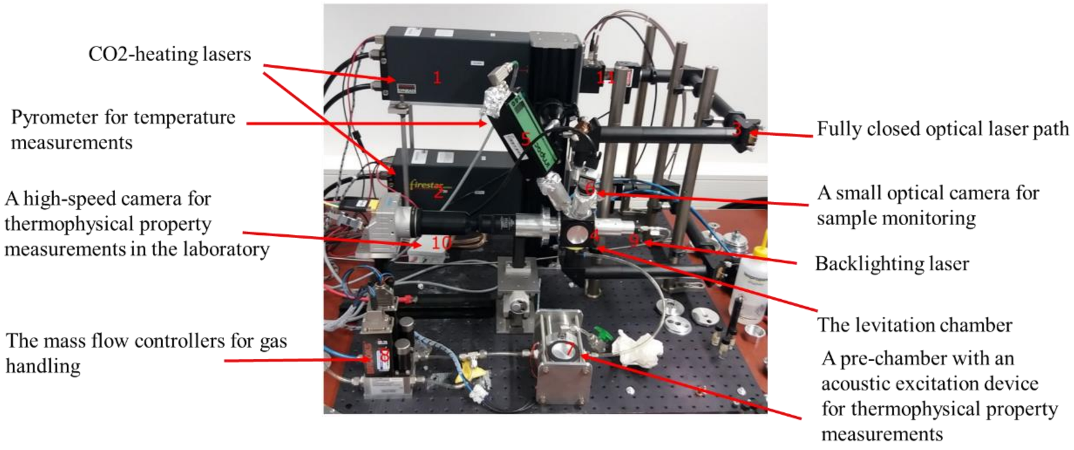

Figure 5-11. Aerodynamic levitation facility with its different components.

The general working principle of ADL is to freely suspend droplets of oxide or metallic materials such as alloys, glasses, or slag using a gas jet directed through a converging-diverging nozzle [161]. The freely suspended droplet is heated through invisible laser radiation in the micrometer range to temperatures above its liquidus. Diagnostics are applied to measure e. g. thermophysical properties of the molten droplet over wide and sometimes extreme temperature ranges [162]. Besides thermophysical properties also phase selection upon solidification can be studied by coupling the ADL facility with synchrotron X-ray diffraction. Furthermore, the microscopic structure of the liquid droplet can be studied by coupling the ADL facility with synchrotron X-ray or neutron diffraction [163,164]. In the past, the facility was operated at ESRF for synchrotron X-ray diffraction experiments in a single beamtime [165].

In this work, the samples were investigated in transmission mode at the high-intensity beamline facility P21.1 at PETRAIII. A schematic illustration of the in-situ synchrotron X-ray experiments set up is shown in Figure 5-13. The practical size limit for levitating droplets is *ca*. 2–4 mm in diameter [161]. Hence, samples of Pd-Ni-S alloy variations with a diameter of ~2 mm were made and used for this study. A wavelength of 0.12215 Å was used and the intensity was detected with a Perkin Elmer XRD1621 CsI bonded amorphous silicon detector (2048 pixels x 2048 pixels). The two-dimensional X-ray diffraction patterns of the samples were subsequently integrated to obtain the scattering intensity I(Q) using the software package PyFAI (Python Fast Azimuthal Integration) [166]. Finally, the obtained data were compared with the simulated diffraction data of the equilibrium phases using the Vesta software [167]. For more information on the theoretical backgrounds of the scattering experiments and further analysis of the data, the reader is referred to Ref. [78,119] respectively.

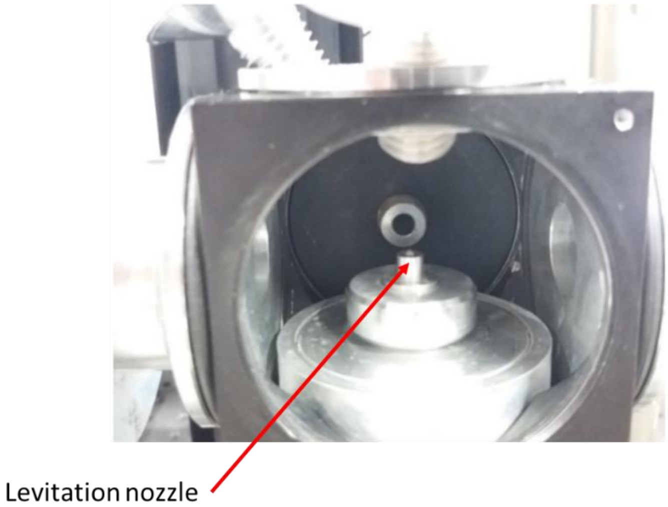

Figure 5-12. Close-up view of the levitation chamber. Water-cooled levitation stage at the bottom with a converging-diverging nozzle mounted on top of it. The nozzle is fixed by a screw-bracket. A test sample is mounted into the levitation nozzle.

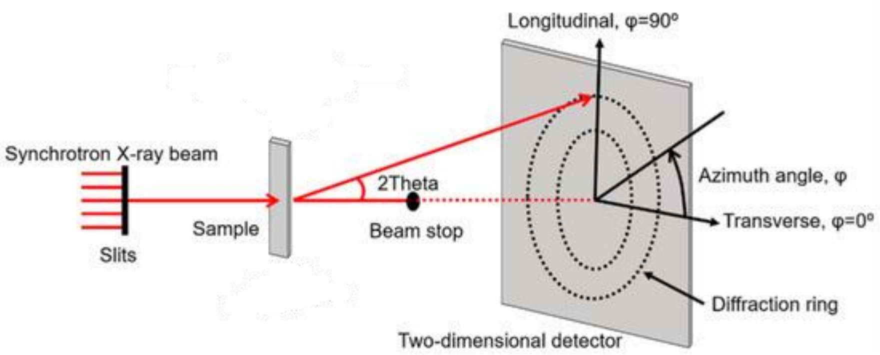

Figure 5-13. Schematic illustration of the in-situ synchrotron X-ray experiments set up. Taken from [168].

5.4 CALPHAD Modeling

The CALPHAD modeling was carried out by our project partners at Karlsruhe Institute of Technology, and full credit for the methodology and results is attributed to their work. What follows is a summary tailored to complement the experimental approach. Further details on the CALPHAD work will be available in the forthcoming publications.

5.4.1 Modelling of pure Sulfur, Palladium, Nickel, Ni-S, Pd-S, and Ni-Pd binary systems

Pure sulfur and Palladium have been modeled using the third-generation CALPHAD database framework. The thermophysical properties of orthorhombic sulfur (α-S), monoclinic sulfur (β-S), and liquid sulfur have been thoroughly summarized [169,170] and are evaluated for the CALPHAD modeling. The description of pure Nickel is taken from the previous assessment of Hao et al [171].

For the modeling of Ni-S, Pd-S, and Ni-Pd binary systems, available thermodynamic and thermophysical data of the system in the literature [114–116] have been critically assessed and incorporated into the Gibbs free energy description of the solid phases, within the context of the third-generation CALPHAD database.

5.4.2 Modelling of the Pd-Ni-S ternary system

5.4.2.1 Modelling of the crystalline phases

The experimental study conducted by Karup-Moller and Makovicky was utilized for evaluating the Pd-Ni-S system, as it provides comprehensive phase diagram data for isothermal sections at 673 K, 823 K, 998 K, and 1173 K [19]. In their research, the authors identified two intermetallic compounds in the system: $Ni_{9.54}Pd_{7.48}S_{15}$ [172], and $Ni_{3.77}Pd_{1.20}S_4$. These compounds were experimentally synthesized and characterized in this work. The measured specific heat capacity of these two intermetallic compounds was subsequently used in the modeling process. The newly developed models for the Pd-Ni, Ni-S, and Pd-S binary systems were integrated into the description of the Pd-Ni-S ternary system.

5.4.2.2 Modelling of the ternary undercooled liquid and the glassy state

The third-generation database approach utilizes the two-state liquid model to describe a unary system's “liquid-amorphous “ state [100], allowing for a single segment to represent the entire liquid-amorphous state from 0 K to the above melting temperature. However, modifications are necessary for glass-forming ternary systems to accurately describe the undercooled liquid, as more complex interatomic interactions significantly influence its properties. A common observation is a drastic increase in the specific heat capacity of the undercooled liquid, ${c_p}^l$, as the temperature decreases (see Figure 6-3), which can be modeled using the Kubaschewski equation, Eq. (6-2) [173]. Such behavior is associated with the decrease of the configurational entropy in the undercooled liquid and is attributed to the development of strong SRO and/or MRO. This excess heat capacity for the glass-forming system cannot be fully described by the current set of parameters of the two-state model, necessitating the addition of an extra "Kubaschewski" term $-0.5bT^{-1}$ to the ternary interaction parameter in the Gibbs free energy description.

The increase in the heat capacity of the undercooled liquid with decreasing temperature ceases at the glass transition, T_g, where a sudden drop in the heat capacity is observed. As represented in Table 6-1, all investigated samples show a T_g of 433 ± 10 K at a heating rate of 20 K/min. Consequently, the modeled T_g of the system is set in a simplified manner at 433 K. The glass transition is formally described by introducing a second segment for the glassy (non-equilibrium) state from 0 K to T_g.

The modeling should adhere to the following criteria:

(1) The enthalpy and entropy values of the glassy state at T_g must match those of the undercooled liquid state;

(2) The calculated Kauzmann temperature must be lower than the experimentally determined T_g;

(3) The specific heat capacity of the glassy state is considered similar to the corresponding mixture of the crystalline phases, which can be approximated by the Kopp-Neumann rule [90]. This assumption is valid, as demonstrated by the previous analysis conducted by Kuball et al. [18], which shows that for the $Pd_{31}Ni_{42}S_{27}$ glass-forming alloy, as well as in our own research (Figure 3) and other studies [41,42], the specific heat capacity (c_p) of the glass matches that of the crystal up to temperatures just below the glass transition region.

Lack of data for the undercooled liquid is another challenge for this analysis, as the behavior of the undercooled liquid cannot be easily predicted. Fir this reason in this work, we incorporate experimental data across various compositions to serve as input for fitting the heat capacity, enthalpy of formation, and enthalpy of fusion. Additionally, the acquired cp data within the supercooled liquid region of $Pd_{31}Ni_{42}S_{27}$ [18], known for being the more thermally stable composition, are also used to improve the model. This promises a self-consistent dataset that can adequately describe the thermodynamic behaviors of the Pd-Ni-S system in the glass-forming range.

6 Results

6.1 Thermodynamic Studies

6.1.1 Experimental thermal and thermodynamic data

In the first step, important thermal and thermodynamic data of the different Pd-Ni-S alloys were investigated. This includes the determination of the glass transition temperature (T_g); crystallization temperature (T_x); enthalpy of crystallization ($\Delta \mathrm{H_x}$); eutectic temperature (T_{eu}); liquidus temperature (T_l) and enthalpy of fusion ($\Delta \mathrm{H_m}$) upon standard scan and also specific heat capacity functions c_p (T) of crystalline mixtures, glasses, undercooled liquids and melts. These properties are important in terms of further thermodynamic and kinetic analysis and serve as important input data for CALPHAD modeling. In particular, experimental heat capacity data of the melt and undercooled liquid are used for the proper modeling of the liquid phase in the CALPHAD approach and the enthalpies of crystallization and fusion serve as input data for this modeling of the liquid.

Figure 6-1 (a-b) shows the up scans acquired for different compositions during heating with 20 K/min through DSC and DTA (blue and red curves, respectively). The onset temperatures of the glass transition, T_g, crystallization, T_x, eutectic $T_{eu,}$ and liquidus temperatures T_l were determined using a tangent construction. The crystallization enthalpy, $\Delta \mathrm{H_x}$, and the heat of fusion, $\Delta \mathrm{H_m}$, were determined by integrating the area between the curve and the baseline. All the evaluated data are listed in Table 6-1. The heat flow profile of Pd-Ni-S variations in Figure 6-1 (a) displays a weak endothermic jump that corresponds to the glass transition due to the difference in heat capacity of glass and supercooled liquid. Additionally, these alloys exhibit exothermic events associated with the crystallization process. Regarding other compositions, $Pd_{37}Ni_{37}S_{26}$ predominantly crystallizes via a single distinct peak, suggesting its proximity to the actual eutectic point within this ternary system. Additionally, Kuball et al. [18], in their alloy development framework, demonstrated that this alloy exhibits the narrowest melting interval $(T_l - T_m)$ in comparison to many other developed compositions, signifying its proximity to the eutectic point. These compositions also exhibit a notably limited supercooled liquid region $(T_x \ - T_g)$ as can be seen in Figure 6-1 (a) and from the determined ΔT $(T_x \ - T_g)$ values presented in Table 6-1, indicating their poor thermal stability. Consequently, further measurements within the supercooled liquid, such as $\mathrm{c_p}$ (heat capacity) measurements and relaxation studies, become problematic. From Table 6-1 can be seen that, changing Pd content towards alloys with larger Pd content, results in a slight decrease in the enthalpy and entropy of fusion.

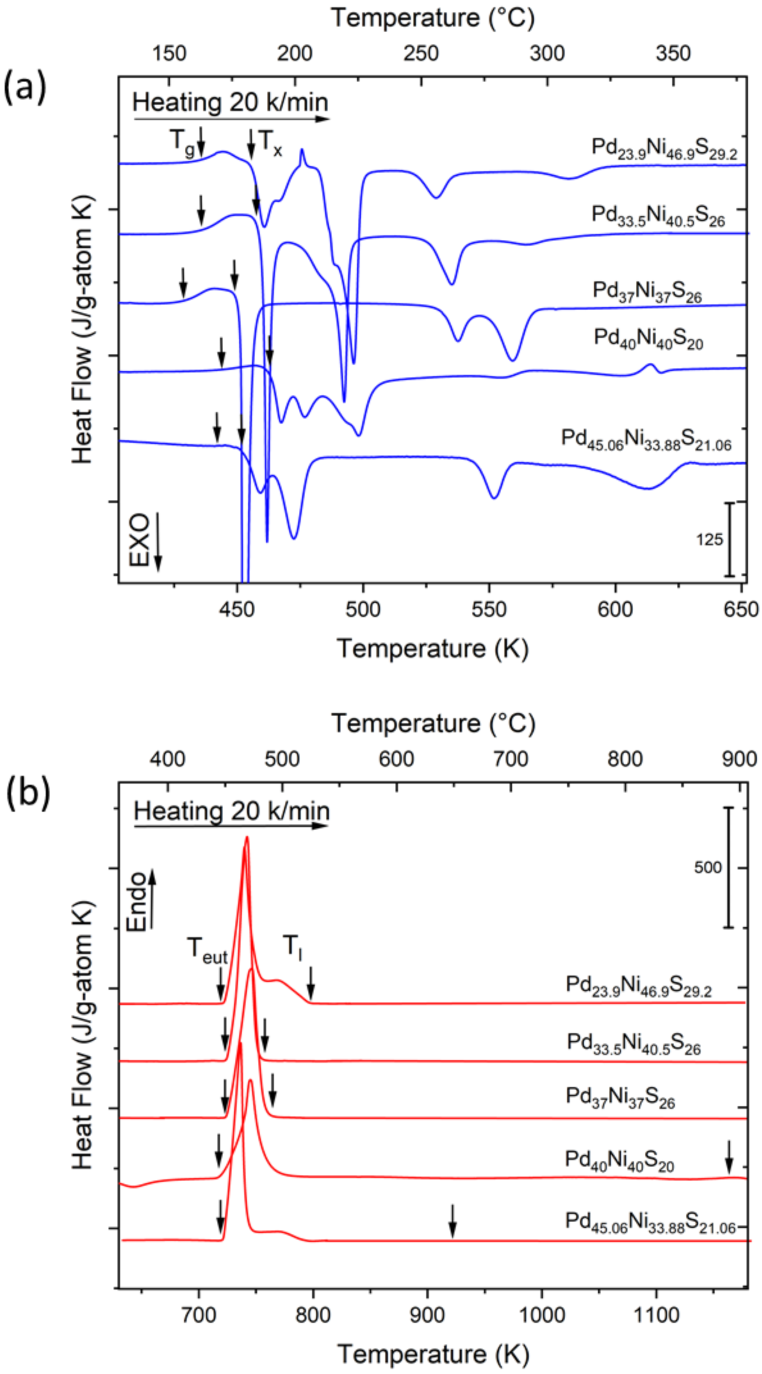

Figure 6-1. Heat flow curves resulted from, a-b) DSC (blue curve) and DTA (red curve) scans of Pd-Ni-S variations acquired during heating with 20 K/min, the glass transition temperature (T_g), crystallization temperatures (T_x), eutectic temperatures (T_{eu}) and liquidus temperatures (T_l) are indicated with black arrows.

Table 6-1. Measured thermodynamic characteristic temperatures and enthalpies for Pd-Ni-S variations: glass transition temperature ($\boldsymbol{T_g}$), crystallization onset temperature ($\boldsymbol{T_x}$), eutectic temperature ($\boldsymbol{T_{eu}}$) and liquidus temperature ($\boldsymbol{T_l}$), enthalpy of crystallization ($\Delta\mathbf{H_x}$), enthalpy of fusion ($\Delta\mathbf{H_m}$), and entropy of fusion ($\Delta\boldsymbol{S_m} = \Delta\mathbf{H_m}/\boldsymbol{T_l}$). Measurements are conducted with a heating rate of 20K/min.

Composition	T_g (K)	T_x (K)	ΔT (T_x-T_g) (K)	ΔH_x (kJ/g-atom)	T_{eu} (K)	T_l (K)	ΔH_m (kJ/g-atom)	ΔS_m ($\Delta H_m/T_l$) (J/g-atom K)
$Pd_{23.9}Ni_{46.9}S_{29.2}$	434	456	22	-5.428	723	791	12.076±0.203	15.26
$Pd_{33.5}Ni_{40.5}S_{26}$	434	459	25	-5.553	729	750	11.025±0.147	14.7
$Pd_{37}Ni_{37}S_{26}$	426	451	25	-4.894	726	757	10.726±0.162	14.17
$Pd_{40}Ni_{40}S_{20}$	441	462	21	-3.867	721	1173	10.131±0.450	8.64
$Pd_{45.06}Ni_{33.88}S_{21.06}$	438	452	14	-4.616	721	923	10.392±0.339	11.26

Focusing on Figure 6-1 (b), changes in the eutectic and liquidus temperature and the shape of the melting peaks can be monitored as well. In the case of $Pd_{40}Ni_{40}S_{20}$ and $Pd_{45.06}Ni_{33.88}S_{21.06}$, determining the liquidus temperature from the main apparent melting peak is misleading and as observed in synchrotron measurements during heating, the (Pd, Ni) solid solution is stable up to very high temperatures and the liquidus temperature could be only roughly estimated based on the measured in-situ HEXRD patterns upon heating with 20 K/min and the temperatures associated with them as shown in Figure 6-2 (a-b). As could be seen, in both cases, the (Pd, Ni) solid solution is stable up to higher temperatures and melts away at about 1173 K and 923 K in $Pd_{40}Ni_{40}S_{20}$, and $Pd_{45.06}Ni_{33.88}S_{21.06}$ respectively. Due to the geometry of the measured samples (2 mm balls) and their limited glass-forming ability, they were in the crystalline state before the heating procedure. Also, during cooling experiments, (Pd, Ni) solid solution tends to form as the first phase around the same temperature region (see Figure 6-8 (d, e)).

Referring back to Figure 6-1 (b), as expected, the determined eutectic temperatures of all the Pd-Ni-S alloy variations are in the same range, specifying a eutectic temperature of $724 \pm 3\ K$. In respect to the shape of the melting peaks, $Pd_{23.9}Ni_{46.9}S_{29.2}$, $Pd_{45.06}Ni_{33.88}S_{21.06}$, and $Pd_{40}Ni_{40}S_{20}$ show a shoulder respectively on their right and left side, indicating their off-eutectic behavior, while $Pd_{33.5}Ni_{40.5}S_{26}$ and $Pd_{37}Ni_{37}S_{26}$ are melting through one single peak, showing their proximity to the eutectic point as discussed earlier.

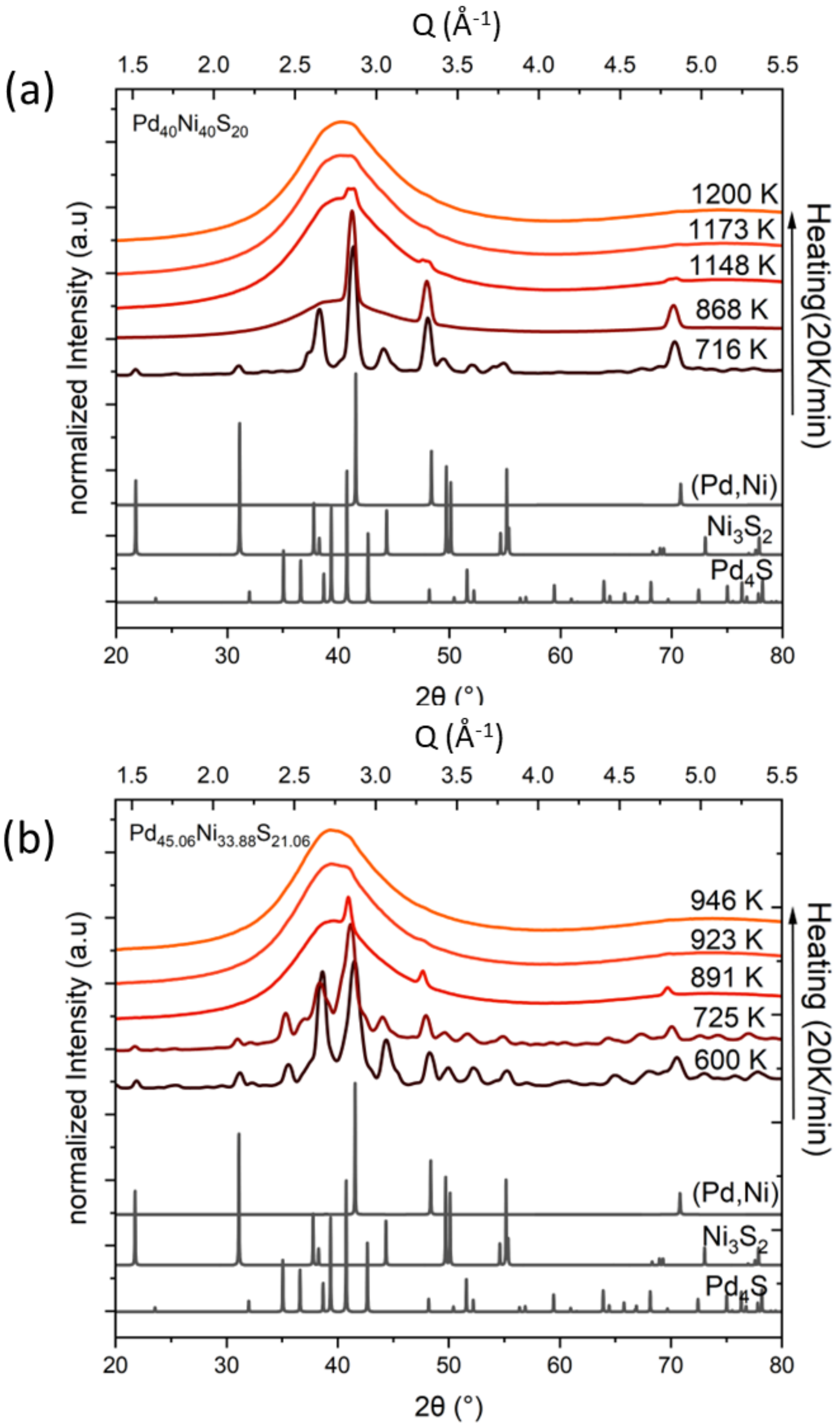

Figure 6-2. In-situ high energy synchrotron X-ray diffraction pattern of a) $Pd_{40}Ni_{40}S_{20}$, b) $Pd_{45.06}Ni_{33.88}S_{21.06}$ upon heating from the crystalline state at 20 K/min. In addition, the simulated diffraction patterns of the possible crystalline phases are shown. In both cases, the (Pd, Ni) solid solution is stable up to higher temperatures and melts away at about 1173 K and 923 K respectively.

6.1.2 Isobaric specific heat capacity data

The measured specific heat capacities for the glassy, crystalline, and liquid states using the step method [40,51] for Pd-Ni-S alloy variations are shown in Figure 6-3. Heat capacity data of the alloy $Pd_{31}Ni_{42}S_{27}$ was previously published in Ref. [42] and is used in further analysis. The model of Inaba [174] can be used to represent the variation of heat capacity with temperature of glassy and crystalline phases around the Debye temperature (T_D) as

$$c_p^{g/x} = 3R/M\{1 - \exp(-1.5\,T/T_D)\} \qquad \textbf{(6-1)}.$$

M and T_D are fitting constants, R is the universal gas constant and T is the absolute temperature. At temperatures far above the T_D, the temperature dependencies of liquid and crystal specific heat capacity, $c_p^l(T)$ and $c_p^x(T)$, were fitted using the Kubaschewski equations [173]

$$c_p^l = 3R + aT + bT^{-2} \qquad \textbf{(6-2)},$$

and

$$c_p^x = 3R + ct + dT^2 \qquad \textbf{(6-3)},$$

where R is the universal gas constant and a, b, c, and d are fitting parameters listed in Table 6-2. To evaluate the accuracy of the obtained specific heat capacity functions, the area between the specific heat capacity curves of the liquid and crystalline phase is estimated for the interval between the onset temperature of crystallization (T_x) and liquidus temperature (T_l). This value should be equal to the difference between the enthalpy of fusion and the enthalpy of crystallization, which is described as

$$\Delta H_m - \Delta H_x = \int_{T_x}^{T_l} \Delta c_p^{l-x}\, dT \qquad \textbf{(6-4)}.$$

Considering $Pd_{37}Ni_{37}S_{26}$ as an example in Figure 6-3, the integral of the shaded area yields a value of 5.7 kJ g-atom^{-1} and $\Delta H_m - \Delta H_x$ equals to 5.8 kJ g-atom^{-1}, representing a difference of less than 2%, which validates the reliability of the c_p measurements. This relation holds valid for all the other compositions as well.

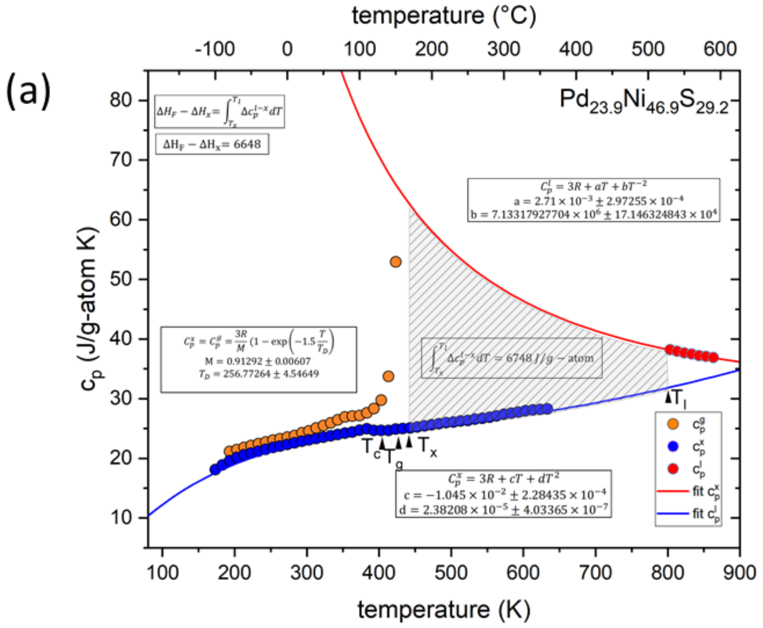
(a)
temperature (°C)
-100
0
100
200
300
400
500
600
$Pd_{23.9}Ni_{46.9}S_{29.2}$
$\Delta H_F - \Delta H_x = \int_{T_x}^{T_l} \Delta c_p^{l-x} dT$
$\Delta H_F - \Delta H_x = 6648$
$C_p^l = 3R + aT + bT^{-2}$
$a = 2.71 \times 10^{-3} \pm 2.97255 \times 10^{-4}$
$b = 7.13317927704 \times 10^6 \pm 17.146324843 \times 10^4$
$C_p^x = C_p^g = \frac{3R}{M}\left(1 - \exp\left(-1.5\frac{T}{T_D}\right)\right)$
$M = 0.91292 \pm 0.00607$
$T_D = 256.77264 \pm 4.54649$
$\int_{T_x}^{T_l} \Delta c_p^{l-x} dT = 6748\ J/g-atom$
T_l
T_c
T_g
T_x
$C_p^x = 3R + cT + dT^2$
$c = -1.045 \times 10^{-2} \pm 2.28435 \times 10^{-4}$
$d = 2.38208 \times 10^{-5} \pm 4.03365 \times 10^{-7}$
c_p^g
c_p^x
c_p^l
fit c_p^x
fit c_p^l
c_p (J/g-atom K)
80
70
60
50
40
30
20
10
100
200
300
400
500
600
700
800
900
temperature (K)

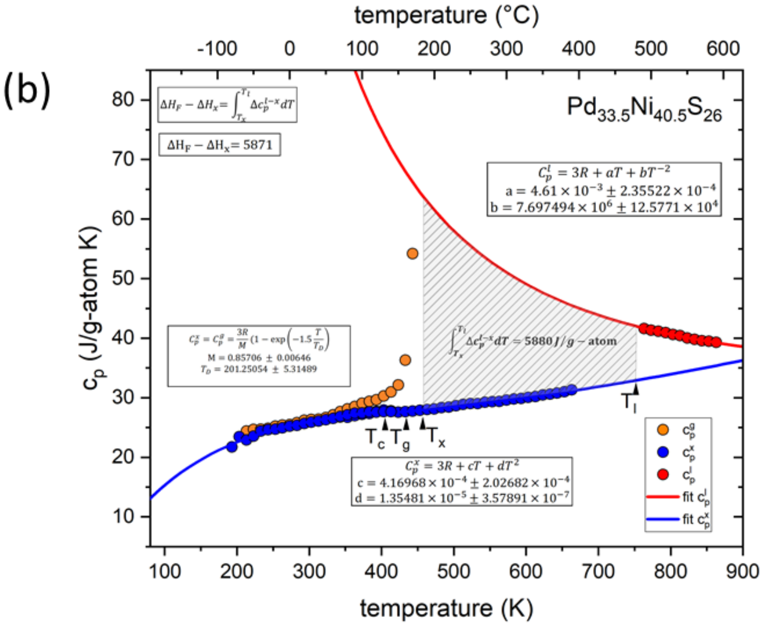
(b)
temperature (°C)
-100
0
100
200
300
400
500
600
$Pd_{33.5}Ni_{40.5}S_{26}$
$\Delta H_F - \Delta H_x = \int_{T_x}^{T_l} \Delta c_p^{l-x} dT$
$\Delta H_F - \Delta H_x = 5871$
$C_p^l = 3R + aT + bT^{-2}$
$a = 4.61 \times 10^{-3} \pm 2.35522 \times 10^{-4}$
$b = 7.697494 \times 10^6 \pm 12.5771 \times 10^4$
$C_p^x = C_p^g = \frac{3R}{M}\left(1 - \exp\left(-1.5\frac{T}{T_D}\right)\right)$
$M = 0.85706 \pm 0.00646$
$T_D = 201.25054 \pm 5.31489$
$\int_{T_x}^{T_l} \Delta c_p^{l-x} dT = 5880\ J/g-atom$
T_l
T_c
T_g
T_x
$C_p^x = 3R + cT + dT^2$
$c = 4.16968 \times 10^{-4} \pm 2.02682 \times 10^{-4}$
$d = 1.35481 \times 10^{-5} \pm 3.57891 \times 10^{-7}$
c_p^g
c_p^x
c_p^l
fit c_p^l
fit c_p^x
c_p (J/g-atom K)
80
70
60
50
40
30
20
10
100
200
300
400
500
600
700
800
900
temperature (K)

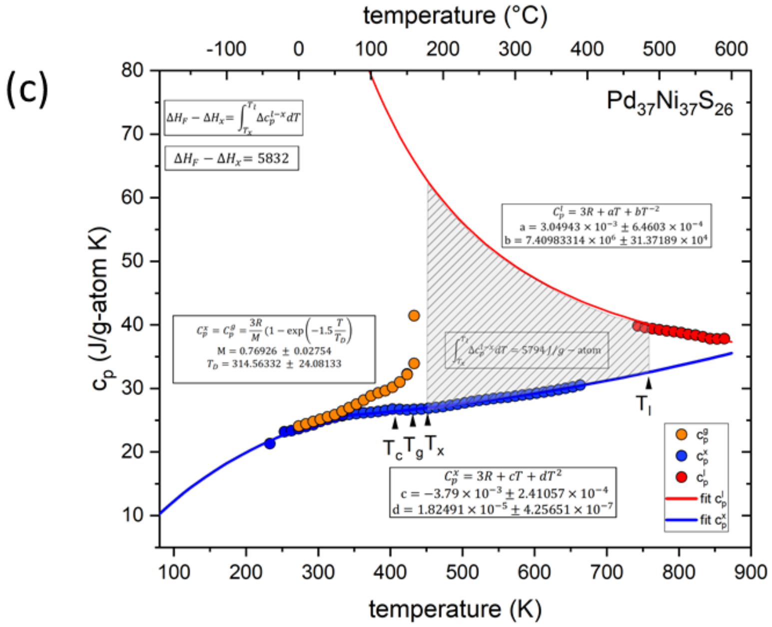
(c)
temperature (°C)
-100
0
100
200
300
400
500
600
$Pd_{37}Ni_{37}S_{26}$
$\Delta H_F - \Delta H_x = \int_{T_x}^{T_l} \Delta c_p^{l-x} dT$
$\Delta H_F - \Delta H_x = 5832$
$C_p^l = 3R + aT + bT^{-2}$
$a = 3.04943 \times 10^{-3} \pm 6.4603 \times 10^{-4}$
$b = 7.40983314 \times 10^6 \pm 31.37189 \times 10^4$
$C_p^x = C_p^g = \frac{3R}{M}\left(1 - \exp\left(-1.5\frac{T}{T_D}\right)\right)$
$M = 0.76926 \pm 0.02754$
$T_D = 314.56332 \pm 24.08133$
$\int_{T_x}^{T_l} \Delta c_p^{l-x} dT = 5794\ J/g-atom$
T_l
T_c
T_g
T_x
$C_p^x = 3R + cT + dT^2$
$c = -3.79 \times 10^{-3} \pm 2.41057 \times 10^{-4}$
$d = 1.82491 \times 10^{-5} \pm 4.25651 \times 10^{-7}$
c_p^g
c_p^x
c_p^l
fit c_p^l
fit c_p^x
c_p (J/g-atom K)
80
70
60
50
40
30
20
10
100
200
300
400
500
600
700
800
900
temperature (K)

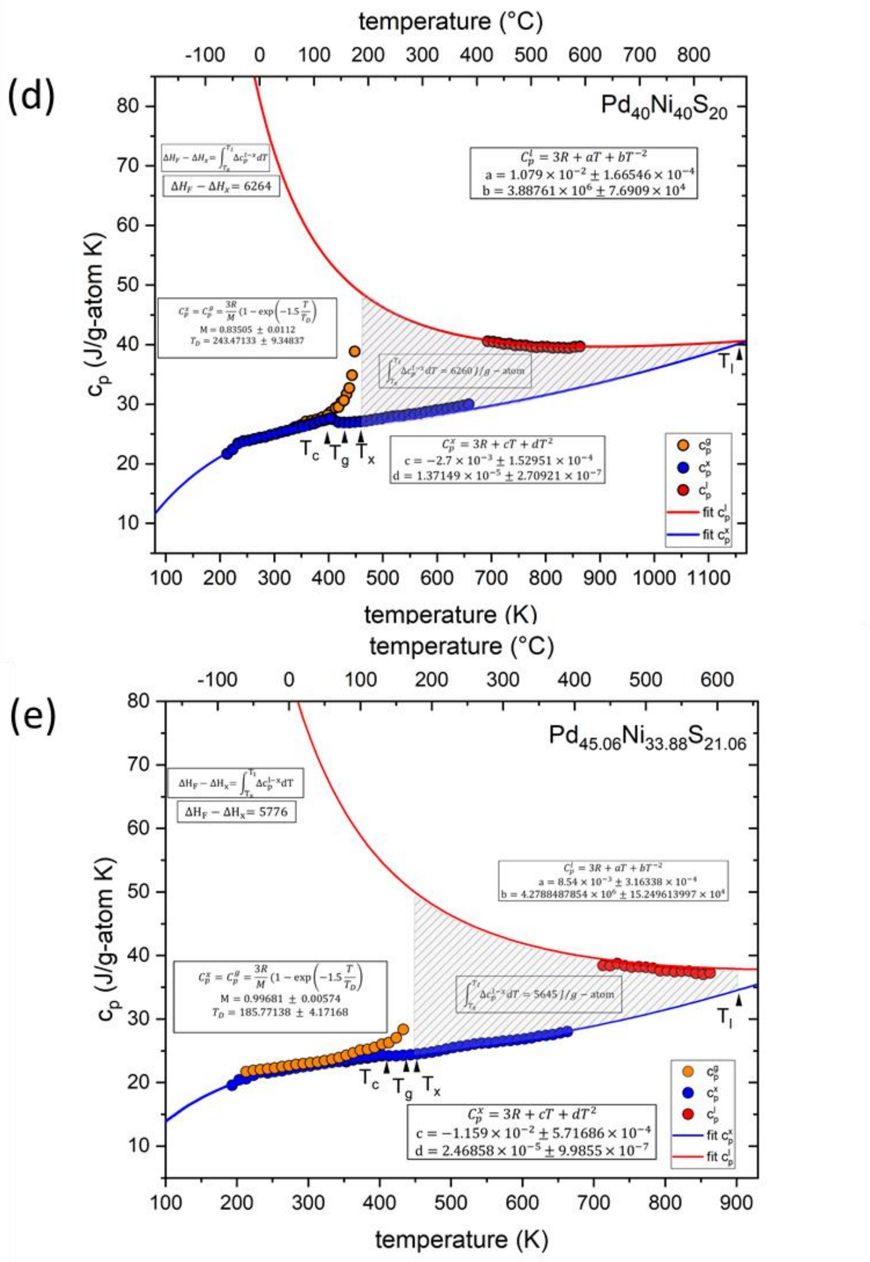

Figure 6-3. Isobaric specific heat capacity data of glassy c_p (orange circles), liquid (red circles), and crystalline state (blue circles) for Pd-Ni-S variations. The fits of crystalline states (blue full line) and liquid states (red full line) are based on the Inaba and Kubaschewski equations, Eq. (6-1), (6-2), and (6-3).

At temperatures lower than the glass transition but above the Debye temperature, both the glassy and crystalline alloy exhibit similar specific heat capacities, approximately around 3 R (≈25 J g-atom $^{-1}$ K $^{-1}$), which is in line with the rule of Dulong-Petits [40,175–177]. At approximately 350 K, the c_p of the glass starts to deviate from that of the crystal because of relaxation effects and finally after the glass transition range, it is expected to reach the c_p of the supercooled liquid. However, due to the poor thermal stability of the supercooled liquid and the interference of crystallization, despite attempts to measure c_p data in different temperature intervals, no c_p data in the supercooled liquid could be collected.

Table 6-2. Fitting parameters derived from applying Eq. (6-1) and (6-2) and (6-3) to the specific heat capacity data.

Fitting Parameter / alloy	**$Pd_{23.9}Ni_{46.9}S_{29.2}$**	**$Pd_{33.5}Ni_{40.5}S_{26}$**	**$Pd_{37}Ni_{37}S_{26}$**	**$Pd_{40}Ni_{40}S_{20}$**	**$Pd_{45.06}Ni_{33.88}S_{21.06}$**
$\mathbf{a.10^3\ (J\ g-atom^{-1}K^{-2})}$	2.71 ± 0.2973	4.61 ± 0.2355	3.0494 ± 0.6460	$10.79 \times \pm 0.1665$	8.54 ± 0.3163
$\mathbf{b.10^{-6}\ (J\ K\ g-atom^{-1})}$	7.1332 ± 0.1715	7.6974 ± 1.2577	7.4098 ± 0.3137	3.8876 ± 0.0769	4.2788 ± 0.1524
$\mathbf{c.10^3\ (J\ g-atom^{-1}K^{-2})}$	-10.45 ± 0.2284	0.4169 ± 0.2026	-3.79 ± 0.2410	-2.7 ± 0.1529	-11.59 ± 0.5716
$\mathbf{d.10^6\ (J\ g-atom^{-1}K^{-3})}$	23.8208 ± 0.4033	13.5481 ± 0.3578	18.2491 ± 0.4256	13.7149 ± 0.2709	24.6858 ± 0.9985
$\mathbf{M.10^2}$	91.29 ± 0.607	85.706 ± 0.646	76.926 ± 2.754	83.50 ± 1.12	99.681 ± 0.574
$\mathbf{T_D(K)}$	256.7726 ± 4.5464	201.2505 ± 5.3148	314.5633 ± 24.0813	243.4713 ± 9.3483	185.7713 ± 4.1716

6.1.3 Excess Enthalpy, Entropy and Gibbs free energy

From the measured specific heat capacity data and the DSC scan data for the liquidus temperature T_l, heat of fusion ΔH_m and entropy of fusion ΔS_m, the enthalpy and entropy difference between the (undercooled) liquid and the crystalline mixture $\Delta H^{l-x}(T), \Delta S^{l-x}(T)$ can be calculated using Eq. (2-2), (2-3) and (2-4) in section 2.3. For the calculations, the liquidus temperature is considered as the temperature, at which the liquid and crystalline state are in equilibrium and the Gibbs free energy of the crystal and liquid are considered equal. In the real nucleation process, a driving force exists as soon as the melt is cooled below the T_l. This driving force is the chemical potential difference between the liquid and crystalline nucleus. In our simplistic approach, the Gibbs free energy difference between the supercooled liquid and the crystalline mixture is assumed to be equal to the chemical potential. In the case of very off-eutectic systems, like $Pd_{40}Ni_{40}S_{20}$ and $Pd_{45.06}Ni_{33.88}S_{21.06}$ which show a high-temperature shoulder during melting, it may lead to underestimations of the excess enthalpy, entropy, and Gibbs free energy. However, it is reasonable to consider the liquidus temperature T_l as a reference point where $\mathbf{\Delta G^{l-x}}$ is considered to be zero, as there is a driving force for crystallization in multi-component systems just below this temperature.

The calculated thermodynamic excess functions for Pd-Ni-S alloy variations are plotted in Figure 6-4. The $\mathbf{\Delta H^{l-x}(T)}$ function shows a decrease with decreasing temperature, bearing a smaller value than $\mathbf{\Delta H_m}$, because of the continuous increase in the heat capacity difference of the undercooled liquid and crystalline mixture (Figure 6-3). This function illustrates the changes in the crystallization enthalpy as depicted in Figure 6-4, where the circles in Figure 6-4 (c), showing measured crystallization enthalpies during isothermal heating through FDSC measurements for

$Pd_{37}Ni_{37}S_{26}$, are in good agreement with the $\Delta H^{l-x}(T)$ function calculated through Eq. (2-3), confirming the experimental c_p measurements.

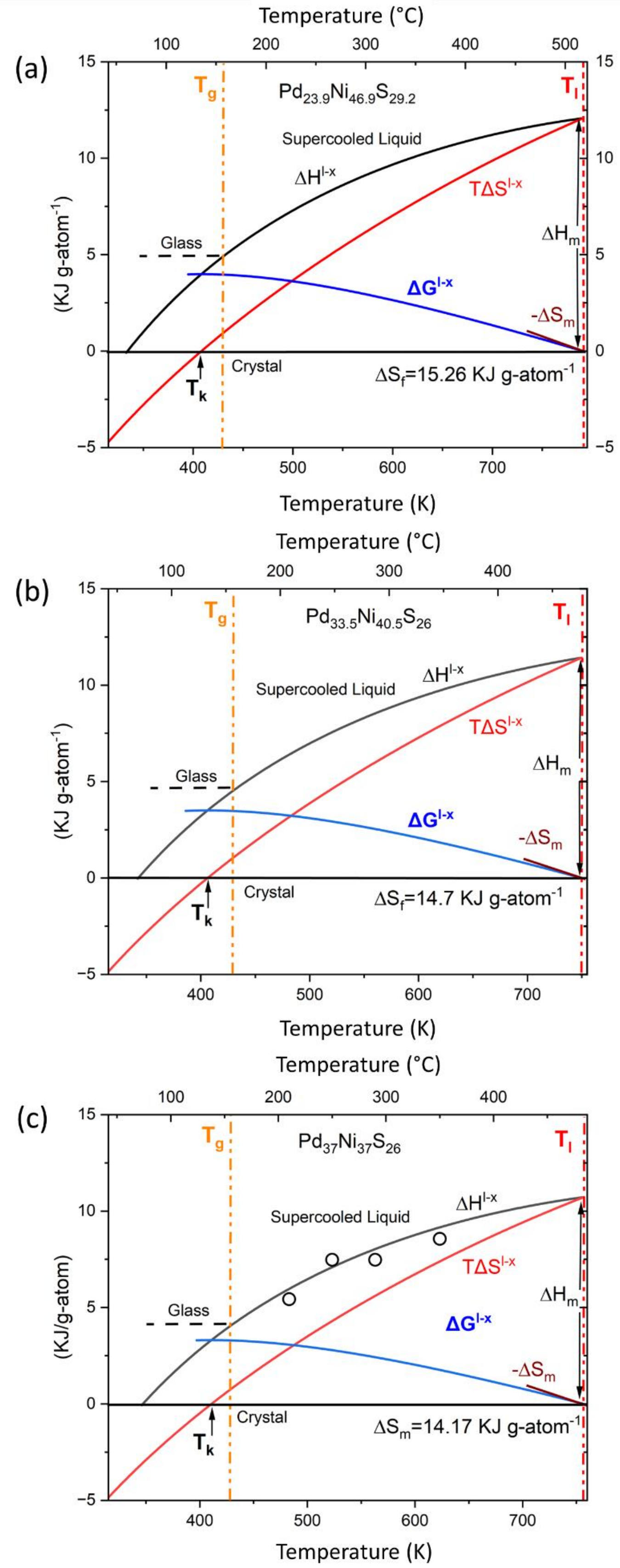
(a)
Temperature (°C)
100
200
300
400
500
15
10
5
0
−5
(KJ g-atom^{-1})
T_g
$Pd_{23.9}Ni_{46.9}S_{29.2}$
T_l
Supercooled Liquid
ΔH^{l-x}
$T\Delta S^{l-x}$
Glass
ΔH_m
ΔG^{l-x}
$-\Delta S_m$
Crystal
T_k
ΔS_f=15.26 KJ g-atom^{-1}
400
500
600
700
Temperature (K)
(b)
Temperature (°C)
100
200
300
400
15
10
5
0
−5
(KJ g-atom^{-1})
T_g
$Pd_{33.5}Ni_{40.5}S_{26}$
T_l
ΔH^{l-x}
Supercooled Liquid
$T\Delta S^{l-x}$
ΔH_m
Glass
ΔG^{l-x}
$-\Delta S_m$
Crystal
T_k
ΔS_f=14.7 KJ g-atom^{-1}
400
500
600
700
Temperature (K)
(c)
Temperature (°C)
100
200
300
400
15
10
5
0
−5
(KJ/g-atom)
T_g
$Pd_{37}Ni_{37}S_{26}$
T_l
ΔH^{l-x}
Supercooled Liquid
$T\Delta S^{l-x}$
ΔH_m
Glass
ΔG^{l-x}
$-\Delta S_m$
Crystal
T_k
ΔS_m=14.17 KJ g-atom^{-1}
400
500
600
700
Temperature (K)

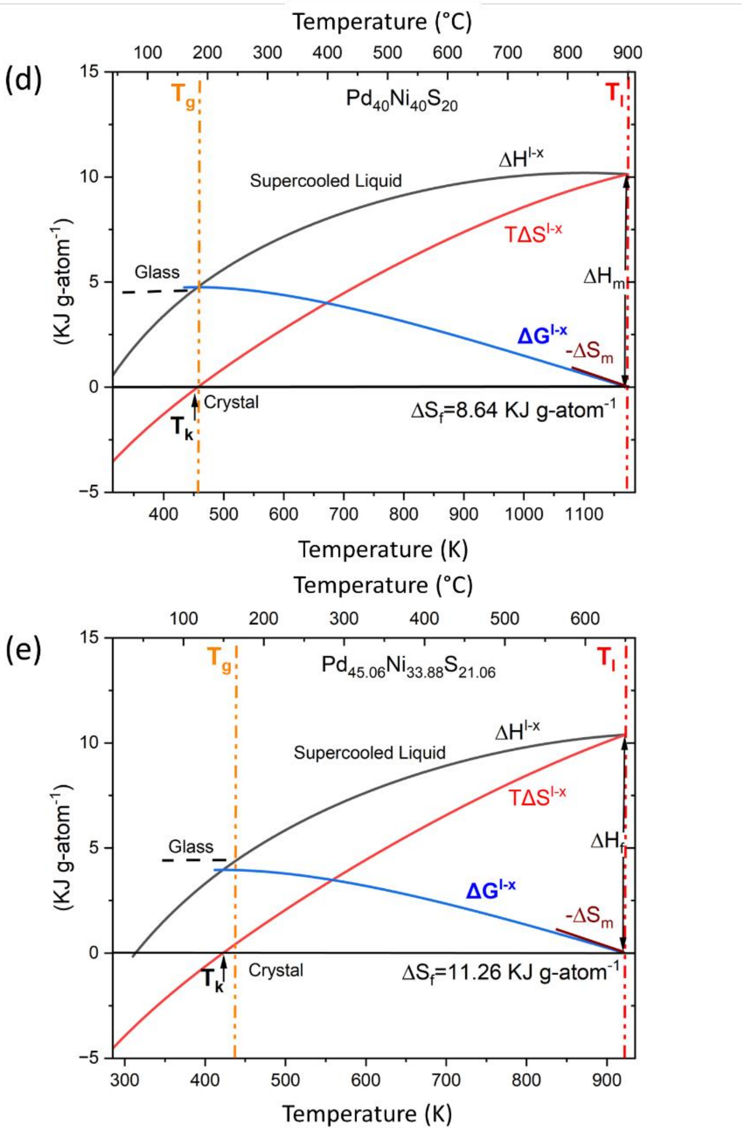

Figure 6-4. Changes in the excess enthalpy ΔH^{l-x}, scaled entropy $\Delta S^{l-x}$and Gibbs free energy ΔG^{l-x} with temperature for Pd-Ni-S alloy variations calculated using Eq. (2-2), (2-3) and (2-4). Circles shown in (c) for $Pd_{37}Ni_{37}S_{26}$ are ΔH_x values obtained during isothermal FDSC measurements.

6.1.4 CALPHAD modeling

The calculated isothermal sections of the Pd-Ni-S ternary phase diagram at 673 K, 823 K, and 998 K are presented in Figure 6-5 (a-c), which agree well with the experimental results obtained by Karup-Moller and Makovicky (dashed blue lines) [19].

The calculated heat capacities of the liquid phase at various compositions also agree well with the experimental data (Figure 6-6). Additionally, the calculated enthalpy change is also close to the results listed in Table 6-1. It can be concluded that the new thermodynamic dataset for the Pd-Ni-

S ternary system can adequately describe the thermodynamic properties of the system. The thermodynamic assessment and the dataset can be found in a forthcoming publication.

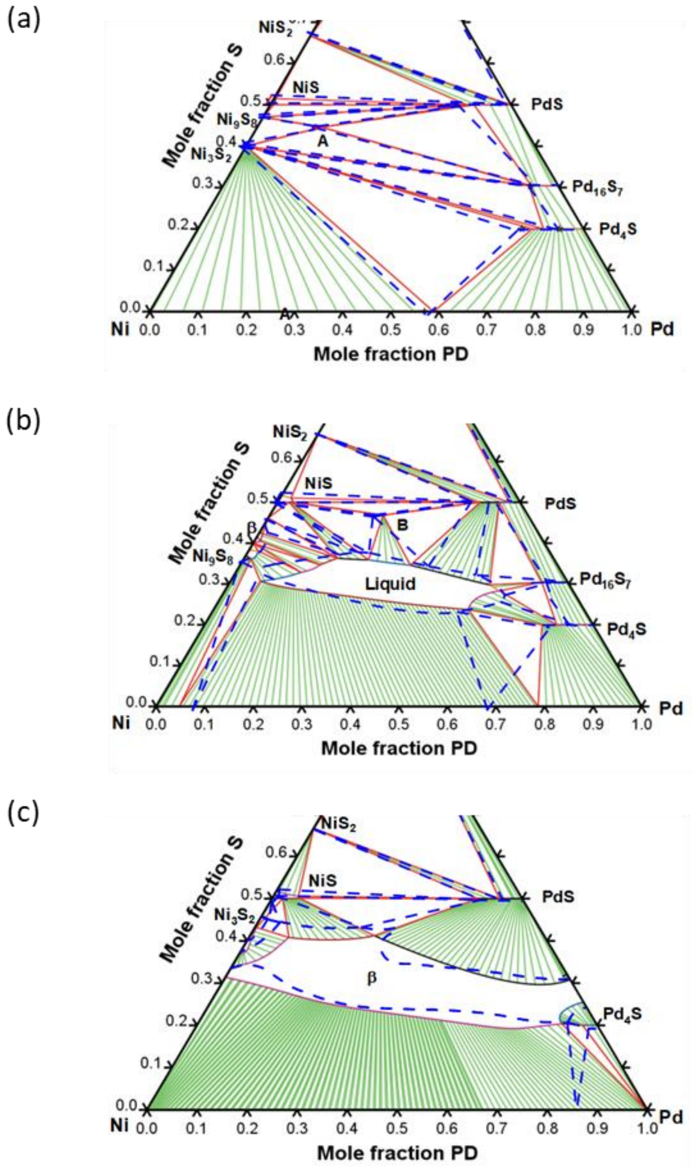

Figure 6-5. Calculated isothermal sections of the Pd-Ni-S ternary phase diagram at (a) 673 K, (b) 823 K, and (c) 998 K. Dashed blue lines indicate the experimental results obtained by Karup-Moller and Makovicky.

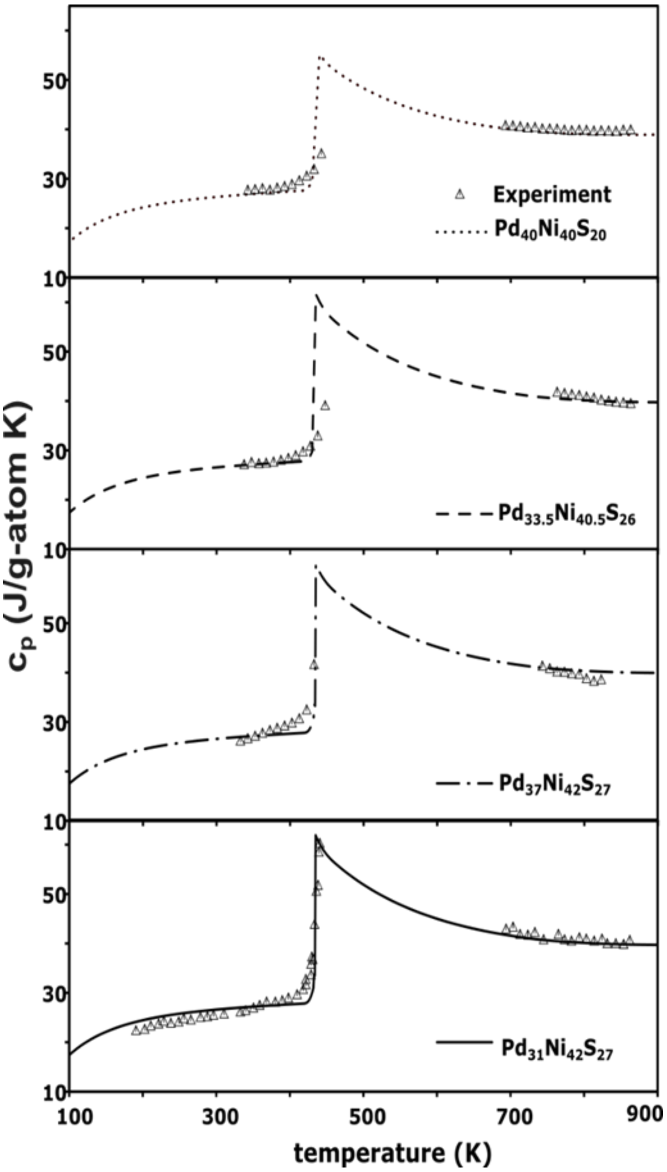

Figure 6-6. Comparison between the calculated heat capacity and the experimental results for some of Pd-Ni-S glass forming compositions. The empty triangles indicate the experimentally measured c_p data and the solid lines are the modeling result.

6.2 Kinetic Studies

6.2.1 Critical Cooling Rate Determination

The findings from CCR measurements with an annealing temperature of 923 K and a holding time of 0.1 s are depicted in Figure 6-7, illustrating the change in crystallization enthalpy with respect to the logarithmic scale of the applied cooling rate. The required CCR for achieving a constant crystallization enthalpy (100%), indicating an initially fully amorphous sample, is about 8390, 9035, and 4901 K s^{-1} for the examined $Pd_{31}Ni_{42}S_{27}$, $Pd_{33.5}Ni_{40.5}S_{26}$, and $Pd_{37}Ni_{37}S_{26}$ compositions respectively, and is determined from the intersection of the two guiding lines of the plateau and the slope. The calculated critical cooling rate (CCR) can be compared to the macroscopic critical casting thickness d_c using the empirical formula [178] as

$$R_c = \frac{10}{d_c^2}\ K\ cm^2 s^{-1} \qquad \textbf{(6-5)},$$

where R_c is the CCR in K s^{-1} and d_c is the critical casting thickness in cm. Considering the experimental d_c of 2 mm in the case of $Pd_{37}Ni_{37}S_{26}$ and 1.5 mm for $Pd_{31}Ni_{42}S_{27}$ [18], an R_c of 250 K s^{-1} for the $Pd_{37}Ni_{37}S_{26}$ and 444 K s^{-1} for the $Pd_{31}Ni_{42}S_{27}$ would be estimated. Although the calculated R_c values exhibit a qualitative trend relative to the critical d_c values, the determination of the CCR using FDSC does not directly correlate with the macroscopic glass-forming ability when applying the established formula based on the experimental critical thickness data. This discrepancy is detected in Au-based BMGs as well [128,146], which has been attributed to the high surface/ volume ratio for small-scale samples, and the easy crystallization at the surface [179,180]. However, in the case of Pd-Ni-S variations, the volatile sulfur is already a potential source of inhomogeneities in the liquid, affecting their CCR strongly.

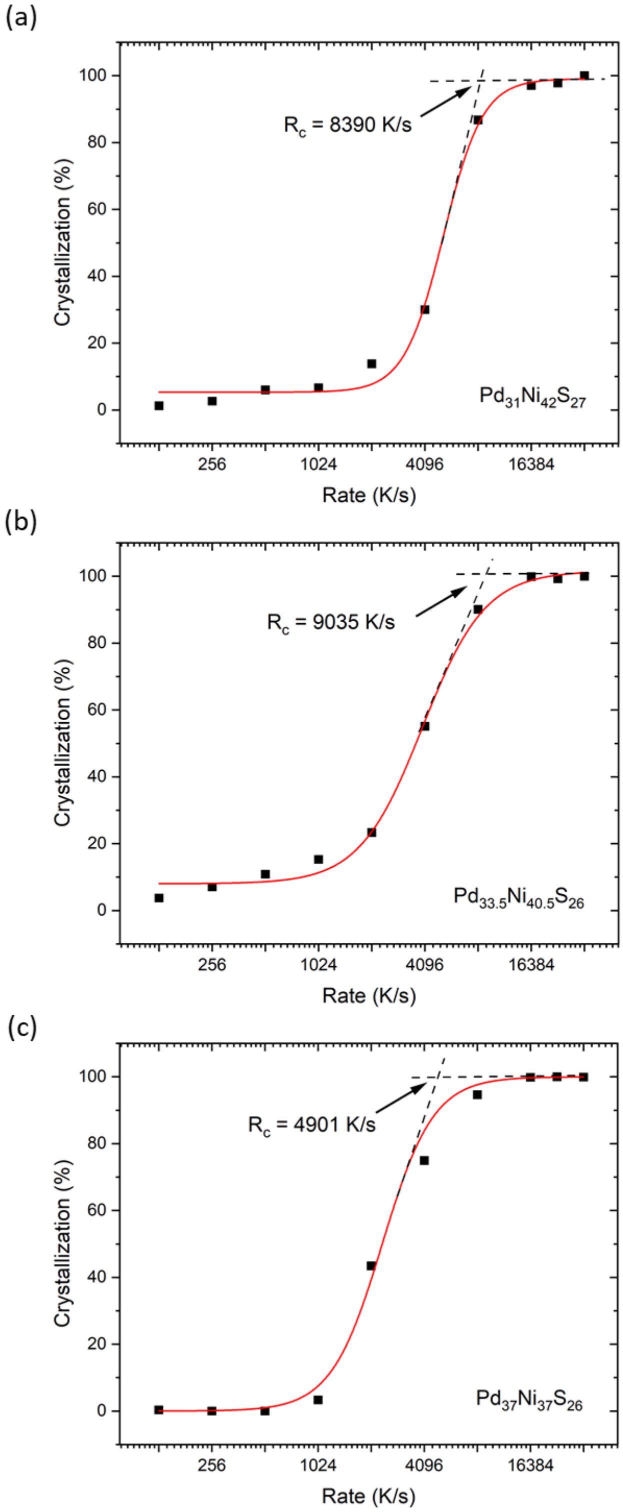

Figure 6-7. Changes in Crystallization enthalpy of a) $Pd_{31}Ni_{42}S_{27}$, b) $Pd_{33.5}Ni_{40.5}S_{26}$, and c) $Pd_{37}Ni_{37}S_{26}$ over a logarithmic cooling rate. Each enthalpy measurement was conducted under a constant heating rate of 100 K s^{-1} following an initial cooling from a temperature significantly above the liquidus temperature of the respective alloy. The point at which the plateau value in crystallization enthalpy is reached signifies the range where fully amorphous samples were achieved, indicating that the critical cooling rate was exceeded.

6.3 Crystallization of the undercooled liquid

6.3.1 Aerodynamic Levitation Study

Based on the Karup-Moller study [19], the selected Pd-Ni-S variations are located within the ternary phase field of the FCC (Pd,Ni) solid solution, and the binary intermetallic compounds of Pd_4S and Ni_3S_2 at 400 °C (673 K) (below their eutectic melting temperature). Therefore, one of these phases is expected to pop out as the primary crystalline phase during cooling experiments. This is confirmed by the in-situ WAXS experiments, where the diffraction pattern of these equilibrium phases was simulated using the Vesta software [167] and compared to the obtained data and no metastable phases could be identified.

The recorded solidification behavior for Pd-Ni-S alloy variations is compared with the Scheil simulations. The Scheil Calculator in Thermo-Calc software enables easy setup of Scheil Solidification Simulations, which model non-equilibrium or partial-equilibrium solidification by assuming infinitely fast diffusion in the liquid phase and zero or limited diffusion in the solid phase. In fast non-equilibrium solidification, the cooling rate is too high to allow the complete redistribution of alloying elements just like an equilibrium condition. The Scheil-Gulliver equation, and its derivatives utilized by the Scheil Calculator, account for the reduced or limited diffusion taking place in the solidified structure in a relatively simple but efficient manner, providing a better estimate of the actual state of the material during solidification. Hence, by using the Scheil Calculator, it is possible to achieve a more accurate estimate of phases present in the microstructure, the solidification range, the extent of segregation, and so on, for a material following solidification [181].

The results for Pd-Ni-S variations are shown in Figure 6-8. During the solidification of Pd-Ni-S alloy variations, a recalescence was recorded which was more pronounced in the case of $Pd_{31}Ni_{42}S_{27}$, $Pd_{33.5}Ni_{40.5}S_{26}$, and $Pd_{37}Ni_{37}S_{26}$ compositions, which is shown exemplarily for $Pd_{33.5}Ni_{40.5}S_{26}$ in Figure 6-8 (b). For this composition, the CALPHAD calculation shows that first during primary crystallization only small amounts of (Pd, Ni) solid solution are formed down to about 744 K, then co-precipitation with Ni_3S_2 takes place as the temperature decreases down to about 736K, followed by the formation of Pd_4S. This sequence, in such a small temperature interval of less than 20K, is hard to resolve in the synchrotron measurement. Therefore, the synchrotron spectra, detects the formation of all crystalline phases at the same time, which is accompanied by a large heat release due to recalescence, increasing the detected temperature from 707 K to 730 K for this composition. This fast solidification is also observed in the case of $Pd_{31}Ni_{42}S_{27}$ and $Pd_{37}Ni_{37}S_{26}$, where the primary phase is hard to detect through synchrotron measurements.

The temperature is also shifted to lower temperatures by about 50 K compared to the Scheil simulations, as a result of the undercooling caused by the high cooling rate and the containerless processing condition in the levitation device. However, the achieved cooling rate is not yet as high as the attainable rate in ultra-fast calorimetry. It is important to note that Scheil simulation is purely thermodynamic and does not account for kinetic aspects, such as undercooling due to rapid cooling, which can alter the phase formation sequence (see section 7.1.2, Figure 7-3).

Regarding the degree of oxidation occurring in ADL, it is acknowledged that aerodynamic levitation does not achieve as high a vacuum level as electrostatic levitation. Consequently, a certain degree of oxidation was observed in some samples. However, the level of oxidation was not significant enough to alter the phase formation. This conclusion is supported by the fact that a wide range of compositions (off-eutectic compositions, with a clear first phase formation) was analyzed, and the resulting data consistently matched the Scheil-predicted phase formation sequence.

In the case of $Pd_{23.9}Ni_{46.9}S_{29.2}$ composition, CALPHAD predicts the formation of the Ni_3S_2 phase, which is perfectly in line with the synchrotron observations and expectations, given its proximity to the Ni_3S_2 rich side in the ternary phase diagram.

For $Pd_{40}Ni_{40}S_{20}$ and $Pd_{45.06}Ni_{33.88}S_{21.06}$ compositions, the formation of (Pd, Ni) solid solution is evident in synchrotron observations, which is supported by CALPHAD calculations as well.

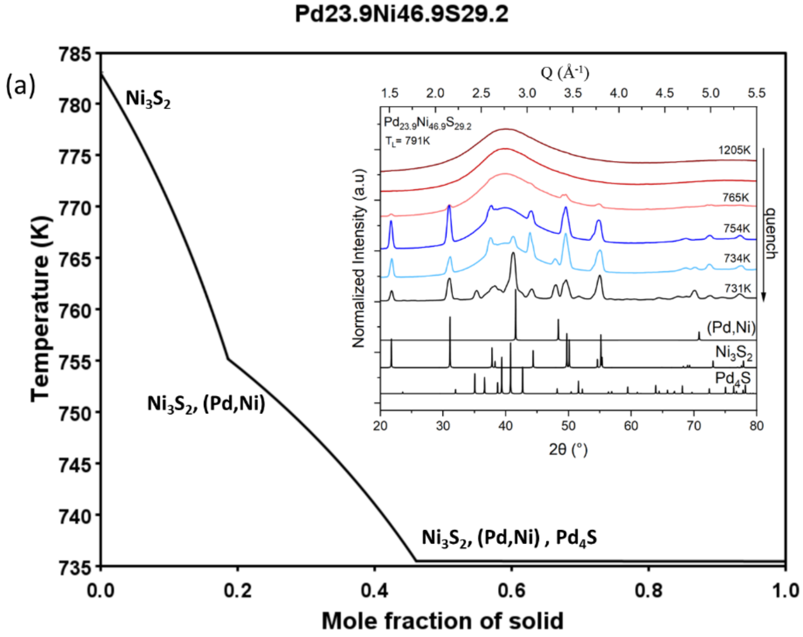
Pd23.9Ni46.9S29.2
(a)
Ni_3S_2
Ni_3S_2, (Pd,Ni)
Ni_3S_2, (Pd,Ni) , Pd_4S
Temperature (K)
785
780
775
770
765
760
755
750
745
740
735
0.0
0.2
0.4
0.6
0.8
1.0
Mole fraction of solid
Q (Å^{-1})
1.5
2.0
2.5
3.0
3.5
4.0
4.5
5.0
5.5
$Pd_{23.9}Ni_{46.9}S_{29.2}$
T_L= 791K
1205K
765K
754K
734K
731K
quench
Normalized Intensity (a.u)
(Pd,Ni)
Ni_3S_2
Pd_4S
20
30
40
50
60
70
80
2θ (°)

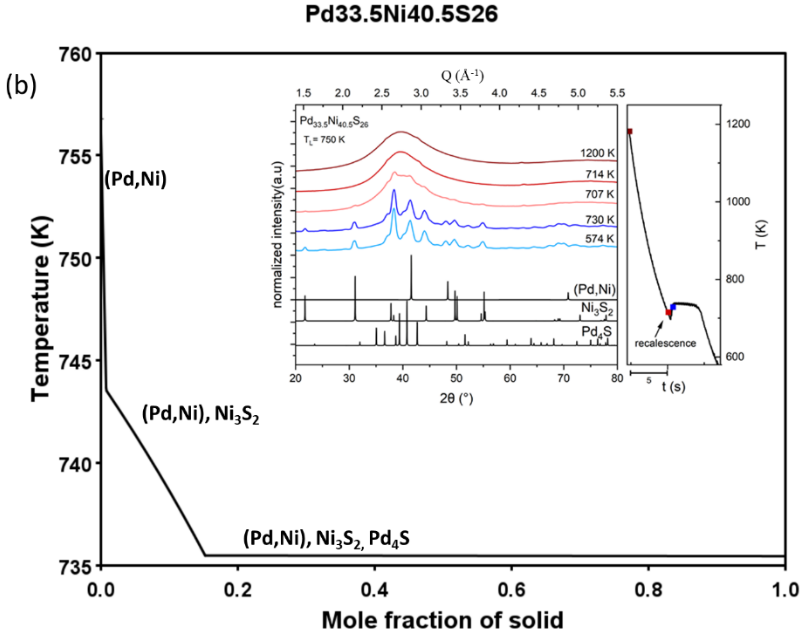
Pd33.5Ni40.5S26
(b)
(Pd,Ni)
(Pd,Ni), Ni_3S_2
(Pd,Ni), Ni_3S_2, Pd_4S
Temperature (K)
760
755
750
745
740
735
0.0
0.2
0.4
0.6
0.8
1.0
Mole fraction of solid
Q (Å^{-1})
1.5
2.0
2.5
3.0
3.5
4.0
4.5
5.0
5.5
$Pd_{33.5}Ni_{40.5}S_{26}$
T_L= 750 K
1200 K
714 K
707 K
730 K
574 K
normalized intensity(a.u)
(Pd,Ni)
Ni_3S_2
Pd_4S
20
30
40
50
60
70
80
2θ (°)
1200
1000
800
600
T (K)
recalescence
5
t (s)

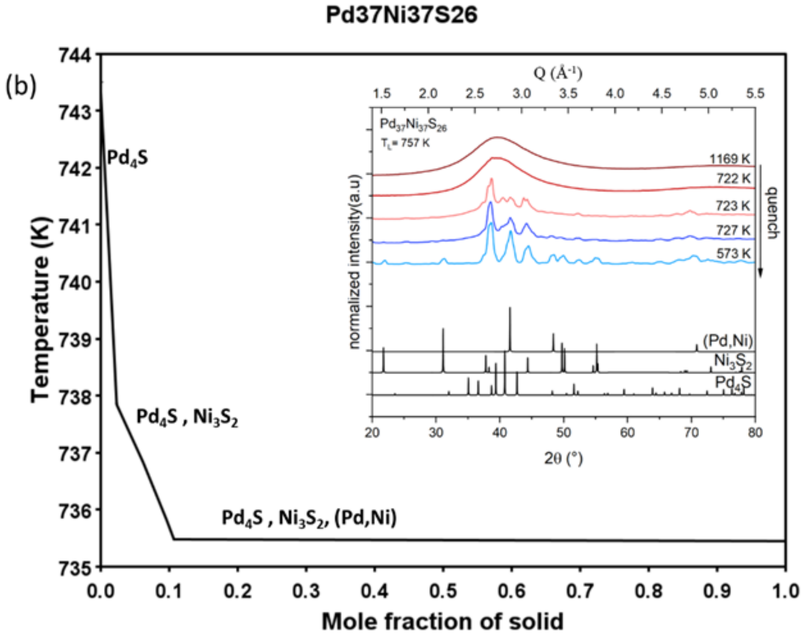
Pd37Ni37S26
(b)
Temperature (K)
744
743
742
741
740
739
738
737
736
735
Pd$_4$S
Pd$_4$S , Ni$_3$S$_2$
Pd$_4$S , Ni$_3$S$_2$, (Pd,Ni)
0.0 0.1 0.2 0.3 0.4 0.5 0.6 0.7 0.8 0.9 1.0
Mole fraction of solid
Q (Å^{-1})
1.5 2.0 2.5 3.0 3.5 4.0 4.5 5.0 5.5
Pd$_{37}$Ni$_{37}$S$_{26}$
T$_L$ = 757 K
normalized intensity(a.u)
1169 K
722 K
723 K
727 K
573 K
quench
(Pd,Ni)
Ni$_3$S$_2$
Pd$_4$S
20 30 40 50 60 70 80
2θ (°)

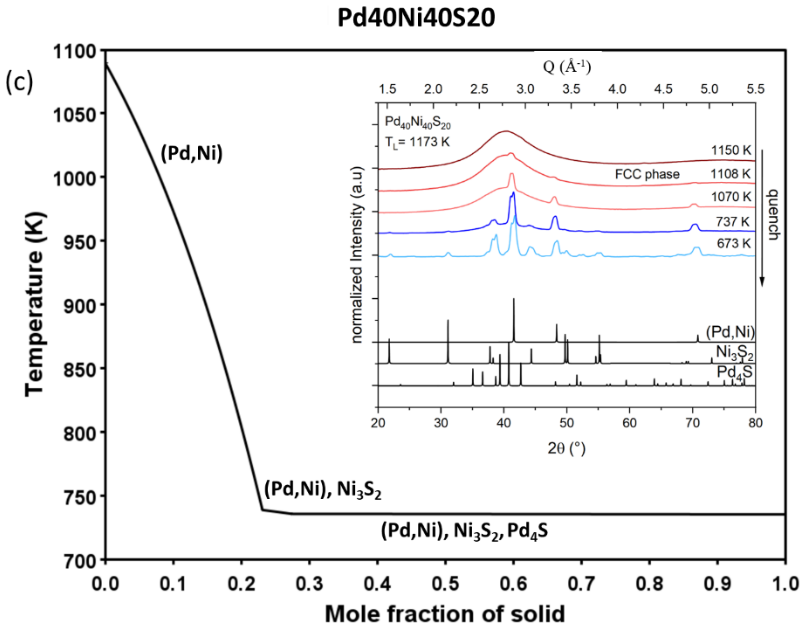
Pd40Ni40S20
(c)
Temperature (K)
1100
1050
1000
950
900
850
800
750
700
(Pd,Ni)
(Pd,Ni), Ni$_3$S$_2$
(Pd,Ni), Ni$_3$S$_2$, Pd$_4$S
0.0 0.1 0.2 0.3 0.4 0.5 0.6 0.7 0.8 0.9 1.0
Mole fraction of solid
Q (Å^{-1})
1.5 2.0 2.5 3.0 3.5 4.0 4.5 5.0 5.5
Pd$_{40}$Ni$_{40}$S$_{20}$
T$_L$ = 1173 K
normalized Intensity (a.u)
1150 K
FCC phase
1108 K
1070 K
737 K
673 K
quench
(Pd,Ni)
Ni$_3$S$_2$
Pd$_4$S
20 30 40 50 60 70 80
2θ (°)

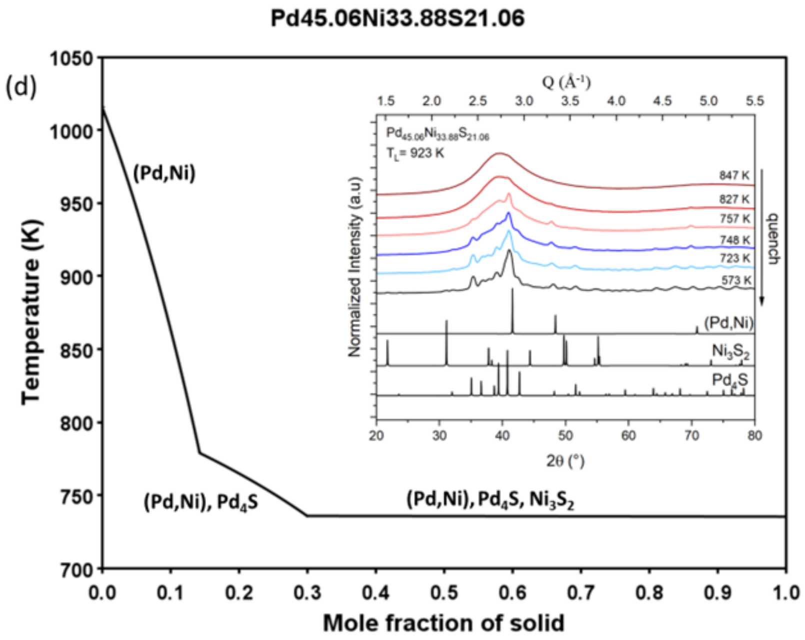

Figure 6-8. Scheil solidification simulation for Pd-Ni-S alloy variations in comparison with the in-situ WAXS measurement at 200 K/s cooling rate which is accompanied by a heat release due to recalescence, shown exemplarily for $Pd_{33.5}Ni_{40.5}S_{26}$. The simulated diffraction patterns of the crystalline equilibrium phases including (Pd, Ni) solid solution, Ni_3S_2, and Pd_4S are shown and used to detect the forming phases.

6.3.2 Time-Temperature-Transformation (TTT) Diagrams

The isothermal TTT diagrams of the $Pd_{31}Ni_{42}S_{27}$, $Pd_{33.5}Ni_{40.5}S_{26}$, and $Pd_{37}Ni_{37}S_{26}$ are depicted in Figure 6-9.

In Figure 6-9, only the crystallization time of 1% is shown for the measured compositions, which shows the typical C-shape of TTT diagrams, with a greater dispersion of data at higher temperatures due to nucleation-controlled crystallization as expected. These data are used for the construction of fitted lines, using the Johnson-Mehl-Avrami-Kolmogorov (Eq. (2-24)), and a detailed discussion on these fits is provided later in the discussion section.

For $Pd_{31}Ni_{42}S_{27}$, the isothermal crystallization data acquired in a conventional DSC (Perkin Elmer DSC 8500) in heating from the glassy state and in cooling from the stable liquid state from Kuball's work [42] is also added to the TTT diagram shown with square symbols. The DSC data measured at longer times and lower temperatures, as well as higher temperatures in regards to the FDSC data, are in good agreement with the crystallization times measured using FDSC. Such a good compatibility has already been reported in other studies [146,182], and proves the accuracy of measurements.

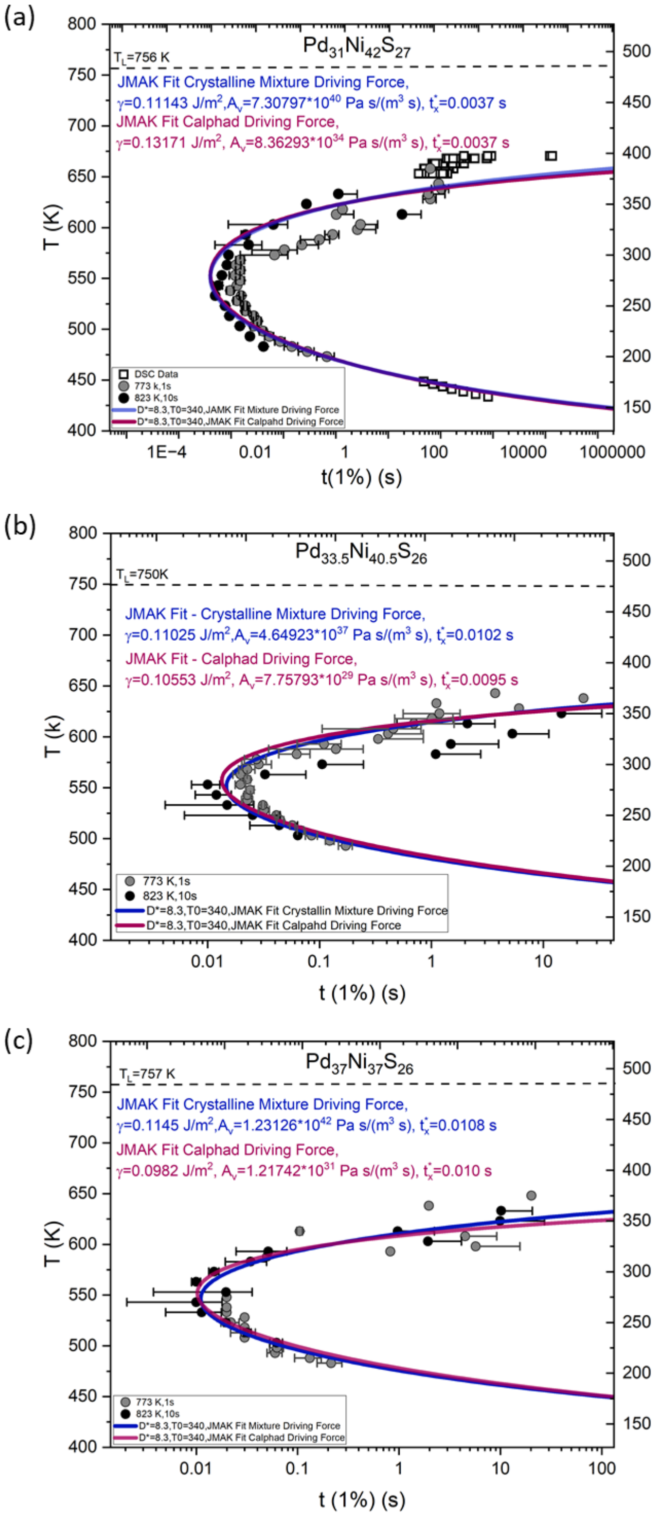

Figure 6-9. Isothermal time–temperature-transformation (TTT) diagram of a) $Pd_{31}Ni_{42}S_{27}$, b) $Pd_{33.5}Ni_{40.5}S_{26}$, and c) $Pd_{37}Ni_{37}S_{26}$ determined in fast differential scanning calorimetry (FDSC) (circles) and conventional DSC (squares) for $Pd_{31}Ni_{42}S_{27}$ from [42]. The dark blue and crimson curves show the Johnson–Mehl–Avrami fitting of the experimental data using experimentally determined crystalline mixture driving force and Calphad driving force, respectively.

7 Discussion

7.1 Gibbs free energy and driving force for crystallization

7.1.1 Experimental approach

Without CALPHAD calculations, we usually determine the Gibbs free energy difference between the undercooled liquid and the crystalline mixture using Eq. (2-5) as described before and use the thermodynamic calculations to estimate the driving force. In Figure 7-1 (a), the calculated Gibbs free energy curves for Pd-Ni-S variations as a function of temperature, normalized to the liquidus temperature, are compared. They reveal that the driving force at the glass transition temperature is very similar for all variations, with $Pd_{37}Ni_{37}S_{26}$ exhibiting the smallest value. The compositional dependence of ΔG^{l-x} follows the changes of the enthalpy and entropy of fusion ΔS_m in the system (Table 6-1), which has been already seen in Au, Pt, and Pd based systems [176,183].

As can be seen in Figure 7-1 (b), compared to other better glass-forming systems, especially Pd-based glass-forming alloys such as $Pd_{43}Ni_{10}Cu_{27}P_{20}$ [1] and $Pd_{40}Ni_{40}P_{20}$ [184], Pd-Ni-S alloy variations show a higher driving force for crystallization, explaining their poor glass forming ability. However, the Gibbs free energy difference shown in Figure 7-1 is only an estimation of the real driving force for crystallization. As depicted schematically in Figure 7-2 in a binary A-B system, the calculated ΔG^{l-x} using Eq. (2-2) in a multiphase system, always refers to the Gibbs free energy difference between the (undercooled) liquid and the crystalline mixture, since $\Delta H_m$and ΔS_m are derived from the melting process of the crystalline mixture and $c_p^x(T)$ is also the measured specific heat capacity of the crystalline mixture. Hence, it is important to note that the Gibbs free energy difference between the liquid and the crystalline mixture is only a lower limit for the driving force for the primary crystallization. The actual driving force for nucleation is correlated to the changes in the chemical potential of the system, if nuclei of a certain crystalline phase are formed [185]. As in Figure 7-2, the driving force for the formation of a nucleus of the α-phase is calculated by the parallel tangent construction (black dashed lines). Therefore, the vertical distance between the two tangents, $\Delta\mu_A^{L-\alpha}$, represents the real driving force for the nucleation of a primary α-nucleus with the composition $X_n(T)$ from the liquid with the composition X_q. From Figure 7-2, for a composition at X_q at $T < T_{eut}$ in a binary A-B system, it is evident that ΔG^{l-x} only gives an approximation of the driving force (lower bound) for the formation of a crystalline nucleus [3]. This illustrates the need for the CALPHAD approach, which is capable of calculating the more realistic crystallization driving force of the first-appearing crystalline phase.

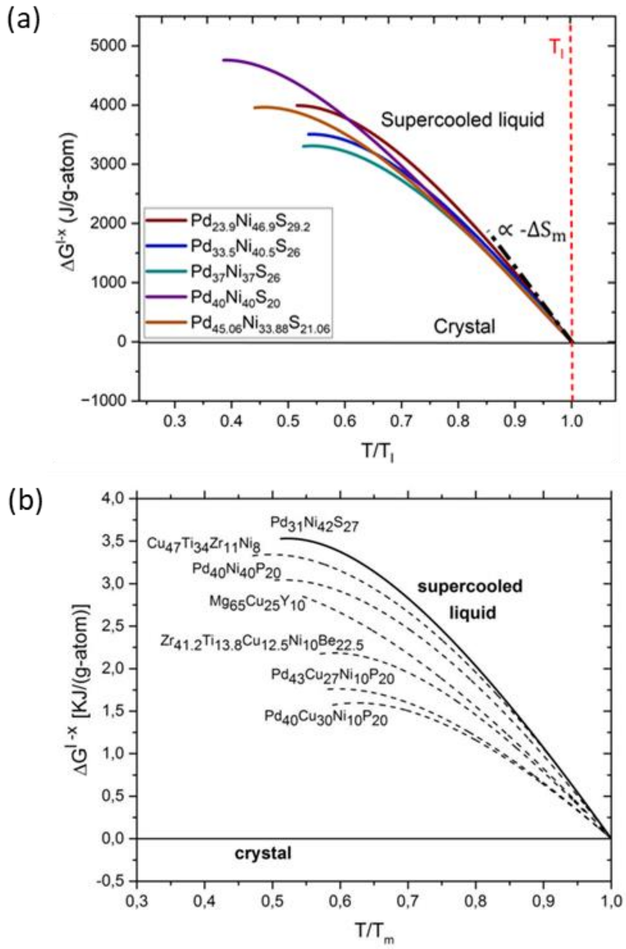

Figure 7-1. Calculated Gibbs free energy function with respect to the crystalline state from Eq. (2-2), a) for the Pd-Ni-S alloy variations, The slope of ΔG^{l-x} at T_l is proportional to $-\Delta S_m$, b) in comparison to other glass-forming systems, taken from [2].

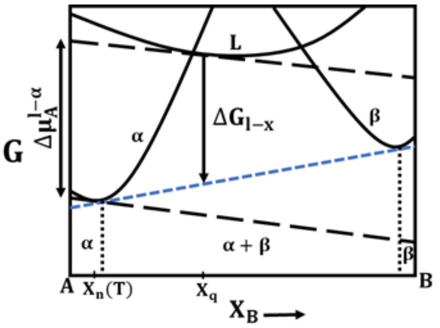

Figure 7-2. Schematic Gibbs free energy curves for the competing phases for a nominal composition of X_q at T< T_{eut} in a binary A-B system. ΔG^{l-x} is the Gibbs free energy difference between the liquid and the crystalline mixture $(\alpha + \beta)$. $\Delta\mu_A^{L-\alpha}$ is the actual driving force for the nucleation of an α-nucleus of the composition $X_n(T)$ within the liquid with the composition X_q [3]. Therefore ΔG^{l-x} is genelly underestimating the driving force for primary crystallization and can be considered a lower bound.

7.1.2 CALPHAD approach

The driving force for the crystallization of each crystalline equilibrium phase from the undercooled liquid can now be determined through CALPHAD calculations. This assessment spans across temperatures from the liquidus temperature down to the glass transition, employing the double tangent construction method as depicted in Figure 7-2. The driving force of the phase transformation is defined by the vertical distance between the tangent to the metastable liquid state (L) and the tangent line at the lowest lying equilibrium state (α in case of Figure 7-2).

Figure 7-3 shows the CALPHAD calculations result of the driving force for crystallization of all three crystalline phases ((Pd,Ni) solid solution, Ni_3S_2 and Pd_4S) for $Pd_{23.9}Ni_{46.9}S_{29.2}$, $Pd_{31}Ni_{42}S_{27}$, $Pd_{33.5}Ni_{40.5}S_{26}$, $Pd_{37}Ni_{37}S_{26}$, $Pd_{40}Ni_{40}S_{20}$, and $Pd_{45.06}Ni_{33.88}S_{21.06}$ composition. Additionally, the experimentally determined Gibbs free energy of the crystalline mixture is included (black curve) for comparison. Discrepancies in the initial points of the driving forces are observed, likely stemming from the incongruent melting behavior of multi-component alloys and varying assumptions between experimental and modeling approaches. When a certain level of undercooling of at least 0.8 T_m necessary for homogenous nucleation [186] is maintained during the cooling process, and the undercooled liquid remains homogeneous with the same composition as the high-temperature liquid, the initial phase to form will consistently be the one with the highest driving force at that temperature. For Pd-Ni-S alloy variations, starting with $Pd_{23.9}Ni_{46.9}S_{29.2}$ from the Ni_3S_2 rich side and going towards the eutectic point, Ni_3S_2 emerges as the primary phase. As previously discussed, here we could see the clear difference between the actual driving force calculated by CALPHAD and the calculated experimental driving force for all the compositions, which becomes smaller as we approach the eutectic point. This shows that our experimental approach is a good approximation tool for near-eutectic compositions, however in the case of off-eutectic compositions, one should be more careful as the discrepancy gets bigger. This holds significance in the TTT diagram, where Ni_3S_2 is anticipated to form after rapid cooling and the sample's isothermal holding at the respective temperature. Subsequently, the interfacial energy related to this phase will be determined by employing the calculated driving forces within the Johnson-Mehl-Avrami-Kolmgrov (JMAK) fit (Eq. (2-24)) of the experimental crystallization times.

Regarding $Pd_{40}Ni_{40}S_{20}$, and $Pd_{45.06}Ni_{33.88}S_{21.06}$, it can be seen clearly in Figure 7-3 (e-f) that (Pd, Ni) solid solution is the phase with the highest driving force which is in line with what was observed through in-situ HEXRD measurements during heating and cooling of these two compositions (Figure 6-2 and 6-8), where (Pd, Ni) solid solution was the last to melt and the first phase to form.

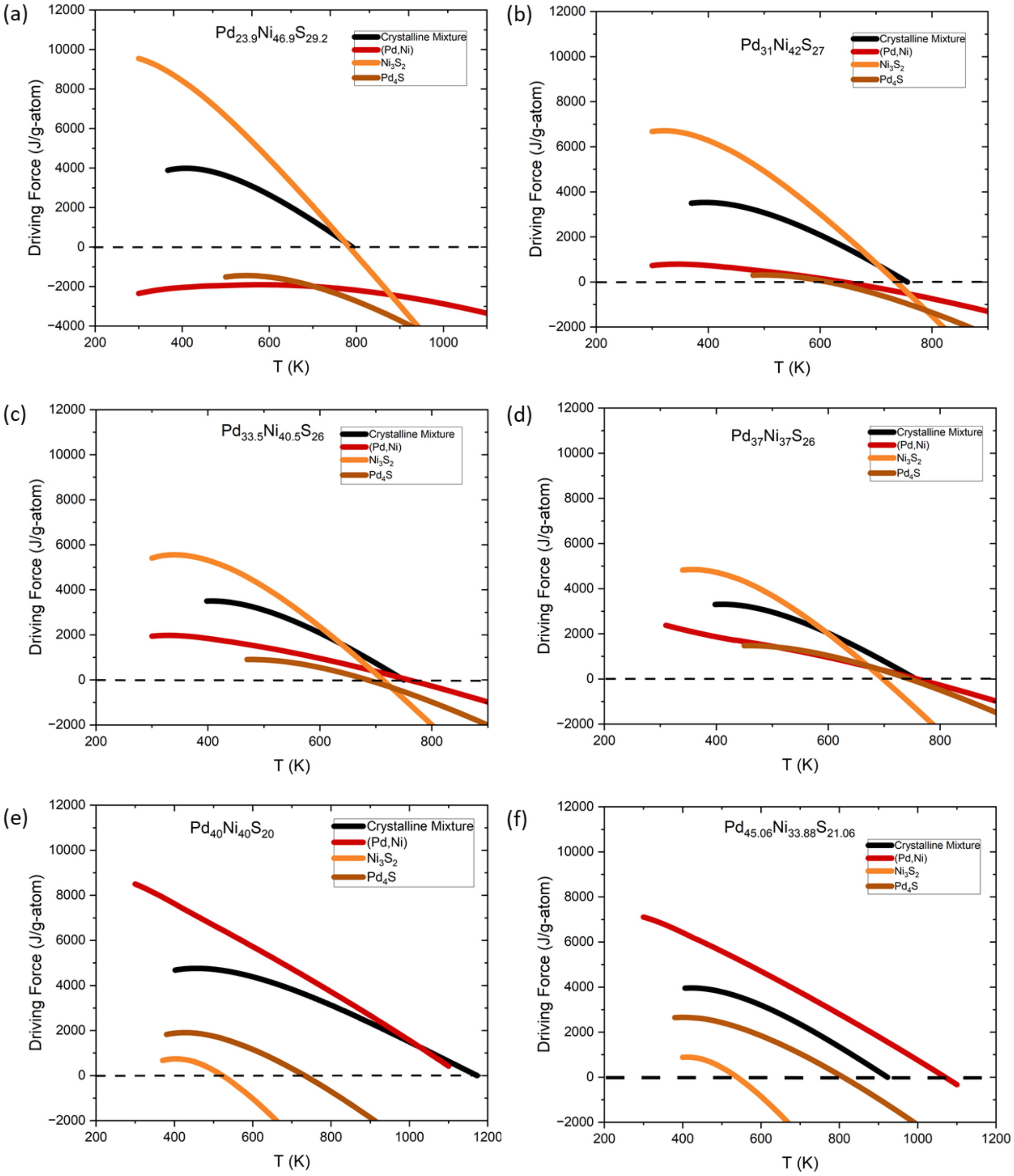

Figure 7-3. Calculated driving forces for crystallization of all the crystalline phases that compete with the undercooled liquid for a) $Pd_{23.9}Ni_{46.9}S_{29.2}$, b) $Pd_{31}Ni_{42}S_{27}$, c) $Pd_{33.5}Ni_{40.5}S_{26}$, d) $Pd_{37}Ni_{37}S_{26}$, e) $Pd_{40}Ni_{40}S_{20}$, and f) $Pd_{45.06}Ni_{33.88}S_{21.06}$ in comparison with the calculated $\boldsymbol{\Delta G^{l-x}}$ between the undercooled liquid and the crystalline mixture. Close to the eutectic (c,d) the prediction for primary crystallization from the crystalline mixture, $\boldsymbol{\Delta G^{l-x}}$, and the Calphad calculation $\Delta\mu^{l-i}$ in the relevant temperature range from about 550K to 625K (see Figure 6-8) are close. In the off-eutectic cases (a,b, e, f) the crystalline mixture underestimates the driving force as it has been illustrated in Figure 7-2.

7.2 Fragility estimations

For a proper description of the TTT diagrams, measured in the framework of this study as plotted in Figure 6-9, the kinetics of the undercooled liquid need to be estimated. Regarding kinetics, the fragility of the liquid phase, as classified by Angell, plays a pivotal role in glass formation, as previously discussed in section 2.4. [48,187].

Figure 7-4 (a) shows $\log_{10}(\tau_d)$ of the $Pd_{31}Ni_{42}S_{27}$, $Pd_{33.5}Ni_{40.5}S_{26}$, and $Pd_{37}Ni_{37}S_{26}$ liquid over 1/T measured at a base frequency of 10 Hz using the step response analysis method. As shown in [188], obtaining the exact τ_0 value for a particular liquid is challenging, leading to uncertainty regarding the comparability of Vogel-Fulcher-Tammann (VFT) fits across different systems within the timescale regime. To circumvent these challenges, m-fragilities are determined by conducting linear Arrhenius-like fits of $\log_{10}(\tau_d)$ data [188], using Eq. (2-10). Figure 7-4 (b) shows the respective fits in an Angell plot carried out in regard to the maximum $\log_{10}(\tau_d)$ data point which is the same for all the three compositions to define T^* and have a qualitative comparison of m_τ.

As depicted in Figure 7-4 (b), the linear fitted lines seem satisfactory, as the overall super-Arrhenius temperature dependence of τ_d can be deemed negligible over such a short temperature range. The calculated m-fragilities for $Pd_{31}Ni_{42}S_{27}$, $Pd_{37}Ni_{37}S_{26}$, and $Pd_{33.5}Ni_{40.5}S_{26}$ are 53.5, 51.2, and 39.6 respectively. Based on these results, $Pd_{33.5}Ni_{40.5}S_{26}$ is found to be a slightly stronger system, while $Pd_{31}Ni_{42}S_{27}$ and $Pd_{37}Ni_{37}S_{26}$ show very close m_τ values indicating their similar fragilities.

Another approach for fragility estimation is to use the connection between kinetic and thermodynamic properties to quantitatively determine the thermodynamic fragility [1,189]. As shown by Molecular dynamics simulations [190], the deeply supercooled liquid undergoes structural redistribution and ordering processes, resulting in significant variations in the specific heat capacity near the glass transition temperature. Based on Adam- Gibbs theory [56], as the liquid is further undercooled, the so-called cooperatively rearranging regions (CRRs) formed by groups of atoms grow in size and increase their degree of cooperativity. As a result, the number of available configurations within the system decreases, leading to a decrease in configurational entropy S_c. This decrease is accompanied by an increase in specific heat capacity, which is linked to the significant rise in viscosity and relaxation times as the glass transition is approached. Assuming a negligible distinction in vibrational entropy between the liquid and crystalline states [60], the excess entropy (entropy difference between undercooled liquid and crystalline state), $\Delta S^{\mathrm{l-x}}$, can be employed instead of S_c to depict the entropic alterations with temperature.

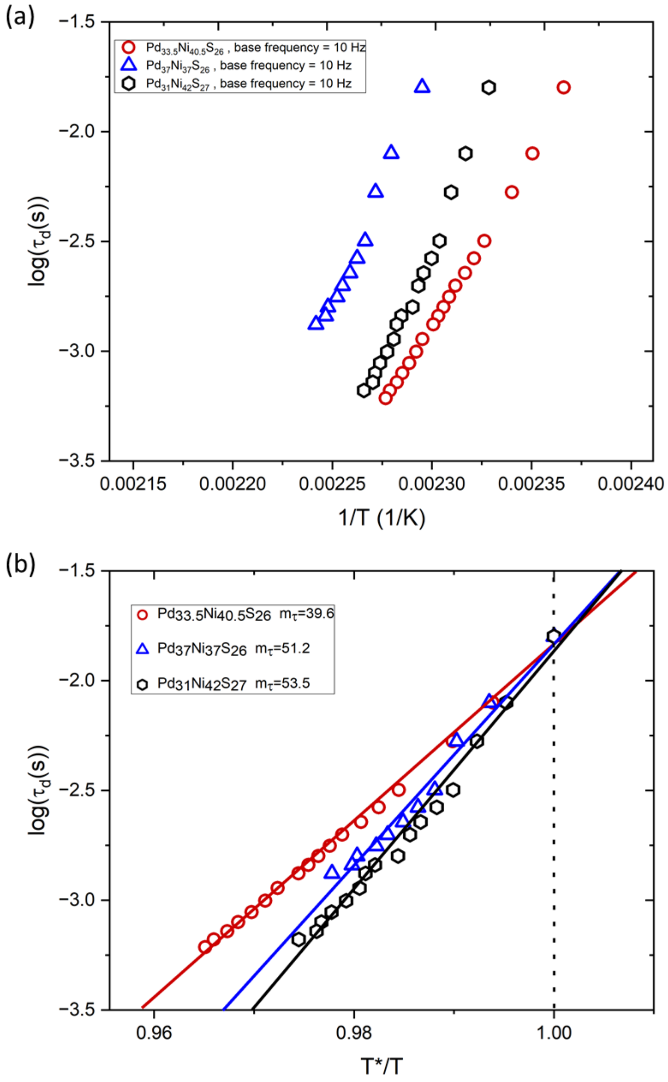

Figure 7-4. Relaxation data acquired by step response analysis, a) $\log_{10}(\tau_d)$ of the $Pd_{31}Ni_{42}S_{27}$, $Pd_{33.5}Ni_{40.5}S_{26}$, and $Pd_{37}Ni_{37}S_{26}$ liquid over 1/T measured at a base frequency of 10 Hz using the step response analysis method. b) Linear Arrhenius fits of τ_d (T) in an Angell-type diagram for all three compositions. The linear fits are done with regard to the maximum $\log_{10}(\tau_d)$ data point which is the same for all the three compositions to define T^* and the m-fragility (m_τ).

A qualitative connection between the concept of kinetic fragility and excess entropy was proposed by Angell et.al [58,190], in which instead of relying on relaxation time or viscosity, they utilized the change in configurational entropy or excess entropy around the glass transition to describe thermodynamic fragility. In this approach, considering $\frac{\mathrm{d}\Delta\mathrm{S}^{\mathrm{l-x}}}{\mathrm{dT}} = \frac{\Delta\mathrm{c}_\mathrm{p}^{\mathrm{l-x}}}{\mathrm{T}}$, and with the assumption $\Delta\mathrm{C}_\mathrm{p}^{\mathrm{l-x}}(\mathrm{T}_\mathrm{g}) \approx \Delta\mathrm{C}_\mathrm{p}^{\mathrm{l-g}}(\mathrm{T}_\mathrm{g})$, the difference in isobaric specific heat capacity between liquid and crystal $\Delta\mathrm{C}_\mathrm{p}^{\mathrm{l-x}}(\mathrm{T}_\mathrm{g})$ at the glass transition can be used as a tool for determination of the thermodynamic fragility, where a larger jump in specific heat capacity at glass transition indicates a more rapid increase of configurational entropy in the liquid upon cooling and a more thermodynamically fragile behavior. Afterwards, by using [191]

$$m = 40\,\frac{\Delta \mathrm{C}_{\mathrm{p}}^{\mathrm{l-x}}(\mathrm{T_g})}{\Delta \mathrm{S_m}} \qquad \textbf{(7-1)},$$

relation for thermodynamic fragility being related to the kinetic fragility, D^* , through [192]

$$m = 17 + \frac{590}{\mathrm{D}^*} \qquad \textbf{(7-2)},$$

D^*can be approximated.

Figure 7-5 depicts the developments in the reversed isobaric specific heat capacity between liquid and crystal $\Delta \mathrm{C}_{\mathrm{p}}^{\mathrm{l-x}}(\mathrm{T_g})$ as a function of composition (Pd content) together with the approximated fragility parameter D^*. As can be seen, D^* and $1/\Delta c_p^{l-x}(T_g)$ show the same trend for all the compositions, as the decrease in $\Delta c_p^{l-x}(T_g)$ (increase in $1/\Delta c_p^{l-x}(T_g)$) translates into a higher fragility parameter (D^*).

For the three better glass forming compositions, $Pd_{31}Ni_{42}S_{27}$, $Pd_{33.5}Ni_{40.5}S_{26}$, and $Pd_{37}Ni_{37}S_{26}$ the estimated D^* is in the same range from 6.5 to 7.5, indicating their comparable behavior, while $Pd_{23.9}Ni_{46.9}S_{29.2}$ and $Pd_{45.06}Ni_{33.88}S_{21.06}$ show a more fragile behavior with a D^* of 5.5 and 4 respectively. However, overall, the low D^*range observed in Pd-Ni-S variations suggests a rather fragile kinetic behavior, as D^* values of bulk glass-forming liquids typically range from 10 to 26 [1,54,141,160,175], where a higher D^* value signifies a higher viscosity at the melting point, which leads to a higher glass-forming ability (GFA). Considering the large crystallization driving force and the fragile liquid behavior observed in these compositions, the improbable formation of bulk glass with a critical diameter (d_c) of at least 1 mm in the Pd-Ni-S system is noteworthy. Therefore, the glass-forming ability (GFA) in this system can be attributed to a high interfacial energy between the liquid and crystalline phases, which results in a significant decrease in the nucleation rate, similar to the case observed in Pt-P based liquids [193]. This aspect will be further investigated in the following section.

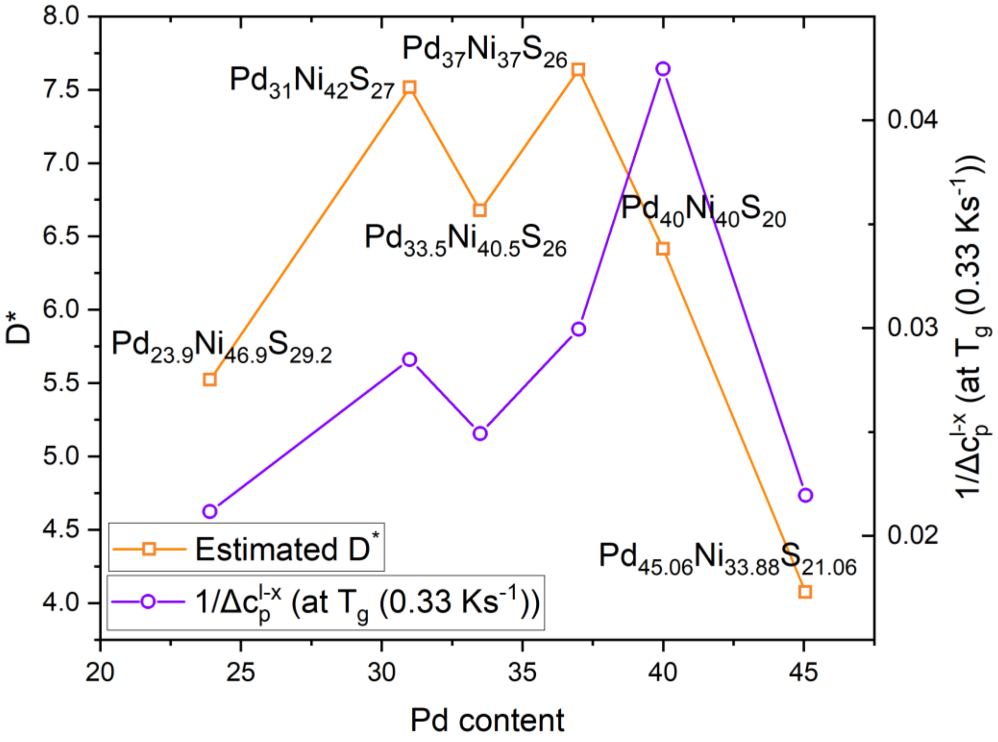

Figure 7-5. Changes in $1/\Delta C_p^{l-x}(T_g)$ as a function of composition (Pd content) together with the approximated kinetic fragility parameter D^* plotted for all Pd-Ni-S alloy variations.

7.3 Interfacial energy calculation

Besides the driving force and viscosity, another critical factor influencing crystallization kinetics is the energy barrier that must be overcome to form a stable nucleus, which can grow into a crystal. For a spherical nucleus in classical nucleation theory, the nucleation barrier, ΔG^*, is defined through Eq. (2-19) in which $\Delta G^*(T) \sim \gamma_{l-x}^3 / \Delta G(T)_{l-x}^2$, with γ_{l-x} being the interfacial energy between liquid and crystal, and ΔG_{l-x} the excess Gibbs free energy. Based on this relation, high interfacial energy also promotes glass formation by raising the nucleation barrier in addition to a low driving force.

The interfacial energy between the nucleating crystal and liquid can be approximated as a fitting parameter within the Johnson-Mehl-Avrami-Kolmogorov (JMAK) equation (Eq. (2-24)).

Table 7-1. JMAK parameters acquired by the fitting procedure.

	Derived from JMAK Fit with crystalline mixture driving force			**Derived from JMAK Fit with Ni_3S_2 driving force**		
Composition	$t_x^*(s)$	$\gamma\ (J/m^2)$	$A_v(Pa/m^3)$	$t_x^*(s)$	$\gamma\ (J/m^2)$	$A_v(Pa/m^3)$
$Pd_{31}Ni_{42}S_{27}$	0.0037	0.11143	7.30797×10^{40}	0.0037	0.13171	8.36239×10^{34}
$Pd_{33.5}Ni_{40.5}S_{26}$	0.0102	0.11025	4.64923×10^{37}	0.0095	0.10553	7.75793×10^{29}
$Pd_{37}Ni_{37}S_{26}$	0.0108	0.1145	1.23126×10^{42}	0.00982	0.0982	1.21742×10^{31}

Given the similar fragilities of $Pd_{31}Ni_{42}S_{27}$, $Pd_{33.5}Ni_{40.5}S_{26}$, and $Pd_{37}Ni_{37}S_{26}$, discussed in section 7.2, and due to the lack of viscosity data for $Pd_{33.5}Ni_{40.5}S_{26}$, and $Pd_{37}Ni_{37}S_{26}$, the derived parameters from the VFT fit by Kuball et al. [42] for the best glass-forming composition, $Pd_{31}Ni_{42}S_{27}$, were used to describe the kinetics of all three compositions in the JMAK fitting procedure.

In Figure 6-9, the experimentally determined times, at which 1% of the sample has isothermally crystallized (circles) in the accessible experimental temperature range, in addition to two fits of the data with the JMAK equation (Eq. 2-24) for all three compositions are shown. One fit uses the calculated Gibbs free energy difference between the supercooled liquid and the crystalline mixture from Eq. (2-2) (dark blue curves) and the other fit (crimson curves) utilizes the calculated driving force from CALPHAD modeling for the primary phase as shown in Figure 7-3. The approximated interfacial energies through both fitting approaches and the minimum crystallization time driven from the fitted curve, the so-called nose time $t_x^*(s)$, are summarized in Table 7-1. The JMAK fitting, employing the calculated driving force from CALPHAD modeling, exhibits more or less the same fit for these compositions, showing a slightly better match to the experimental data at the nose of the crystallization. This slight improvement in the fit can be attributed to considering the actual driving force associated with the initial phase formation (Ni_3S_2), thereby aligning more accurately with the experimental data. Nevertheless, the obtained results suggest that the earlier approach, which involved considering the Gibbs free energy of the crystalline mixture, estimates an interfacial energy value very close to the interfacial energy value obtained when using the driving force from the CALPHAD calculations. The reason is, that for all three compositions close to the eutectic, the driving forces for all crystalline phases are very similar slightly below their melting point (Figure 7-3), so they all crystallize virtually simultaneously (Figure 6-8).

However, in the case of off-eutectic compositions, CALPHAD calculations' role becomes more crucial. As one moves away from the eutectic point, the driving force for primary crystallization increases, and the disparity between the experimentally determined Gibbs free energy difference between the supercooled liquid and the crystalline mixture and the actual (CALPHAD) driving force increases, which impacts the estimation of the interfacial energy significantly. This is the case in Figure 7-3 (a) for the $Pd_{23.9}Ni_{46.9}S_{29.2}$. This plot clearly shows that the actual driving force for the formation of the Ni_3S_2 phase is much larger than the estimation from the crystalline mixture and by approaching the eutectic point the disparity decreases.

For all three compositions presented in Table 7-1, the estimated interfacial energy values, derived using the driving force of crystalline mixture, are quite similar. This similarity is not surprising, since the driving forces of the crystalline mixture are also closely aligned (Figure 7-1 (a)), and that the measured TTT diagrams are very similar resulting in close interfacial energies derived as a fitting parameter. However, the interfacial free energy at the solid-liquid interface very much depends on the local orders in the liquid and solid, along with the thermodynamics. For the three liquid compositions in question, the crystalline phase that nucleates first is the same (Ni_3S_2), but the composition difference across the interface between the liquid and the crystal that forms first, is different. This is why in reality interfacial energy should be different. Therefore, when we use CALPHAD driving forces, the resulting fitted interfacial energies should be closer to the real value, which unfortunately cannot be determined experimentally. These real interfacial energies show a slight variation in concentration indicating that the composition difference between liquid and primary crystal cannot be neglected.

At the liquidus temperature, the solid and liquid phases are in equilibrium, where the high enthalpy of the liquid is balanced by its high entropy, leading to equal free energy for both liquid and solid phases. However, at the interface, this balance is disrupted, resulting in an excess free energy, denoted as γ_{sl}. The origin of γ_{sl} has been shown schematically in Figure 7-6. Hence, by the formation of a solid sphere, the solidified sphere and liquid must then have the same free energy. From Gibbs- Thomson effect (see Figure 7-7), $\Delta \mathrm{G}_v = 2\gamma_{sl}/r^*$, where r^* is the radius of the solid sphere in (unstable) equilibrium with the surrounding liquid and $\Delta \mathrm{G}_v$ is the free energy difference of solid and liquid per unit volume, a solid sphere of radius r will have a free energy greater than that of the stable bulk solid by $2\gamma/r$ per unit volume, and therefore for the nucleation of a specific solid phase with a critical r^*, the Gibbs energy difference between the crystal and liquid, is directly related to the interfacial energy at the interface and varies accordingly [62].

These estimated interfacial energy values are comparable to those determined for Pt-based metallic glasses [193,194], which are considerably higher compared to other glass-forming systems like Zr-based systems [39,195], compensating for the large driving force and the fragile liquid behavior of these glass-forming liquids [193].

Regarding the minimum crystallization time determined at the nose of TTT diagram, $t_x^*(s)$, using the empirical equation relating the crystallization nose time $t_x^*(s)$ to the critical casting diameter d_c (mm) developed by Johnson et al. [65] (Eq. (2-26)), results in a d_c of approximately 1.4 mm for $Pd_{33.5}Ni_{40.5}S_{26}$ and $Pd_{37}Ni_{37}S_{26}$ and 0.95 mm for $Pd_{31}Ni_{42}S_{27}$, which is in good agreement with the experimentally determined d_c of 2 mm and 1.5 mm for $Pd_{37}Ni_{37}S_{26}$ and $Pd_{31}Ni_{42}S_{27}$ compositions, respectively [18].

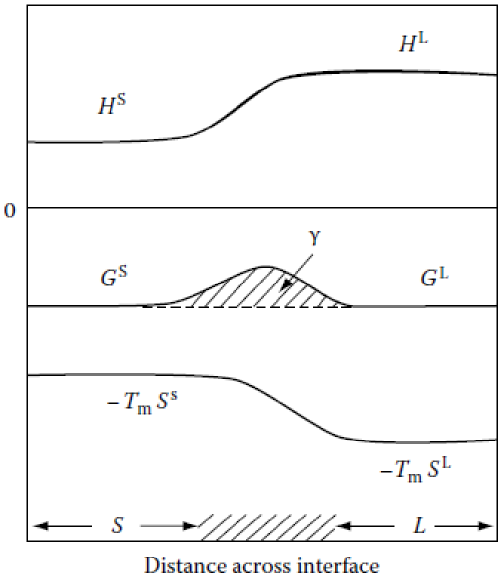

Figure 7-6. Schematic changes of $H - T_m S$ and G across the solid/liquid interface at the equilibrium melting temperature, which shows the origin of the solid/liquid interfacial energy γ_{sl}. Taken from [62].

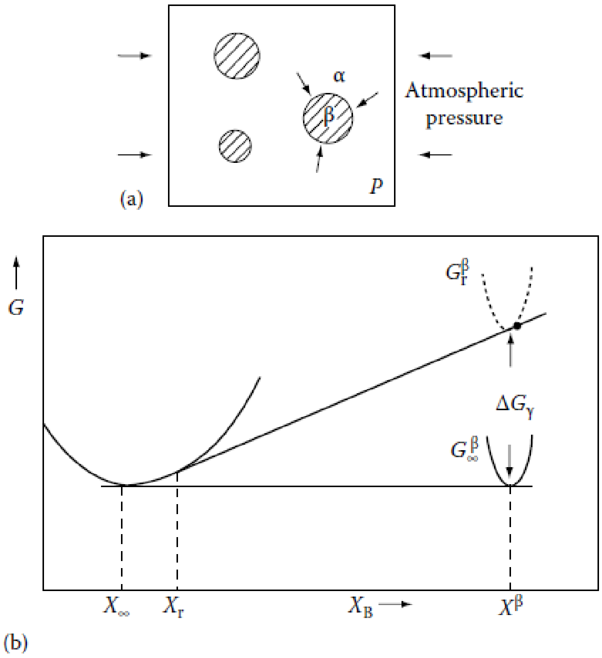

Figure 7-7. Schematic illustration depicting the effect of interfacial energy on the solubility of small particles. Taken from [62].

8 Summary and Conclusion

In this work, a comprehensive experimental and computational investigation into the thermo-physical properties of the novel ternary BMG-forming Pd-Ni-S system was conducted. This system was chosen due to its relative simplicity regarding equilibrium thermodynamics in comparison to other ternary glass forming systems and the extensive experimental data on equilibrium phases available in the literature, which facilitates the application of the CALPHAD approach for the modeling of the underlying thermodynamics affecting the glass formation.

The modeling of the (undercooled) liquid and glass for the pure elements was done using the two-state liquid model and third-generation database. Further, the model was extended to the corresponding Pd-S, Ni-S, and Pd-Ni binary and Pd-Ni-S ternary system, where the modeled results were compared with experimental data and optimized accordingly.

Our experimental investigations consisted of applying methods such as Differential Scanning Calorimetry (DSC), Differential Thermal Analysis (DTA), and Flash-DSC (chip-calorimetry). Additionally, primary phase formation studies using high-energy synchrotron diffraction experiments (HEXRD) under aero-dynamic levitation were conducted to compare and validate CALPHAD modeling.

Using the parallel tangent method for Gibbs free energy in both crystalline and liquid phases, the actual driving force for crystallization of the possible phases (Ni_3S_2, Pd_4S, and (Pd, Ni) solid solution) within the Pd-Ni-S alloy variations was calculated. This method provided a more precise estimation of the nucleation driving force for the initial phase compared to traditional thermodynamic approaches. The calculated driving forces were then used to model isothermal Time-Temperature-Transformation (TTT) diagrams.

The JMAK fitting of the 1% crystallization times in the TTT diagrams, using the driving forces derived from CALPHAD modeling, exhibited a comparable fit to the fits using the crystalline mixture driving force across various compositions, showing a slight improvement in alignment with experimental data at the crystallization nose, which can be attributed to the use of the accurate driving force for the formation of Ni_3S_2.

For compositions close to the eutectic point, namely $Pd_{31}Ni_{42}S_{27}$, $Pd_{33.5}Ni_{40.5}S_{26}$, and $Pd_{37}Ni_{37}S_{26}$, the driving forces for all crystalline phases right below the liquidus temperature were found to be nearly identical, causing them to crystallize almost simultaneously. However, the importance of CALPHAD calculations is remarkable for compositions far from the eutectic point. As compositions diverge from the eutectic, the driving force for primary crystallization increases, leading to a larger discrepancy between the experimentally determined Gibbs free energy difference between the liquid and the crystalline mixture and the actual CALPHAD driving force.

This significantly impacts the interfacial energy estimation. The estimated interfacial energy values for all three compositions, derived from the crystalline mixture driving force, were quite similar due to the closely aligned driving forces. When using CALPHAD driving forces, the values showed a slight decline, reflecting the decrease in Ni_3S_2 driving forces as the eutectic point was approached. Both sets of calculated interfacial energies were very close, indicating the good accuracy of our experimental method for near eutectic compositions, which considered the Gibbs free energy of the crystalline mixture. These calculated considerably large interfacial energies are capable of offsetting the large driving force and fragile liquid behavior of Pd-Ni-S glass-forming liquids, enabling them to form bulk metallic glasses with a critical diameter (d_c) of at least 1 mm.

In conclusion, our experimental approach remains a valuable tool for understanding and predicting the thermodynamics of glass-forming systems, particularly near eutectic compositions. Furthermore, our CALPHAD approach offers a new and accurate means of calculating the driving force for the crystallization of the primary phase, which is critical for assessing glass-forming ability. These findings highlight the interplay of thermodynamic principles, compositional factors, and advanced modeling techniques in the study of metallic glass formation.

9 References

[1] I. Gallino, J. Schroers, R. Busch, Kinetic and thermodynamic studies of the fragility of bulk metallic glass forming liquids, J. Appl. Phys. 108 (2010) 1–8. https://doi.org/10.1063/1.3480805.

[2] V.M. Pacheco Gimon, Optimization and characterization of a novel Pd Ni based bulk metallic glass forming alloy, Universität des Saarlandes, 2016.

[3] O. Gross, Precious metal based bulk glass-forming liquids: Development, thermodynamics, kinetiks and structure, (2018). https://doi.org/http://dx.doi.org/10.22028/D291-27993.

[4] W. KLEMENT, R.H. WILLENS, P.O.L. DUWEZ, Non-crystalline Structure in Solidified Gold–Silicon Alloys, Nature 187 (1960) 869–870. https://doi.org/10.1038/187869b0.

[5] X.H. Lin, W.L. Johnson, Formation of Ti–Zr–Cu–Ni bulk metallic glasses, J. Appl. Phys. 78 (1995) 6514–6519. https://doi.org/10.1063/1.360537.

[6] C. Suryanarayana, A. Inoue, Iron-based bulk metallic glasses, Int. Mater. Rev. 58 (2013) 131–166. https://doi.org/10.1179/1743280412Y.0000000007.

[7] X. Wang, I. Yoshii, A. Inoue, Y.-H. Kim, I.-B. Kim, Bulk Amorphous Ni75−xNb5MxP20−yBy (M=Cr, Mo) Alloys with Large Supercooling and High Strength, Mater. Trans. JIM 40 (1999) 1130–1136. https://doi.org/10.2320/matertrans1989.40.1130.

[8] A.J. Drehman, A.L. Greer, D. Turnbull, Bulk formation of a metallic glass: Pd40Ni40P20, Appl. Phys. Lett. 41 (1982) 716–717. https://doi.org/10.1063/1.93645.

[9] Y.C. Kim, W.T. Kim, D.H. Kim, A development of Ti-based bulk metallic glass, Mater. Sci. Eng. A 375–377 (2004) 127–135. https://doi.org/https://doi.org/10.1016/j.msea.2003.10.115.

[10] A. Peker, W.L. Johnson, A highly processable metallic glass: Zr41.2Ti13.8Cu12.5Ni10.0Be22.5, Appl. Phys. Lett. 63 (1993) 2342–2344. https://doi.org/10.1063/1.110520.

[11] P.J. Spencer, The origins, growth and current industrial impact of Calphad, Calphad Comput. Coupling Phase Diagrams Thermochem. 79 (2022) 102489. https://doi.org/10.1016/j.calphad.2022.102489.

[12] M. Palumbo, L. Battezzati, Thermodynamics and kinetics of metallic amorphous phases in the framework of the CALPHAD approach, Calphad Comput. Coupling Phase Diagrams Thermochem. 32 (2008) 295–314. https://doi.org/10.1016/j.calphad.2007.12.002.

[13] M. Palumbo, G. Cacciamani, E. Bosco, M. Baricco, Thermodynamic analysis of glass formation in Fe-B system, Calphad 25 (2001) 625–637. https://doi.org/https://doi.org/10.1016/S0364-5916(02)00012-3.

[14] R. Bormann, F. Gärtner, K. Zöltzer, Application of the CALPHAD method for the prediction of amorphous phase formation, J. Less Common Met. 145 (1988) 19–29. https://doi.org/10.1016/0022-5088(88)90258-5.

[15] R.B. Schwarz, P. Nash, D. Turnbull, The use of thermodynamic models in the prediction of the glass-forming range of binary alloys, J. Mater. Res. 2 (1987) 456–460. https://doi.org/10.1557/JMR.1987.0456.

[16] S. Bigdeli, H. Mao, M. Selleby, On the third-generation Calphad databases: An updated description of Mn, Phys. Status Solidi 252 (2015) 2199–2208. https://doi.org/https://doi.org/10.1002/pssb.201552203.

[17] J. Agren, B. Cheynet, M.T. Clavaguera-Mora, K. Hack, J. Hertz, F. Sommer, U. Kattner, THERMODYNAMIC MODELS AND DATA FOR PURE ELEMENTS AND OTHER ENDMEMBERS OF SOLUTIONS: Group 2 Extrapoliation of the Heat Capacity in Liquid and Amorphous Phases, Calphad 19 (1995) 449–480. https://drive.google.com/open?id=0BwDenrliobpfSkhZTXBEWjgzckk.

[18] A. Kuball, B. Bochtler, O. Gross, V. Pacheco, M. Stolpe, S. Hechler, R. Busch, On the bulk glass formation in the ternary Pd-Ni-S system, Acta Mater. 158 (2018) 13–22. https://doi.org/10.1016/j.actamat.2018.07.039.

[19] S. Karup-Moller, E. Makovicky, The system Pd-Ni-S at 900 degrees , 725 degrees , 550 degrees , and 400 degrees C, Econ. Geol. 88 (1993) 1261–1268. https://doi.org/10.2113/gsecongeo.88.5.1261.

[20] A. Inoue, T. Zhang, T. Masumoto, Glass-forming ability of alloys, J. Non. Cryst. Solids 156–158 (1993) 473–480. https://doi.org/https://doi.org/10.1016/0022-3093(93)90003-G.

[21] A. Inoue, Stabilization of metallic supercooled liquid and bulk amorphous alloys, Acta Mater. 48 (2000) 279–306. https://doi.org/https://doi.org/10.1016/S1359-6454(99)00300-6.

[22] A. Inoue, N. Nishiyama, H. Kimura, Preparation and Thermal Stability of Bulk Amorphous Pd40Cu30Ni10P20 Alloy Cylinder of 72 mm in Diameter, Mater. Trans. JIM

38 (1997) 179–183. https://doi.org/10.2320/matertrans1989.38.179.

[23] J.F. Löffler, Bulk metallic glasses, Intermetallics 11 (2003) 529–540. https://doi.org/https://doi.org/10.1016/S0966-9795(03)00046-3.

[24] A.L. Greer, Confusion by design, Nature 366 (1993) 303–304. https://doi.org/10.1038/366303a0.

[25] K. Russew, L. Stojanova, Glassy Metals, Glas. Met. (2016) 1–262. https://doi.org/10.1007/978-3-662-47882-0.

[26] Z.P. Lu, Y. Li, S.C. Ng, Reduced glass transition temperature and glass forming ability of bulk glass forming alloys, J. Non. Cryst. Solids 270 (2000) 103–114. https://doi.org/https://doi.org/10.1016/S0022-3093(00)00064-8.

[27] C.A. Angell, Glass-Formers and Viscous Liquid Slowdown since David Turnbull: Enduring Puzzles and New Twists Introduction: The Two Major Branches of the "Glass Problem," 33 (2008). www.mrs.org/bulletin.

[28] G. Jaeger, The Ehrenfest Classification of Phase Transitions: Introduction and Evolution, Arch. Hist. Exact Sci. 53 (1998) 51–81. https://doi.org/10.1007/s004070050021.

[29] J. Ågren, On the classification of phase transformations, Scr. Mater. 46 (2002) 893–898. https://doi.org/10.1016/S1359-6462(02)00083-0.

[30] C.A. Angell, The glass transition, Curr. Opin. Solid State Mater. Sci. 1 (1996) 578–585. https://doi.org/10.1016/S1359-0286(96)80076-3.

[31] M. J.R. Hoch, Statistical and Thermal Physics: An Introduction, 2nd ed., CRC Press, 2021. https://doi.org/https://doi.org/10.1201/9781003028604.

[32] M.H. Cohen, G.S. Grest, Liquid-glass transition, a free-volume approach, Phys. Rev. B 20 (1979) 1077–1098. https://doi.org/10.1103/PhysRevB.20.1077.

[33] W. Kauzmann, The Nature of the Glassy State and the Behavior of Liquids at Low Temperatures., Chem. Rev. 43 (1948) 219–256. https://doi.org/10.1021/cr60135a002.

[34] H.S. Chen, D. Turnbull, The specific heat of tin and gallium in their stable and undercooled pure liquid states, Acta Metall. 16 (1968) 369–373. https://doi.org/https://doi.org/10.1016/0001-6160(68)90023-0.

[35] R. Busch, Y.J. Kim, W.L. Johnson, Thermodynamics and kinetics of the undercooled liquid and the glass transition of the Zr41.2Ti13.8Cu12.5Ni10.0Be22.5 alloy, J. Appl. Phys. 77 (1995) 4039–4043. https://doi.org/10.1063/1.359485.

[36] R. Fox, The Background to the Discovery of Dulong and Petit's Law, Br. J. Hist. Sci. 4

(1968) 1–22. https://doi.org/DOI: 10.1017/S0007087400003150.

[37] D. Turnbull, Formation of Crystal Nuclei in Liquid Metals, J. Appl. Phys. 21 (1950) 1022–1028. https://doi.org/10.1063/1.1699435.

[38] A. Inoue, High Strength Bulk Amorphous Alloys with Low Critical Cooling Rates (<I>Overview</I>), Mater. Trans. JIM 36 (1995) 866–875. https://doi.org/10.2320/matertrans1989.36.866.

[39] Y.T. Shen, T.H. Kim, A.K. Gangopadhyay, K.F. Kelton, Icosahedral order, frustration, and the glass transition: Evidence from time-dependent nucleation and supercooled liquid structure studies, Phys. Rev. Lett. 102 (2009) 6–9. https://doi.org/10.1103/PhysRevLett.102.057801.

[40] R. Busch, W. Liu, W.L. Johnson, Thermodynamics and kinetics of the Mg65Cu25Y10 bulk metallic glass forming liquid, J. Appl. Phys. 83 (1998) 4134–4141. https://doi.org/10.1063/1.367167.

[41] W.H. Wang, C. Dong, C.H. Shek, Bulk metallic glasses, Mater. Sci. Eng. R Reports 44 (2004) 45–89. https://doi.org/10.1016/j.mser.2004.03.001.

[42] A. Kuball, Development, Characterization and Processing of a novel Family of Bulk Metallic Glasses: Sulfur-containing Bulk Metallic Glasses, Saarland University, 2019. https://doi.org/10.22028/D291-30889.

[43] K.F. Kelton, A.L. Greer, Nucleation in condensed matter : applications in materials and biology, Elsevier, 2010.

[44] U. Geyer, W.L. Johnson, S. Schneider, Y. Qiu, T.A. Tombrello, M. -P. Macht, Small atom diffusion and breakdown of the Stokes–Einstein relation in the supercooled liquid state of the Zr46.7Ti8.3Cu7.5Ni10Be27.5 alloy, Appl. Phys. Lett. 69 (1996) 2492–2494. https://doi.org/10.1063/1.117716.

[45] R. Pastore, T. Kikutsuji, F. Rusciano, N. Matubayasi, K. Kim, F. Greco, Breakdown of the Stokes–Einstein relation in supercooled liquids: A cage-jump perspective, J. Chem. Phys. 155 (2021) 114503. https://doi.org/10.1063/5.0059622.

[46] M.D. Ediger, P. Harrowell, L. Yu, Crystal growth kinetics exhibit a fragility-dependent decoupling from viscosity, J. Chem. Phys. 128 (2008) 34709. https://doi.org/10.1063/1.2815325.

[47] L.-M. Wang, V. Velikov, C.A. Angell, Direct determination of kinetic fragility indices of glassforming liquids by differential scanning calorimetry: Kinetic versus thermodynamic fragilities, J. Chem. Phys. 117 (2002) 10184–10192. https://doi.org/10.1063/1.1517607.

[48] C.A. Angell, Formation of Glasses from Liquids and Biopolymers, Science (80-.). 267 (1995) 1924–1935. https://doi.org/10.1126/science.267.5206.1924.

[49] H. Eyring, Viscosity, Plasticity, and Diffusion as Examples of Absolute Reaction Rates, J. Chem. Phys. 4 (1936) 283–291. https://doi.org/10.1063/1.1749836.

[50] H. Tanaka, Relation between thermodynamics and kinetics of glass-forming liquids, Phys Rev Lett 90 (2003) 055701. https://doi.org/10.1103/PhysRevLett.90.055701.

[51] Z. Evenson, S. Raedersdorf, I. Gallino, R. Busch, Equilibrium viscosity of Zr–Cu–Ni–Al–Nb bulk metallic glasses, Scr. Mater. 63 (2010) 573–576. https://doi.org/https://doi.org/10.1016/j.scriptamat.2010.06.008.

[52] J.H. Na, M.D. Demetriou, M. Floyd, A. Hoff, G.R. Garrett, W.L. Johnson, Compositional landscape for glass formation in metal alloys, Proc. Natl. Acad. Sci. 111 (2014) 9031–9036. https://doi.org/10.1073/pnas.1407780111.

[53] J. Hyun Na, M.D. Demetriou, W.L. Johnson, Fragility of iron-based glasses, Appl. Phys. Lett. 99 (2011) 161902. https://doi.org/10.1063/1.3651763.

[54] O. Gross, B. Bochtler, M. Stolpe, S. Hechler, W. Hembree, R. Busch, I. Gallino, The kinetic fragility of Pt-P- and Ni-P-based bulk glass-forming liquids and its thermodynamic and structural signature, Acta Mater. 132 (2017) 118–127. https://doi.org/10.1016/j.actamat.2017.04.030.

[55] W.L. Johnson, Bulk Glass-Forming Metallic Alloys: Science and Technology, MRS Bull. 24 (1999) 42–56. https://doi.org/10.1557/S0883769400053252.

[56] J.H. Gibbs, G. Adam, On the temperature dependence of cooperative relaxation properties in glass-forming liquids, J. Chem. Phys. 43 (1965) 139–146.

[57] P. G. Debenedetti, Metastable Liquids: Concepts and Principles, Princton University Press, 1997.

[58] L.-M. Martinez, C.A. Angell, C.A. Martinez, L-M. and Angell, A thermodynamic connection to the fragility of glass-forming liquids, Nature 410 (2001) 663–667. https://doi.org/10.1038/35070517.

[59] G.J. Fan, H. Choo, P.K. Liaw, Fragility of metallic glass-forming liquids: A simple thermodynamic connection, J. Non. Cryst. Solids 351 (2005) 3879–3883. https://doi.org/https://doi.org/10.1016/j.jnoncrysol.2005.10.018.

[60] H.L. Smith, C.W. Li, A. Hoff, G.R. Garrett, D.S. Kim, F.C. Yang, M.S. Lucas, T. Swan-Wood, J.Y.Y.Y. Lin, M.B. Stone, D.L. Abernathy, M.D. Demetriou, B. Fultz, Separating the configurational and vibrational entropy contributions in metallic glasses, Nat. Phys. 13

(2017) 900–905. https://doi.org/10.1038/nphys4142.

[61] C.A. Angell, Thermodynamic aspects of the glass transition in liquids and plastic crystals, 63 (1991) 1387–1392. https://doi.org/doi:10.1351/pac199163101387.

[62] D. A. PORTER, K. E. EASTERLING, M. Y. SHERIF, Phase Transformations in Metals and Alloys, 4th ed., CRC Press, 2021. https://doi.org/https://doi.org/10.1201/9781003011804.

[63] D.R. Uhlmann, A kinetic treatment of glass formation, J. Non. Cryst. Solids 7 (1972) 337–348. https://doi.org/https://doi.org/10.1016/0022-3093(72)90269-4.

[64] D.R. Uhlmann, Glass formation, J. Non. Cryst. Solids 25 (1977) 42–85. https://doi.org/https://doi.org/10.1016/0022-3093(77)90090-4.

[65] W.L. Johnson, J.H. Na, M.D. Demetriou, Quantifying the origin of metallic glass formation, Nat. Commun. 7 (2016). https://doi.org/10.1038/ncomms10313.

[66] Y.J. Kim, R. Busch, W.L. Johnson, A.J. Rulison, W.K. Rhim, Metallic glass formation in highly undercooled Zr41.2Ti13.8Cu12.5Ni10.0Be22.5 during containerless electrostatic levitation processing, Appl. Phys. Lett. 65 (1994) 2136–2138. https://doi.org/10.1063/1.112768.

[67] A. Gebert, J. Eckert, L. Schultz, Effect of oxygen on phase formation and thermal stability of slowly cooled Zr65Al7.5Cu17.5Ni10 metallic glass, Acta Mater. 46 (1998) 5475–5482. https://doi.org/https://doi.org/10.1016/S1359-6454(98)00187-6.

[68] X.H. Lin, W.L. Johnson, W.K. Rhim, Effect of Oxygen Impurity on Crystallization of an Undercooled Bulk Glass Forming Zr–Ti–Cu–Ni–Al Alloy, Mater. Trans. JIM 38 (1997) 473–477. https://doi.org/10.2320/matertrans1989.38.473.

[69] Liling Sun, Qi Wu, Yingfan Xu, Wenkui Wang, Study on solidification behaviour of Pd40Ni40P20 alloy by fluxing method, Phys. B Condens. Matter 240 (1997) 205–210. https://doi.org/https://doi.org/10.1016/S0921-4526(97)00425-0.

[70] D. Granata, E. Fischer, V. Wessels, J.F. Löffler, Fluxing of Pd–Si–Cu bulk metallic glass and the role of cooling rate and purification, Acta Mater. 71 (2014) 145–152. https://doi.org/https://doi.org/10.1016/j.actamat.2014.03.008.

[71] M. Müller, Crystallization and Physical Aging Behavior Studies on Bulk Metallic Glass Forming Liquids via Fast Differential Scanning Calorimetry, Universität des Saarlandes, 2022.

[72] J.L. Finney, Modelling the structures of amorphous metals and alloys, Nature 266 (1977) 309–314. https://doi.org/10.1038/266309a0.

[73] G.S. Cargill, Structure of Metallic Alloy Glasses, in: H. Ehrenreich, F. Seitz, D.B.T.-S.S.P. Turnbull (Eds.), Academic Press, 1975: pp. 227–320. https://doi.org/https://doi.org/10.1016/S0081-1947(08)60337-9.

[74] J.D. BERNAL, A Geometrical Approach to the Structure Of Liquids, Nature 183 (1959) 141–147. https://doi.org/10.1038/183141a0.

[75] J.D. BERNAL, J. MASON, Packing of Spheres: Co-ordination of Randomly Packed Spheres, Nature 188 (1960) 910–911. https://doi.org/10.1038/188910a0.

[76] J.D. BERNAL, Geometry of the Structure of Monatomic Liquids, Nature 185 (1960) 68–70. https://doi.org/10.1038/185068a0.

[77] P.H. GASKELL, A new structural model for transition metal–metalloid glasses, Nature 276 (1978) 484–485. https://doi.org/10.1038/276484a0.

[78] T. Egami, S. J. L. Billinge, S. J.L. Billinge, T. Egami, S. J. L. Billinge, Underneath the Bragg Peaks, 1st ed., Elsevier Ltd, 2003.

[79] A. Hirata, L.J. Kang, T. Fujita, B. Klumov, K. Matsue, M. Kotani, A.R. Yavari, M.W. Chen, Geometric Frustration of Icosahedron in Metallic Glasses, Science (80-.). 341 (2013) 376–379. https://doi.org/10.1126/science.1232450.

[80] Y.Q. Cheng, E. Ma, Atomic-level structure and structure–property relationship in metallic glasses, Prog. Mater. Sci. 56 (2011) 379–473. https://doi.org/https://doi.org/10.1016/j.pmatsci.2010.12.002.

[81] T. Egami, S. Aur, Local atomic structure of amorphous and crystalline alloys: Computer simulation, J. Non. Cryst. Solids 89 (1987) 60–74. https://doi.org/https://doi.org/10.1016/S0022-3093(87)80321-6.

[82] H.W. Sheng, W.K. Luo, F.M. Alamgir, J.M. Bai, E. Ma, Atomic packing and short-to-medium-range order in metallic glasses, Nature 439 (2006) 419–425. https://doi.org/10.1038/nature04421.

[83] D.B. Miracle, A structural model for metallic glasses, Nat. Mater. 3 (2004) 697–702. https://doi.org/10.1038/nmat1219.

[84] D.B. Miracle, The efficient cluster packing model – An atomic structural model for metallic glasses, Acta Mater. 54 (2006) 4317–4336. https://doi.org/https://doi.org/10.1016/j.actamat.2006.06.002.

[85] J. Ding, E. Ma, M. Asta, R.O. Ritchie, Second-Nearest-Neighbor Correlations from Connection of Atomic Packing Motifs in Metallic Glasses and Liquids, Sci. Rep. 5 (2015) 17429. https://doi.org/10.1038/srep17429.

[86] O. Gross, N. Neuber, A. Kuball, B. Bochtler, S. Hechler, M. Frey, R. Busch, Signatures of structural differences in Pt–P- and Pd–P-based bulk glass-forming liquids, Commun. Phys. 2 (2019) 1–8. https://doi.org/10.1038/s42005-019-0180-2.

[87] L. Kaufman, H. Bernstein, Computer calculation of phase diagrams With special reference to refractory metals, Academic Press Inc, United States, 1970. http://inis.iaea.org/search/search.aspx?orig_q=RN:02004171.

[88] P.J. Spencer, A brief history of CALPHAD, Calphad 32 (2008) 1–8. https://doi.org/https://doi.org/10.1016/j.calphad.2007.10.001.

[89] A.T. Dinsdale, SGTE data for pure elements, Calphad 15 (1991) 317–425. https://doi.org/https://doi.org/10.1016/0364-5916(91)90030-N.

[90] U.R. Kattner, the Calphad Method and Its Role in Material and Process Development, Tecnol. Em Metal. Mater. e Mineração 13 (2016) 3–15. https://doi.org/10.4322/2176-1523.1059.

[91] N.R. Council, Integrated Computational Materials Engineering: A Transformational Discipline for Improved Competitiveness and National Security, The National Academies Press, Washington, DC, 2008. https://doi.org/10.17226/12199.

[92] C. Ward, Materials Genome Initiative for Global Competitiveness, 2012.

[93] J. Ågren, The materials genome and CALPHAD, Chinese Sci. Bull. 59 (2014) 1635–1640. https://doi.org/10.1007/s11434-013-0108-2.

[94] L. Kaufman, J. Ågren, CALPHAD, first and second generation – Birth of the materials genome, Scr. Mater. 70 (2014) 3–6. https://doi.org/https://doi.org/10.1016/j.scriptamat.2012.12.003.

[95] G.B. Olson, Preface to the viewpoint set on: The Materials Genome, Scr. Mater. 70 (2014) 1–2. https://doi.org/https://doi.org/10.1016/j.scriptamat.2013.09.013.

[96] P. Benigni, CALPHAD modeling of the glass transition for a pure substance, coupling thermodynamics and relaxation kinetics, Calphad Comput. Coupling Phase Diagrams Thermochem. 72 (2021) 102238. https://doi.org/10.1016/j.calphad.2020.102238.

[97] Z. Li, S. Bigdeli, H. Mao, Q. Chen, M. Selleby, Thermodynamic evaluation of pure Co for the third generation of thermodynamic databases, Phys. Status Solidi Basic Res. 254 (2017). https://doi.org/10.1002/pssb.201600231.

[98] E.D. Alvares, W.J. Botta, J. Ågren, A. Costa e Silva, An assessment of Fe-Nb-B melts using the two-state liquid model, Calphad Comput. Coupling Phase Diagrams Thermochem. 68 (2020) 101692. https://doi.org/10.1016/j.calphad.2019.101692.

[99] S. Bigdeli, Q. Chen, M. Selleby, A New Description of Pure C in Developing the Third Generation of Calphad Databases, J. Phase Equilibria Diffus. 39 (2018) 832–840. https://doi.org/10.1007/s11669-018-0679-3.

[100] J. Agren, Thermodynamics of Supercooled Liquids and their Glass Transition, Phys. Chem. Liq. 18 (1988) 123–139. https://doi.org/10.1080/00319108808078586.

[101] Workshop on thermodynamic models and data for pure elements and other endmembers of solutions: Schloβ Ringberg, Febr. 21, to March 3, 1995, Calphad 19 (1995) 449–480. https://doi.org/https://doi.org/10.1016/0364-5916(96)00003-X.

[102] C.A. Becker, J. Ågren, M. Baricco, Q. Chen, S.A. Decterov, U.R. Kattner, J.H. Perepezko, G.R. Pottlacher, M. Selleby, Thermodynamic modelling of liquids: CALPHAD approaches and contributions from statistical physics, Phys. Status Solidi 251 (2014) 33–52. https://doi.org/https://doi.org/10.1002/pssb.201350149.

[103] Q. Chen, B. Sundman, Modeling of thermodynamic properties for Bcc, Fcc, liquid, and amorphous iron, J. Phase Equilibria 22 (2001) 631–644. https://doi.org/10.1007/s11669-001-0027-9.

[104] A. V Khvan, A.T. Dinsdale, I.A. Uspenskaya, M. Zhilin, T. Babkina, A.M. Phiri, A thermodynamic description of data for pure Pb from 0K using the expanded Einstein model for the solid and the two state model for the liquid phase, Calphad 60 (2018) 144–155. https://doi.org/https://doi.org/10.1016/j.calphad.2017.12.008.

[105] A. V Khvan, T. Babkina, A.T. Dinsdale, I.A. Uspenskaya, I. V Fartushna, A.I. Druzhinina, A.B. Syzdykova, M.P. Belov, I.A. Abrikosov, Thermodynamic properties of tin: Part I Experimental investigation, ab-initio modelling of α-, β-phase and a thermodynamic description for pure metal in solid and liquid state from 0 K, Calphad 65 (2019) 50–72. https://doi.org/https://doi.org/10.1016/j.calphad.2019.02.003.

[106] O. Tolochko, J. Ågren, Thermodynamic properties of supercooled Fe-B liquids—A theoretical and experimental study, J. Phase Equilibria 21 (2000) 19–24. https://doi.org/10.1361/105497100770340372.

[107] S. Bigdeli, M. Selleby, A thermodynamic assessment of the binary Fe-Mn system for the third generation of Calphad databases, Calphad 64 (2019) 185–195. https://doi.org/https://doi.org/10.1016/j.calphad.2018.11.011.

[108] P. Benigni, Interest of the regular 2-state model for the description of unary liquids: Presentation of the formalism, Calphad 83 (2023) 102627. https://doi.org/https://doi.org/10.1016/j.calphad.2023.102627.

[109] C.A. Angell, K.J. Rao, Configurational Excitations in Condensed Matter, and the ``Bond

Lattice'' Model for the Liquid-Glass Transition, J. Chem. Phys. 57 (1972) 470–481. https://doi.org/10.1063/1.1677987.

[110] M.I. Ojovan, W. (Bill) E. Lee, Connectivity and glass transition in disordered oxide systems, J. Non. Cryst. Solids 356 (2010) 2534–2540. https://doi.org/https://doi.org/10.1016/j.jnoncrysol.2010.05.012.

[111] G.T. Furukawa, W.G. Saba, M.L. Reilly, Critical analysis of the heat-capacity data of the literature and evaluation of thermodynamic properties of copper, silver, and gold from 0 to 300 oK:, (1968). https://doi.org/https://doi.org/10.6028/NBS.NSRDS.18.

[112] R.B. Schwarz, Y. He, Bulk Metallic Glass Formation in the Pd-Ni-P and Pd-Cu-P Alloy Systems BT - Properties of Complex Inorganic Solids, in: A. Gonis, A. Meike, P.E.A. Turchi (Eds.), Springer US, Boston, MA, 1997: pp. 287–299. https://doi.org/10.1007/978-1-4615-5943-6_38.

[113] H.S. Chen, B.K. Park, Role of chemical bonding in metallic glasses, Acta Metall. 21 (1973) 395–400. https://doi.org/https://doi.org/10.1016/0001-6160(73)90196-X.

[114] H. Okamoto, Pd-s (palladium-sulfur), J. Phase Equilibria 13 (1992) 106–107. https://doi.org/10.1007/BF02645396.

[115] H. Okamoto, Ni-S (Nickel-Sulfur), J. Phase Equilibria Diffus. 30 (2009) 123. https://doi.org/10.1007/s11669-008-9430-9.

[116] A. Nash, P. Nash, The Ni−Pd (Nickel-Palladium) system, Bull. Alloy Phase Diagrams 5 (1984) 446–450. https://doi.org/10.1007/BF02872890.

[117] W. Zielenkiewicz, E. Margas, Theory of Calorimetry, 1st ed., Springer Dordrecht, 2002. https://doi.org/https://doi.org/10.1007/0-306-48418-8.

[118] S. Vyazovkin, N. Koga, C. Schick, Handbook of Thermal Analysis and Calorimetry, 6th ed., 2018.

[119] B. Bochtler, Thermophysical and Structural Investigations of a CuTi- and a Zr-based Bulk Metallic Glass, the Influence of Minor Additions, and the Relation to Thermoplastic Forming, Universitt des Saarlandes, 2019.

[120] V.B.F. Mathot, Thermal analysis and calorimetry beyond 2000: challenges and new routes, Thermochim. Acta 355 (2000) 1–33. https://doi.org/https://doi.org/10.1016/S0040-6031(00)00450-0.

[121] V. Mathot, B. Goderis, H. Reynaers, Metastability in polymer systems studied under extreme conditions: High pressure, scan-iso T-t ramps and high scanning rates, Fibres Text. East. Eur. 11 (2003) 20–27.

[122] C. Schick, Differential scanning calorimetry (DSC) of semicrystalline polymers, Anal. Bioanal. Chem. 395 (2009) 1589–1611. https://doi.org/10.1007/s00216-009-3169-y.

[123] J.E.K. Schawe, S. Pogatscher, Material Characterization by Fast Scanning Calorimetry: Practice and Applications BT - Fast Scanning Calorimetry, in: C. Schick, V. Mathot (Eds.), Springer International Publishing, Cham, 2016: pp. 3–80. https://doi.org/10.1007/978-3-319-31329-0_1.

[124] J.E.K. Schawe, Flash DSC 1: A novel fast differential scanning calorimeter, in: 27th World Congr. Polym. Process. Soc., Marrakech, Morocco, 2011.

[125] J.E.K. Schawe, S. Ziegelmeier, Determination of the thermal short time stability of polymers by fast scanning calorimetry, Thermochim. Acta 623 (2016) 80–85. https://doi.org/https://doi.org/10.1016/j.tca.2015.11.020.

[126] J. Orava, A.L. Greer, B. Gholipour, D.W. Hewak, C.E. Smith, Characterization of supercooled liquid Ge2Sb2Te5 and its crystallization by ultrafast-heating calorimetry, Nat. Mater. 11 (2012) 279–283. https://doi.org/10.1038/nmat3275.

[127] J.Q. Wang, N. Chen, P. Liu, Z. Wang, D. V Louzguine-Luzgin, M.W. Chen, J.H. Perepezko, The ultrastable kinetic behavior of an Au-based nanoglass, Acta Mater. 79 (2014) 30–36. https://doi.org/https://doi.org/10.1016/j.actamat.2014.07.015.

[128] S. Pogatscher, P.J. Uggowitzer, J.F. Löffler, In-situ probing of metallic glass formation and crystallization upon heating and cooling via fast differential scanning calorimetry, Appl. Phys. Lett. 104 (2014) 251908. https://doi.org/10.1063/1.4884940.

[129] P.A. Vermeulen, J. Momand, B.J. Kooi, Reversible amorphous-crystalline phase changes in a wide range of Se1−xTex alloys studied using ultrafast differential scanning calorimetry, J. Chem. Phys. 141 (2014) 24502. https://doi.org/10.1063/1.4886185.

[130] J. Schawe, Fast Scanning DSC: Practical tips and information, METTLER TOLEDO (2010) 1–7.

[131] S. Pogatscher, D. Leutenegger, A. Hagmann, P.J. Uggowitzer, J.F. Löffler, Reprint of: Characterization of bulk metallic glasses via fast differential scanning calorimetry, Thermochim. Acta 590 (2014) 46–52. https://doi.org/10.1016/j.tca.2014.12.012.

[132] J.Q. Wang, Y. Shen, J.H. Perepezko, M.D. Ediger, Increasing the kinetic stability of bulk metallic glasses, Acta Mater. 104 (2016) 25–32. https://doi.org/10.1016/j.actamat.2015.11.048.

[133] N. Sohrabi, J.E.K. Schawe, J. Jhabvala, J.F. Löffler, R.E. Logé, Critical crystallization properties of an industrial-grade Zr-based metallic glass used in additive manufacturing,

Scr. Mater. 199 (2021) 113861. https://doi.org/10.1016/j.scriptamat.2021.113861.

[134] J.E.K. Schawe, S. Pogatscher, J.F. Löffler, Thermodynamics of polymorphism in a bulk metallic glass: Heat capacity measurements by fast differential scanning calorimetry, Thermochim. Acta 685 (2020) 178518. https://doi.org/10.1016/j.tca.2020.178518.

[135] C. Schick, V. Mathot, Fast Scanning Calorimetry, 1st ed., Springer Cham, 2018. https://doi.org/https://doi.org/10.1007/978-3-319-31329-0.

[136] J.E.K. Schawe, J.F. Löffler, Existence of multiple critical cooling rates which generate different types of monolithic metallic glass, Nat. Commun. 10 (2019). https://doi.org/10.1038/s41467-018-07930-3.

[137] S. Mukherjee, Z. Zhou, J. Schroers, W.L. Johnson, W.K. Rhim, Overheating threshold and its effect on time-temperature-transformation diagrams of zirconium based bulk metallic glasses, Appl. Phys. Lett. 84 (2004) 5010–5012. https://doi.org/10.1063/1.1763219.

[138] J.K. Lee, D.H. Bae, W.T. Kim, D.H. Kim, Effect of liquid temperature on thermal stability and crystallization behavior of Ni-based amorphous alloys, Mater. Sci. Eng. A 375–377 (2004) 332–335. https://doi.org/10.1016/j.msea.2003.10.103.

[139] J. Mao, H.F. Zhang, H.M. Fu, A.M. Wang, H. Li, Z.Q. Hu, The effects of casting temperature on the glass formation of Zr-based metallic glasses, Adv. Eng. Mater. 11 (2009) 986–991. https://doi.org/10.1002/adem.200900174.

[140] Q. Cheng, Y.H. Sun, J. Orava, W.H. Wang, Homogenization of a metallic melt: Enhancing the thermal stability of glassy metal, Mater. Today Phys. 31 (2023) 101004. https://doi.org/10.1016/j.mtphys.2023.101004.

[141] Z. Evenson, T. Schmitt, M. Nicola, I. Gallino, R. Busch, High temperature melt viscosity and fragile to strong transition in Zr-Cu-Ni-Al-Nb(Ti) and Cu 47Ti 34Zr 11Ni 8 bulk metallic glasses, Acta Mater. 60 (2012) 4712–4719. https://doi.org/10.1016/j.actamat.2012.05.019.

[142] C. Way, P. Wadhwa, R. Busch, The influence of shear rate and temperature on the viscosity and fragility of the Zr41.2Ti13.8Cu12.5Ni10.0Be22.5 metallic-glass-forming liquid, Acta Mater. 55 (2007) 2977–2983. https://doi.org/10.1016/j.actamat.2006.12.032.

[143] W. Xu, M.T. Sandor, Y. Yu, H.B. Ke, H.P. Zhang, M.Z. Li, W.H. Wang, L. Liu, Y. Wu, Evidence of liquid-liquid transition in glass-forming La50Al35Ni15 melt above liquidus temperature, Nat. Commun. 6 (2015). https://doi.org/10.1038/ncomms8696.

[144] D.H. Kim, W.T. Kim, E.S. Park, N. Mattern, J. Eckert, Phase separation in metallic glasses, Prog. Mater. Sci. 58 (2013) 1103–1172.

https://doi.org/10.1016/j.pmatsci.2013.04.002.

[145] P.S. Popel, V.E. Sidorov, Microheterogeneity of liquid metallic solutions and its influence on the structure and properties of rapidly quenched alloys, Mater. Sci. Eng. A 226–228 (1997) 237–244. https://doi.org/10.1016/s0921-5093(96)10624-9.

[146] N. Neuber, M. Frey, O. Gross, J. Baller, I. Gallino, R. Busch, Ultrafast scanning calorimetry of newly developed Au-Ga bulk metallic glasses, J. Phys. Condens. Matter 32 (2020). https://doi.org/10.1088/1361-648X/ab8252.

[147] M. Frey, N. Neuber, M. Müller, O. Gross, S.S. Riegler, I. Gallino, R. Busch, Determining and modelling a complete time-temperature-transformation diagram for a Pt-based metallic glass former through combination of conventional and fast scanning calorimetry, Scr. Mater. 215 (2022) 114710. https://doi.org/10.1016/j.scriptamat.2022.114710.

[148] E. Shoifet, G. Schulz, C. Schick, Temperature modulated differential scanning calorimetry - Extension to high and low frequencies, Thermochim. Acta 603 (2015) 227–236. https://doi.org/10.1016/j.tca.2014.10.010.

[149] X. Monnier, D. Cangialosi, B. Ruta, R. Busch, I. Gallino, Vitrification decoupling from α-relaxation in a metallic glass, Sci. Adv. 6 (2020). https://doi.org/10.1126/sciadv.aay1454.

[150] E. Hempel, G. Hempel, A. Hensel, C. Schick, E. Donth, Characteristic Length of Dynamic Glass Transition near Tg for a Wide Assortment of Glass-Forming Substances, J. Phys. Chem. B 104 (2000) 2460–2466. https://doi.org/10.1021/jp991153f.

[151] N.G. Perez-de-Eulate, V. Di Lisio, D. Cangialos, Glass transition and molecular dynamics in polystyrene nanospheres by fast scanning calorimetry, ACS Macro Lett. 6 (2017) 859–863. https://doi.org/10.1021/acsmacrolett.7b00484.

[152] V. Di Lisio, I. Gallino, S.S. Riegler, M. Frey, N. Neuber, G. Kumar, J. Schroers, R. Busch, D. Cangialosi, Size-dependent vitrification in metallic glasses, Nat. Commun. 14 (2023) 4698. https://doi.org/10.1038/s41467-023-40417-4.

[153] K. Schraut, F. Kargl, C. Adam, O. Ivashko, In situ synchrotron XRD measurements during solidification of a melt in the CaO-SiO2system using an aerodynamic levitation system, J. Phys. Condens. Matter 33 (2021). https://doi.org/10.1088/1361-648X/abf7e1.

[154] K.H. SANDHAGE, G.J. YUREK, Indirect Dissolution of Sapphire into Silicate Melts, J. Am. Ceram. Soc. 71 (1988) 478–489. https://doi.org/https://doi.org/10.1111/j.1151-2916.1988.tb05898.x.

[155] D.J. Malvin, Silica-glass containers for high-temperature experiments, Am. Mineral. 73

(1988) 1198–1200.

[156] W. Rhim, S.K. Chung, D. Barber, K.F. Man, G. Gutt, A. Rulison, R.E. Spjut, An electrostatic levitator for high-temperature containerless materials processing in 1-g, Rev. Sci. Instrum. 64 (1993) 2961–2970. https://doi.org/10.1063/1.1144475.

[157] P.-F. Paradis, T. Ishikawa, S. Yoda, Electrostatic Levitation Research and Development at JAXA: Past and Present Activities in Thermophysics, Int. J. Thermophys. 26 (2005) 1031–1049. https://doi.org/10.1007/s10765-005-6683-y.

[158] N.A. Mauro, K.F. Kelton, A highly modular beamline electrostatic levitation facility, optimized for in situ high-energy x-ray scattering studies of equilibrium and supercooled liquids, Rev. Sci. Instrum. 82 (2011) 35114. https://doi.org/10.1063/1.3554437.

[159] N.A. Mauro, A.J. Vogt, K.S. Derendorf, M.L. Johnson, G.E. Rustan, D.G. Quirinale, A. Kreyssig, K.A. Lokshin, J.C. Neuefeind, K. An, X.-L. Wang, A.I. Goldman, T. Egami, K.F. Kelton, Electrostatic levitation facility optimized for neutron diffraction studies of high temperature liquids at a spallation neutron source, Rev. Sci. Instrum. 87 (2016) 13904. https://doi.org/10.1063/1.4939194.

[160] B. Bochtler, O. Gross, I. Gallino, R. Busch, Thermo-physical characterization of the Fe67Mo6Ni3.5Cr3.5P12C5.5B2.5 bulk metallic glass forming alloy, Acta Mater. 118 (2016) 129–139. https://doi.org/10.1016/j.actamat.2016.07.031.

[161] C.J. Benmore, J.K.R. Weber, Aerodynamic levitation, supercooled liquids and glass formation, Adv. Phys. X 2 (2017) 717–736. https://doi.org/10.1080/23746149.2017.1357498.

[162] L. Hennet, C. Landron, P. Berthet, J.-P. Coutures, T. Jenkins, C. Aletru, N. Greaves, X-Ray Diffraction and Near Edge Studies of Iron Oxides and Alumina at High Temperatures Using Aerodynamic Levitation and Laser Heating, Jpn. J. Appl. Phys. 38 (1999) 115. https://doi.org/10.7567/JJAPS.38S1.115.

[163] O.L.G. Alderman, L.B. Skinner, C.J. Benmore, A. Tamalonis, J.K.R. Weber, Structure of molten titanium dioxide, Phys. Rev. B 90 (2014) 94204. https://doi.org/10.1103/PhysRevB.90.094204.

[164] J. Kozaily, L. Hennet, H.E. Fischer, M. Koza, S. Brassamin, S. Magazù, F. Kargl, Time-of-flight neutron spectroscopy: a new application of aerodynamic sample levitation, Phys. Status Solidi C 8 (2011) 3155–3158. https://doi.org/https://doi.org/10.1002/pssc.201000753.

[165] L. Hennet, I. Pozdnyakova, A. Bytchkov, D.L. Price, G.N. Greaves, M. Wilding, S. Fearn, C.M. Martin, D. Thiaudière, J.-F. Bérar, N. Boudet, M.-L. Saboungi, Development of

structural order during supercooling of a fragile oxide melt, J. Chem. Phys. 126 (2007) 74906. https://doi.org/10.1063/1.2646812.

[166] G. Ashiotis, A. Deschildre, Z. Nawaz, J.P. Wright, D. Karkoulis, F.E. Picca, J. Kieffer, The fast azimuthal integration Python library: PyFAI, J. Appl. Crystallogr. 48 (2015) 510–519. https://doi.org/10.1107/S1600576715004306.

[167] K. Momma, F. Izumi, VESTA 3 for three-dimensional visualization of crystal, volumetric and morphology data, J. Appl. Crystallogr. 44 (2011) 1272–1276. https://doi.org/10.1107/S0021889811038970.

[168] Q. Meng, H. Li, K. Wang, S. Guo, F. Wei, J. Qi, Y. Sui, B. Shen, X. Zhao, In Situ Synchrotron X-ray Diffraction Investigations of the Nonlinear Deformation Behavior of a Low Modulus β-Type Ti36Nb5Zr Alloy, Metals (Basel). 10 (2020). https://doi.org/10.3390/met10121619.

[169] B. Meyer, Elemental sulfur, Chem. Rev. 76 (1976) 367–388. https://doi.org/10.1021/cr60301a003.

[170] C. Malcolm W., NIST-JANAF thermochemical tables, 4th ed., American Chemical Society ; New York : American Institute of Physics for the National Institute of Standards and Technology, Washington, DC, 1998.

[171] L. Hao, A. Ruban, W. Xiong, CALPHAD modeling based on Gibbs energy functions from zero kevin and improved magnetic model: A case study on the Cr–Ni system, Calphad 73 (2021) 102268. https://doi.org/https://doi.org/10.1016/j.calphad.2021.102268.

[172] V. Dubost, T. Balić-Žunić, E. Makovicky, THE CRYSTAL STRUCTURE OF Ni9.54Pd7.46S15, Can. Mineral. 45 (2007) 847–855. https://doi.org/10.2113/gscanmin.45.4.847.

[173] O. Kubaschewski, C.B. Alcock, P.J. Spencer, Materials thermochemistry, 6th ed., r, Pergamon Press Oxford, Oxford SE - xii, 363 pages : illustrations ; 26 cm, 1993. https://doi.org/LK - https://worldcat.org/title/26724109.

[174] S. Inaba, S. Oda, K. Morinaga, Heat capacity of oxide glasses at high temperature region, J. Non. Cryst. Solids 325 (2003) 258–266. https://doi.org/10.1016/S0022-3093(03)00315-6.

[175] M. Frey, R. Busch, W. Possart, I. Gallino, On the thermodynamics, kinetics, and sub-Tg relaxations of Mg-based bulk metallic glasses, Acta Mater. 155 (2018) 117–127. https://doi.org/10.1016/j.actamat.2018.05.063.

[176] N. Neuber, O. Gross, M. Frey, B. Bochtler, A. Kuball, S. Hechler, I. Gallino, R. Busch,

On the thermodynamics and its connection to structure in the Pt-Pd-Cu-Ni-P bulk metallic glass forming system, Acta Mater. 220 (2021) 117300. https://doi.org/10.1016/j.actamat.2021.117300.

[177] N. Neuber, O. Gross, M. Eisenbart, A. Heiss, U.E. Klotz, J.P. Best, M.N. Polyakov, J. Michler, R. Busch, I. Gallino, The role of Ga addition on the thermodynamics, kinetics, and tarnishing properties of the Au-Ag-Pd-Cu-Si bulk metallic glass forming system, Acta Mater. 165 (2019) 315–326. https://doi.org/10.1016/j.actamat.2018.11.052.

[178] X.H. Lin, W.L. Johnson, Formation of Ti-Zr-Cu-Ni bulk metallic glasses, J. Appl. Phys. 78 (1995) 6514–6519. https://doi.org/10.1063/1.360537.

[179] S. Mechler, E. Yahel, P.S. Pershan, M. Meron, B. Lin, Crystalline monolayer surface of liquid Au-Cu-Si-Ag-Pd: Metallic glass former, Appl. Phys. Lett. 98 (2011) 98–101. https://doi.org/10.1063/1.3599515.

[180] S. V. Ketov, N. Chen, A. Caron, A. Inoue, D. V. Louzguine-Luzgin, Structural features and high quasi-static strain rate sensitivity of Au49Cu26.9Ag5.5Pd2.3Si 16.3 bulk metallic glass, Appl. Phys. Lett. 101 (2012). https://doi.org/10.1063/1.4770072.

[181] S.-L. Chen, Y. Yang, S.-W. Chen, X.-G. Lu, Y.A. Chang, Solidification Simulation Using Scheil Model in Multicomponent Systems, J. Phase Equilibria Diffus. 30 (2009) 429–434. https://doi.org/10.1007/s11669-009-9568-0.

[182] J.E.K. Schawe, Measurement of the thermal glass transition of polystyrene in a cooling rate range of more than six decades, Thermochim. Acta 603 (2015) 128–134. https://doi.org/10.1016/j.tca.2014.05.025.

[183] O. Gross, M. Eisenbart, L.Y. Schmitt, N. Neuber, L. Ciftci, U.E. Klotz, R. Busch, I. Gallino, Development of novel 18-karat, premium-white gold bulk metallic glasses with improved tarnishing resistance, Mater. Des. 140 (2018) 495–504. https://doi.org/10.1016/j.matdes.2017.12.007.

[184] G. Wilde, G.P. Görler, R. Willnecker, G. Dietz, Thermodynamic properties of Pd40Ni40P20 in the glassy, liquid, and crystalline states, Appl. Phys. Lett. 65 (1994) 397–399. https://doi.org/10.1063/1.112313.

[185] J.W. CHRISTIAN, The Theory of Transformations in Metals and Alloys, in: J.W.B.T.-T.T. of T. in M. and A. CHRISTIAN (Ed.), Pergamon, Oxford, 2002: pp. vi–vii. https://doi.org/https://doi.org/10.1016/B978-008044019-4/50001-5.

[186] E.R. BUCKLE, Reduced Temperatures for Nucleation in Supercooled Liquids, Nature 186 (1960) 875–876. https://doi.org/10.1038/186875b0.

[187] R. Busch, E. Bakke, W.L. Johnson, On the glass forming ability of bulk metallic glasses, Mater. Sci. Forum 235–238 (1997) 327–336. https://doi.org/10.4028/www.scientific.net/msf.235-238.327.

[188] M. Frey, N. Neuber, O. Gross, B. Zimmer, W. Possart, R. Busch, Determining the fragility of bulk metallic glass forming liquids via modulated DSC, J. Phys. Condens. Matter 32 (2020). https://doi.org/10.1088/1361-648X/ab8526.

[189] I. Gallino, On the fragility of bulk metallic glass forming liquids, Entropy 19 (2017). https://doi.org/10.3390/e19090483.

[190] J. Ding, Y.Q. Cheng, H. Sheng, E. Ma, Short-range structural signature of excess specific heat and fragility of metallic-glass-forming supercooled liquids, Phys. Rev. B - Condens. Matter Mater. Phys. 85 (2012) 1–5. https://doi.org/10.1103/PhysRevB.85.060201.

[191] L.M. Wang, C.A. Angell, R. Richert, Fragility and thermodynamics in nonpolymeric glass-forming liquids, J. Chem. Phys. 125 (2006). https://doi.org/10.1063/1.2244551.

[192] S. Wei, Z. Evenson, I. Gallino, R. Busch, The impact of fragility on the calorimetric glass transition in bulk metallic glasses, Intermetallics 55 (2014) 138–144. https://doi.org/10.1016/j.intermet.2014.07.018.

[193] O. Gross, S.S. Riegler, M. Stolpe, B. Bochtler, A. Kuball, S. Hechler, R. Busch, I. Gallino, On the high glass-forming ability of Pt-Cu-Ni/Co-P-based liquids, Acta Mater. 141 (2017) 109–119. https://doi.org/https://doi.org/10.1016/j.actamat.2017.09.013.

[194] Z. Ling, Thermodynamic and kinetic study of Pt42.5CuxNi36.5-xP21 alloy variations, Saarland University, 2023.

[195] Z. Wang, S. V. Ketov, C.L. Chen, Y. Shen, Y. Ikuhara, A.A. Tsarkov, D. V. Louzguine-Luzgin, J.H. Perepezko, Nucleation and thermal stability of an icosahedral nanophase during the early crystallization stage in Zr-Co-Cu-Al metallic glasses, Acta Mater. 132 (2017) 298–306. https://doi.org/10.1016/j.actamat.2017.04.044.

Copyright Permissions

Figure	Reference	License Number
2-1	20	5875960321796
2-6	38	5875981382123
2-8	58	5877120824090
2-15	78	5875980194492
4-2	110	1529866-1
4-2	111	5875970995541
4-2	112	5875971371513